



Industrial Digital Fabrication Using Inkjet Technology

Ingo Reinhold

Doctoral Thesis in Information and Communication Technology
School of Electrical Engineering and Computer Science
KTH Royal Institute of Technology
Stockholm, Sweden 2019

TRITA-EECS-AVL-2019:82
ISBN 978-91-7873-366-8

School of Electrical Engineering and
Computer Science
KTH Royal Institute of Technology
SE-164 40 Kista
SWEDEN

Akademisk avhandling som med tillstånd av KTH i Stockholm framlägges till offentlig granskning för avläggande av teknologie doktorsexamen i informations- och kommunikationsteknik på måndag den 9 december 2019 kl. 10:00 i Sal B, KTH, Kistagången 16, Kista.

© Ingo Reinhold, November 2019.

Tryck: Universitetsservice US-AB

Abstract

The use of acoustic waves initiated by the deformation of a microchannel is one method for generating monodisperse, micrometer-sized droplets from small orifices and is employed in piezo-electric inkjet printheads. These printheads are used in both graphical printing and digital fabrication, where functionalities, such as optical, biological, electrical or mechanical, are being produced locally. The processes leading to detrimental artifacts such as satellite droplets or nozzle outages, however, are not fully understood and require profound experimentation. This thesis presents both novel techniques to study jetting for optimal droplet formation and reliability, as well as the post-processing techniques required for solution-based production of a conductive feature on low-cost polymeric substrates.

A multi-exposure imaging system using laser light pulses shorter than 50 ns and a MEMS micro-mirror enabled the imaging of the droplet formation at ten instances on the droplet's travel towards the substrate. The technique allows for the study of droplet formation, satellite droplet break-up and secondary tail formation allowing for better control and understanding of the process.

Reliability measurement using a linescan camera was introduced to record every droplet ejected from the width of a printhead. The variations in droplet velocity and misalignment of the printhead required the use of a constant background illumination to reliably capture the droplets. The resulting low-contrast images were post-processed using statistical analysis of the graylevel distributions of both, the droplet and background pixels, and were subsequently used in a histogram matching algorithm to enable reliable identification of the threshold value required for unhindered detection of missing droplets based on the printed image. Using temporal oversampling the technique was shown to qualitatively describe droplet velocity variations introduced by the actuation of the printhead.

The conversion of inkjet-printed metallic nanoparticle inks to conductive structures was investigated with a focus on the applicability to industrial processes. Intense pulsed light (IPL) processing achieved comparable results to convective oven sintering in less than ten seconds. The dynamics of IPL sintering were found to be strongly dependent on the spectral composition of the light resonating in the processing chamber. By implementing a passive filtering concept, thermal runaway was prevented and the line conformation was optimized irrespective of the underlying substrate. Alternatively, pulse-shaping, to tailor the energy flux into the deposit and incorporate drying in the IPL process, was found to generate conductive copper features without pre-drying.

The findings were applied to applications comprising small droplet generation for nanoimprint lithography, the fabrication of conductors for blind via connections to buried LED dies as well as the hybrid generation of hyperbolic ion-trap electrodes for mass spectrometry applications. The addition of the non-contact and high accuracy of the inkjet process enabled suitable performance that lies beyond that of conventional processes.

Keywords: inkjet printing, droplet formation, digital fabrication, sintering, nanoparticles, printed electronics

Sammanfattning

Användningen av akustiska vågor som är initierad genom deformation av en mikrokanaal är ett exempel på generering av monodispersa mikrometer-små droppar från små öppningar och används i piezo-elektriska bläckstråleskrivhuvud. Dessa skrivhuvuden används i både grafisk tryckning och digital tillverkning, där funktionaliteter såsom optiska, biologiska, elektriska eller mekaniska, produceras lokalt. Processerna som leder till oönskade artefakter som satellitdroppar eller dysavbrott är emellertid inte helt förstådda och kräver ingående experiment. Denna avhandling presenterar både nya tekniker för att studera tekniker för optimal droppbildning och tillförlitlighet, såväl som efterbehandlingstekniker som krävs för lösningsbaserad produktion av en ledande film på billiga polymersubstrat.

Ett bildbehandlingssystem med flera exponeringar vilken använder laserljuspulser som är kortare än 50 ns och en MEMS-mikrospegel möjliggjorde avbildning av droppbildningen i tio bilder under droppens rörelse mot substratet. Tekniken möjliggör studier av droppbildning, satellitdroppuppbrott och sekundär svansbildning som möjliggör bättre kontroll och förståelse av processen.

Tillförlitlighetsmätning med hjälp av en linjekamera infördes för att avbilda varje droppe som matas ut från skrivhuvudets bredd. Variationerna i dropphastigheten och felinställningen av skrivhuvudet krävde användning av en konstant bakgrundsbelysning för att tillförlitligt registrera dropparna. De resulterande bilderna med låg kontrast efterbehandlades med användning av statistisk analys av gråskalefördelningarna för både droppen och bakgrundsbildpixlarna och användes därefter i en histogrammatchande algoritm för att möjliggöra pålitlig identifiering av tröskeln som krävs för stabil detektion av saknade droppar baserat på den tryckta bilden. Med användning av temporär översampling visades tekniken kvalitativt beskriva dropphastighetsvariationer införda genom aktiveringen av skrivhuvudet.

Omvandlingen av bläckstråleskrivna metalliska nanopartikelfärger till ledande strukturer undersöktes med fokus på användbarheten för industriella processer. Intense Pulsed Light (IPL) processering uppnådde jämförbara resultat med konvektiv ugnsintring på mindre än tio sekunder. Dynamiken för IPL-sintring befanns vara starkt beroende av den spektrala sammansättningen av ljuset som resonerar i behandlingskammaren. Genom att implementera ett passivt filtreringskoncept förhindrades temperaturhöjning och linjekonformationen optimerades oavsett underlag. Alternativt visades att pulsformning, för att skräddarsy energiflödet i depositen och införliva torkning i IPL-processen, genererar kopparledare utan förtorkning.

Resultaten applicerades på applikationer som innefattade små-droppgenerering för nanoimprint-litografi, tillverkning av ledare för dolda via-anslutning till begravnad LED-matriser samt hybridgenerering av hyperboliska jonfälleelektroder för masspektrometriapplikationer. Tillägget av icke-kontaktering och hög noggrannhet i bläckstråleprocessen möjliggjorde lämplig prestanda som ligger utanför möjligheterna i konventionella processer.

Nyckelord: bläckstråleskrivning, droppbildning, digital tillverkning, sintring, nanopartiklar, tryckt elektronik

List of Appended Papers

- A Analysis of Formation of an Individual Droplet Using a High-Resolution Multi-Exposure Imaging System

Ingo Reinhold, Karsten Sitterberg, Matthias Müller, Mamat Abdulla, Sergej Popov, Wolfgang Voit, Werner Zapka. In: *International Conference on Digital Printing Technologies and Digital Fabrication*, 2013.

Author's contribution: The author contributed to design and implementation of the imaging method, experimentation and produced the manuscript.

- B Inkjet Printing of Electrical Connections in Electronic Packaging

Ingo Reinhold, Wolfgang Voit, Moritz Thielen, Maik Müller, Matthias Müller, Stan Farnsworth, Ian Rawson, Roger Bollström, Werner Zapka. In: *International Conference on Digital Printing Technologies and Digital Fabrication*, 2011.

Author's contribution: The author planned and produced the required sample sets, analyzed the data and produced the manuscript.

- C Spectrally Enhanced Photonic Sintering

Ingo Reinhold, Matthias Müller, Maik Müller, Wolfgang Voit, Werner Zapka. In: *International Conference on Digital Printing Technologies and Digital Fabrication*, 2012.

Author's contribution: The author contributed to production of the samples, assessment of the intensity profiles, analysis of the data, development of the passive filtering approach and produced the manuscript.

- D Novel Developments in Photonic Sintering of Inkjet Printed Functional Inks

Ingo Reinhold, Wolfgang Voit, Ian Rawson, Karl Martin, Stan Farnsworth, Werner Zapka, Charles Munson. In: *International Conference on Digital Printing Technologies and Digital Fabrication*, 2013.

Author's contribution: The author contributed to the experimentation, the development of the arbitrary pulse shape for drying and sintering, analysis of the data and produced the manuscript.

- E High-Speed, Low-Volume Inkjet and Its Role in Jet and FlashTM Imprint Lithography

Ingo Reinhold, Matthew Shafran, Whitney Longsine, Matthew Traub, Yeshwanth Srinivasan, Van Truskett, Werner Zapka. In: *International Conference on Digital Printing Technologies and Digital Fabrication*, 2014.

Author's contribution: The author contributed to the creation of the optimum drive of the printhead, modification of the printhead geometry and produced the manuscript except for results of the imprint process.

- F Electrical Through-Hole and Planar Interconnect Generation in Roll-to-Roll LED-Lighting Manufacturing Using Industrial Inkjet Printheads

Ingo Reinhold, Moritz Thielen, Wolfgang Voit, Werner Zapka, Reiner Götzen, Helge Bohlmann. In: *Materials Research Society Symposium Proceedings*, 2012.

Author's contribution: The author contributed to the investigation of the sintering behavior, planning of the experiments, analysis of the data and produced the manuscript.

- G A Hybrid Approach Combining 3D and Conductive Inkjet Printing for the Generation of Linear Ion Traps for Mass Spectrometry Applications

Ingo Reinhold, Mirko Wittkötter, Maik Müller, Fritz Koch, Fabrizio Siviero, Robert Murcott, Werner Zapka. In: *International Conference on Non-Impact Printing and Digital Fabrication*, 2014.

Author's contribution: The author contributed to production of the samples, optimization of the surface finish of the 3D printed parts, analysis of the data and produced the manuscript.

- H Industrial, Quantitative Assessment of Inkjet Reliability Under High-Duty, Conditions: Measuring All Drops during Extended Printing

Ingo Reinhold, Tomáš Černý; In W. Zapka (Ed.), *Handbook of Industrial Inkjet Printing* (1st ed., pp. 445–458). Weinheim: Wiley-VCH. 2018.

Author's contribution: The author contributed to the implementation of the setup, experimentation, assessment of image analysis techniques, produced the computer code for alignment and analysis of the recorded images and wrote the manuscript.

Related Publications

- I Inkjet Printing of Functional Materials and Post-Processing
Ingo Reinhold; In Shlomo Magdassi (ed.) and Alexander Kamyshny (ed.), *Nanomaterials for 2D and 3D Printing*, (1st ed., pp. 27–50), Weinheim: Wiley-VCH. 2017.
- II Measurement of Mass of Single Inkjet Drops with a Quartz Crystal Microbalance QCM
Ingo Reinhold, Vasile Mecea, Lucas Armbrrecht, Wolfgang Voit, Werner Zapka, Reinhard R. Baumann. In: *International Conference on Digital Printing Technologies and Digital Fabrication*, 2012.
- III Evaluation of Crosstalk Effects in Inkjet Printing with Xaar 1001
Wolfgang Voit, Nick Jackson, Katrin Preckel, Sohail Iqbal, **Ingo Reinhold**, Werner Zapka. In: *International Conference on Digital Printing Technologies and Digital Fabrication*, 2011.
- IV Ink Jet Printing of Conductive Silver Tracks from Nanoparticle Inks on Mesoporous Substrates
Anna Schuppert, Moritz Thielen, **Ingo Reinhold**, Wolfgang Schmidt. In: *International Conference on Digital Printing Technologies and Digital Fabrication*, 2011.
- V Parallel Software Design Enabling High-Speed Reliability Testing of Inkjet Printheads
George Ungureanu, **Ingo Reinhold**, Ingo Sander, Werner Zapka. In: *International Conference on Digital Printing Technologies and Digital Fabrication*, 2013.
- VI Drucken Jenseits Der Farbe
Werner Zapka, Wolfgang Voit, **Ingo Reinhold**. *Elektronik*, 12, 2013, 34–39.
- VII Ink-Jet Printed Copper Complex MOD Ink for Plastic Electronics
Yousef Farraj, Michael Grouchko, Shlomo Magdassi, Fritz Koch, Mirko Witkötter, Maik Müller, **Ingo Reinhold**, Werner Zapka. In: *International Conference on Digital Printing Technologies and Digital Fabrication*, 2014.
- VIII Break-up Time in Inkjet Printing from Bulk Rheological Data
Maik Müller, Gustaf Mårtensson, **Ingo Reinhold**, Tim Wickens, Werner Zapka, In: *International Conference on Digital Printing Technologies and Digital Fabrication*, 2015.

IX Speed and Accuracy of High Speed Sintering

Adam Ellis, Antonis Hadjiforados, Neil Hopkinson, **Ingo Reinhold**. In: *International Conference on Digital Printing Technologies and Digital Fabrication*, 2015.

Contents

Abstract	III
List of Appended Papers	VII
1 Introduction	1
1.1 Digital Fabrication	2
1.2 Motivation and Challenges	3
1.3 Research Objectives	6
1.4 Thesis Contribution and Organization	6
2 Inkjet Technology	9
2.1 History	9
2.2 Droplet Generation with Piezo Inkjet Technology	11
2.3 Print Artifacts	14
2.3.1 Crosstalk	14
2.3.2 Air Ingestion	15
2.3.3 Satellite and Mist Generation	16
2.3.4 Nozzle Plate Wetting	17
3 Measurement Techniques	19
3.1 Imaging Methods for Single Droplet Studies	19
3.1.1 Experimental Setup	20
3.1.2 Results and Discussion	22
3.1.3 Summary	23
3.2 Qualitative Reliability Assessment by Measuring Every Droplet ..	24
3.2.1 Reliability Measurement Approaches	24
3.2.2 Linescan In-Flight Imaging	27
3.2.3 Low Contrast Handling	30
3.2.4 Analysis Results	31
3.2.5 Summary	33
4 Inkjet-Printing and Post-Processing of Metallic Conductors ..	35
4.1 Ink Concepts	35
4.2 Sintering Mechanisms	36

4.3	Selective Sintering	38
4.4	Influence of Drying	38
4.5	Technologies for Continuous Post-Processing of Metal Inks.....	39
4.5.1	Influence of the Spectral Characteristics of the Underlying Layer	41
4.5.2	Substrate-Dependent Line Formation	44
4.5.3	Passive Optimization	45
4.5.4	Active Optimization	45
4.6	Residues and Entrapped Gases	47
4.7	Summary	49
5	Applications	51
5.1	Hybrid Approaches to High-Resolution Structure Generation.....	51
5.2	Digital Conductor Printing onto 2.5D Substrates	56
5.2.1	Blind Via Connections	56
5.2.2	Printing Conductors on 3D Printed Parts	59
5.2.3	Summary	60
6	Conclusion	63
	Acknowledgments	65
	References	67

List of Abbreviations

AOI	Area of Interest
ASIC	Application Specific Integrated Circuit
CCD	Charge-Coupled Device
CDF	Cumulative Distribution Function
CIJ	Continuous Inkjet
CMOS	Complementary Metal-Oxide Semiconductor
CTE	Coefficient of Thermal Expansion
DLP	Digital Light Processing
DoD	Drop-on-Demand
DPI	Dots per Inch
DTG	Direct to Garment
FFT	Fast Fourier Transformation
FPS	Frames per Second
ILIF	Illumination by Laser-Induced Fluorescence
IPL	Intense Pulsed Light
IR	Infrared
JFIL	Jet-and-Flash Imprint Lithography
LED	Light Emitting Diode
LIT	Linear Ion Traps
LOC	Lab-on-Chip
LUT	Look-Up-Table
MEMS	Microelectromechanical Systems
NIL	Nanoimprint Lithography
NIR	Near Infrared
OLED	Organic Light Emitting Diode
PZT	Lead Zirconate Titanate
R2R	Roll-to-Roll
RIP	Raster Image Processing
RLT	Residual Layer Thickness
SLA	Stereolithography
SNR	Signal-to-Noise Ratio
SOHO	Small and Home Office Market

Introduction

The generation of monodisperse microdroplets has implications for many applications and attracts significant interest in academic research. Applications span from the preparation of emulsions, the distribution of droplets in sprays for the optimal uptake of medicine in the human lung to the high-frequency creation of molten tin droplets for the extraction of ultraviolet (UV) radiation in extreme UV lithography tools.^{1–3}

Inkjet actuators are one of the methods to produce monodisperse, picoliter-sized droplets emanating from a free jet of fluid with a viscosity lower than 25 mPa.s.

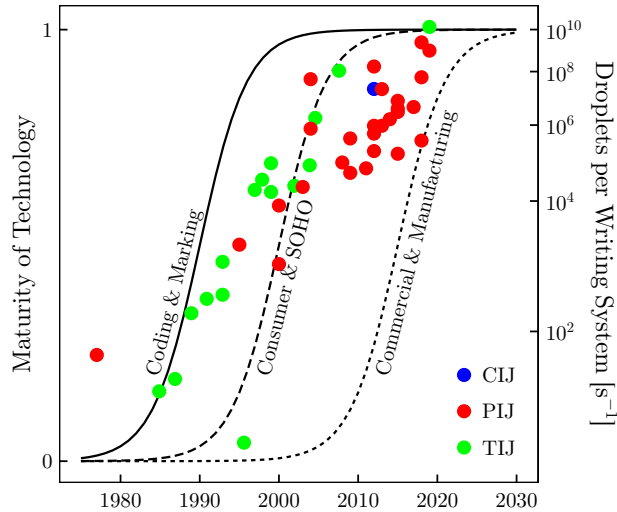


Fig. 1.1. Overview of the developments in the digital printing markets according to Hutchings *et al.*⁴ (lines) and the number of droplets created in commercial inkjet writing systems (dots) for continuous inkjet (CIJ), thermal inkjet (TIJ) and piezo inkjet (PIJ).^{5–15}

Inkjet printing has undergone significant developments in productivity and as a result has penetrated many markets, as is depicted in Figure 1.1. The resolution and print frequency of early inkjet printheads was limited to tens of nozzles at a resolution of 90 DPI, which were used for the coding and marking of products in the 1980s. With the increase in nozzle density, desktop printing (Small and Home Office, SOHO) and wide-format graphics came into reach, which commonly utilized multi-pass printing to obscure some of the deficiencies in printhead reliability. The increase in quality, productivity, but most importantly reliability led to digital printing of commercial print products such as labels, books and newspapers, which pressured classical printing techniques such as flexography, rotogravure and offset printing due to the decline in run-length. Inkjet also displaced many of the electrophotographic processes due to its higher flexibility and scalability. For instance the complexity of charging consistency in electrophotographic nanography is nowadays reduced by inkjetting a type of liquid toner material directly onto a transfer belt.¹⁶ The last major wave in the adoption of digital printing techniques was seen in the industrial markets, where inkjet replaced rotary screen printing in the ceramic tile industry within only a few years, as sedimentation of the high density ceramic particles could be counterbalanced by continuous convective flow through the channels of the printhead. A similar transformation is currently anticipated in the single-pass digital textile market, which had previously adopted multi-pass printing for direct-to-garment (DTG) applications, but now increases rapidly in productivity through single-pass print strategies to accommodate the market trends of custom and fast fashion.

Advances made in the production of nano- or micron-sized particles, the stabilization of colloids in low viscosity fluids as well as the understanding of the dynamics of monomers and polymers provide the production of inks that enable products with sufficient color gamut, light fastness alongside with sufficient adhesion and controlled dot gain on the substrate.¹⁷ The concepts developed were, however, not limited to ink pigments and dyes only but could be applied to constituents with mechanical, biological or electrical functionality.

The combination of advanced materials being made jettable and printheads improving in integration density, lower droplet volumes, increased jetting frequencies as well as improved reliability, altogether facilitates new applications, where inkjet is used as a fabrication tool that is capable to tailor optical, electrical, mechanical or chemical functionality.

1.1 Digital Fabrication

With the initial purpose of producing graphical prints with reduced run-lengths, digital printing, and in the recent years most prominently inkjet printing, was part of a broader development towards the digitalized production of products. The benefit can be mainly attributed to the elimination of pre-manufactured masters, whose production cost dictates the minimum lot size, but also through reduced material waste as well as change-over and setup times. In the printing market this enabled the profitable production of print products.

The transition to digital fabrication does not come without the necessity to rethink. Printing with massive arrays of nozzles requires the discretization of

the product into pixels or voxels in a two- or three-dimensional grid, which is fundamentally different from typical vector-based representations in the analog manufacturing industry. Pixels or voxels can then be used to not only attribute characteristics such as volume or location to an element, but in a digital fabrication setting provide mechanical, electrical or optical properties. This, in consequence, enables the local tailoring of material properties which are difficult or even impossible to manufacture with conventional techniques.^{18,19} One key aspect for achieving this is the possibility to deposit a wide range of fluids with volumes in the range of 1–200 pL from a large number of orifices with a native lateral resolution of tens of micrometers.

An additional benefit of inkjet is the *non-impact* nature of the image formation, so that no direct force is exerted onto the substrate except for the interaction of the impinging droplet. The reduction of substrate thickness to minimize cost is an evident trend in the industry and has its limitation in the peak distributed load for breakage.²⁰ In addition a change in topography does not impose insurmountable challenges to inkjet. Droplet placement variations due to altered flight times and potential differences in deceleration due to Stokes drag can, within limits, be already incorporated in the Raster Image Processing pre-press steps.^{21,22}

The direct and additive nature of the inkjet process compared to subtractive processes often used in the electronics industry is a key feature, where not only process steps but also material waste can be minimized. Waste in, for instance, commonly used spin coating is estimated to be higher than 85% and represents a large portion of the consumable cost.²³ With increasing prices for highly sophisticated materials such as photoresists or rare earth materials required for today's functionality, resolution and yield; subtractive processing can become prohibitive to the cost target of modern devices. In addition the removal of process steps does not only reduce the overall process time but also the necessity of additional process equipment and thereby the total cost of ownership.

An early example of digital fabrication using inkjet was the the generation of pixels in OLED display manufacturing, where prepatterned wells for the respective colors were filled with a 70 nm thick layer of light-emitting polymer.^{24,25} The required thickness tolerance needed to be kept within a few percent as otherwise the varying electric field strength across the device would alter the photon yield of the pixels. This development highlights many of the challenges in digital fabrication, spanning the material science to find suitable functional and soluble materials, to pre-patterning of the substrate and to the development of the print process to provide the consistency and reliability in conjunction with drying of the deposits.^{26,27}

1.2 Motivation and Challenges

Digital fabrication differs greatly from graphical printing in the sense that requirements are much more stringent while throughput requirements seldom relax. It is therefore that consistency of droplet velocity, volume and trajectory are fundamental requirements for the process of drop formation. The more challenging target in this context is the reliability of the process, where a single missing droplet may render the product non-functional. Sophisticated techniques such as

photographing each deposited droplet have been developed to provide insight into the correct operation of printheads and guarantee the correct dosage of functional material.²⁸

A critical step is the transition from the laboratory to the production stage, typically referred to as the Lab2Fab transition. Here the complexity of the inkjet process changes appreciably with increasing number of nozzles and printheads, the accommodation of varying patterns and the accompanying differences in crosstalk, altered drying behavior due to a change in composition of the surrounding atmosphere and reliability considerations in a 24-7, often single-pass, operation.

Mimicking these variations in a laboratory environment is often challenging, mostly time consuming and costly. For instance reliability in the graphics world is still assessed by eye on hundreds of meters of paper and therefore has to be limited to a finite time interval. Drop-watching setups are more efficient, as they can be configured to recycle ink and enable longer print runs at reduced cost. These are, however, often limited in the field of view to some tens of nozzles in the print pattern rather than imaging a complete printhead and all ejected droplets. Pattern variability is often limited, so that it is important to test worst-case scenarios, where all nozzles fire simultaneously. This, however, in some cases gives rise to lower droplet velocities, whereas air ingestion due to strongly moving menisci may be dominant in much more sparse pattern configurations.²⁹ Droplet visualization techniques advanced with the improvement and affordability of cameras with higher resolution and acquisition rates as well as improved image analysis algorithms to estimate the drop volume assuming rotational symmetry.^{30–33} The fundamental challenges of analyzing inkjet printing remain, where both droplet velocities of 10 m s^{-1} and dimensions as small as $1\text{ }\mu\text{m}$ need to be quantified to study both the development of the primary tail as well as the disintegration of secondary tails into mist.³⁴ Sophisticated experimental techniques enable nowadays high-resolution imaging but often rely on stroboscopic illumination and the high repeatability of the droplet formation process.³⁵

The development of electrical driving waveforms is highly complex, as the pressure behind the nozzle needs to be tailored to efficiency, rapid damping and minimal crosstalk while creating fast droplets without satellites, which are sufficiently tolerant to fluctuations in temperature and duty cycle. Advances made towards an optimal drive and thus optimum drop formation are accomplished with optimization routines in embedded systems. These combine the input from droplet formation with the residual pressure signal in the channel.^{36,37} However, they still rely on the pattern-based acquisition and image analysis and do not allow for a direct correlation to reliability. Residual fluctuations were shown to be able to assess nozzle health to proactively initiate redundancy measures or trigger preventive maintenance.^{38,39} Other reliability measurement techniques mainly focus on printhead technologies without the ability to automatically recover from air ingestion or debris.^{40,41}

From a fluid point of view, selection is often a limiting factor. Here the finite solubility of materials in a solvent, the limited dispersion stability, the viscosity requirements as well as the orthogonality of solvent systems to previously deposited layers poses challenges for material scientists. Many studies are produced

on the solubility and stability of inks, but a limited amount of research is published on the achievement of multilayer stacks with complicated structures and the influence of surface energy contrast.⁴²

Following the deposition step the remaining challenge is the formation of a dense layer of functional material at process speed. Particle-based functional fluids require the removal of the ink solvent as well as the polymeric stabilizing agents before particles come into physical contact and fuse together. Thermal removal is one of the most common procedures,^{43–45} but is limited by the mechanical integrity of polymeric substrates. Lower temperatures and extended hold times of 30 to 60 minutes are often employed,⁴⁶ which are incompatible with Roll-to-Roll (R2R) processes. Alternative approaches to selectively or rapidly heat the deposits have been proposed but are often either time-consuming or exhibit strong dynamics, which require special attention.⁴⁷ On the timescales available for the creation of the final functionality, surface tension- and concentration-driven distribution of the solute start to play an important role. For non-absorbing substrates solvents often are chosen for rapid evaporation, which induce redistribution of material due to the concentration gradient triggered by the strong solvent flux at the contact line. For electrical conductors this may trigger locally enhanced resistance or result in a variation of the electrical field intensity in the deposition of dielectrics and semi-conductors.^{48–50} To date post-processes for printed conductors on non-absorbing substrates are separated into subsequential drying and sintering. The combination of rapid evaporation and functionality formation within a single, high-speed process is still to be found.

Lastly, limitations in productivity as well as critical dimensions are widely discussed in the community. Techniques for the creation of 2.5D and 3D structures evolve into mature processes,^{51,52} but the limitation in throughput compared to conventional manufacturing processes is appreciable. Hybrid approaches for separating the creation of shape and adding functionality often appear more economical. Examples for such approaches can be found in Lab-on-Chip (LOC) devices,⁵³ where the underlying fluidic network is prepared by hot embossing or injection molding, whereas dielectrics and conductors are added in subsequent printing steps.⁵⁴

Another driver for the adoption of hybrid approaches is to overcome the resolution limit of inkjet.⁵⁵ This limitation is posed by the physical spacing of adjacent nozzles, nozzle sizes and landing accuracy alongside with the dynamic wetting of a low viscosity fluid on a substrate. Surface energy patterning offers the possibility to exploit surface tension forces exerted on the liquid to constrain or even move fluid to specific locations on the substrate.^{56,57} Alternatively the fluid film can be patterned after deposition as it is performed for instance in Jet-and-Flash imprint lithography.⁵⁸ Here the inkjet-printed fluid layer, which varies locally in thickness, enables minimizing the capillary filling time of the nanometer-sized features and reduces defectivity in the created resist pattern.⁵⁹ The requirement for smaller residual layer thicknesses (RLT) to minimize the critical dimension of the process pushes the jetting process to extremely small droplets at high repetition rates.

1.3 Research Objectives

The two main goals of this thesis address the challenges outlined above. The first topic describes the improvement of the experimental techniques for the quantitative measurement of jetting performance in a laboratory environment to minimize the gap in the transition to fabrication. Secondly will intense pulsed light (IPL) processing be investigated and optimized for the generation of inkjet-printed conductors from nanoparticle dispersions without intermediate drying.

- **Objective 1:** Develop a droplet visualization system that images the generation and trajectory of one single droplet and allows the study of tail formation.
- **Objective 2:** Develop a measurement system to visualize all droplets ejected from the width of a printhead over a period of time and analyze the data according to the printed pattern.
- **Objective 3:** Investigate suitable post-processing techniques for the inline formation of electrically conductive inkjet-printed metal deposits on polymeric substrates in a R2R process.
- **Objective 4:** Assess the applicability of intense pulsed light sintering of nanoparticle deposits on non-absorbing substrates without intermediate drying.
- **Objective 5:** Extend the range of applications that benefit from digital fabrication through the techniques developed in Objectives 3 and 4.

1.4 Thesis Contribution and Organization

The contributions of the author with respect to the above mentioned objectives are as follows

- **Contribution 1:** A stroboscopic technique was designed and implemented to overcome the challenges caused by the reduced spatial resolution of high-speed cameras and by the low temporal resolution of cameras typically used in the stroboscopic setups. A laser diode was employed to produce light pulses shorter than 50 ns with sufficient intensity to create a sharp image of an inkjet droplet in flight. By using the slow and fast axis of the laser diode the imaged area was confined to the trajectory of the droplet. The resulting slit illumination was swept across a CCD chip by means of a resonant MEMS micro-mirror. Synchronizing the illumination to the printhead produced multiple images during the transition of the droplet through the field of view in a single exposure of the CCD. In this fashion the *same* droplet could be imaged on a high resolution CCD at various stages of its development (**Paper A**).
- **Contribution 2:** A new set up, allowing the investigation of every droplet released from the width of a printhead was devised and implemented. Continuous background illumination was shown necessary to accommodate for time-of-flight variations. The system uses a linescan camera, which is triggered at threefold the frequency of the printhead to image all ejected droplets. Sample data was recorded from a printhead at 18 kHz cycle frequency. As the constant background illumination resulted in a low contrast image, the two

Gaussian distributions for droplets and background pixels in the histograms were difficult to discriminate. Statistical data analysis was used to estimate the mean μ and standard deviation σ of the distributions in the recorded gray level, which were subsequently used in histogram matching to allow for improved thresholding. The technique provided sufficient resolution to identify missing as well as laterally deviated droplets and was used to investigate droplet velocity variations qualitatively (**Paper H**).

- **Contribution 3:** Inkjet printed electrical conductors were produced for the electrical connection of LEDs on a polymeric carrier with low thermal stability. Various sintering methods including thermal, infrared (IR) radiation and intense pulsed light curing were investigated with respect to compatibility with the used materials, consistency of the results as well as their applicability to R2R processing. IR was found to produce conductive traces with a resistance of approximately $31 \Omega \text{ cm}^{-1}$, but compromised the integrity of the polymeric foils. It was shown that IPL sintering was capable to achieve resistances as low as $9.6 \Omega \text{ cm}^{-1}$ within three seconds without damage to the sensitive substrate. Thermal sintering achieved an equivalent value, however, for a sintering time of thirty minutes (**Paper B**).
- **Contribution 4:** Wet intense pulsed light processing was assessed for the inline sintering of nanoparticle deposits in a R2R process. The results showed a strong dependency on the wavelengths present during different stages of the sintering process. Different spectral compositions of the light resonating between the substrate holder and the reflector of a broadband Xenon lamp were investigated. Employing different absorbers resulted in (a) damping the blue portion of the spectrum and thus prevented thermal runaway and (b) preserving the red portion for both indirect heating as well as avoidance of the redeposition of evaporated solvent in the vicinity of the cured layers. A passive filter was implemented to optimize both line formation and electrical performance. Using this wet sintering approach we found resistance values lower than $5 \Omega \text{ cm}^{-1}$ with sintering times not exceeding ten seconds on polyimide. Using the passive damping of the incident light allowed to sinter deposits on PET into smooth lines with resistance values of $3\text{--}4 \Omega \text{ cm}^{-1}$, without dewetting and discontinuous tracks.

As an alternative, temporal shaping of the energy delivered by the arc lamp was investigated on a copper oxide ink. It was shown that by shaping the amplitude of a pulse train, both drying and sintering could be conducted in a single step. Substrate feed velocities up to 0.18 m s^{-1} were investigated and allowed to produce resistances of $11.5 \Omega \text{ cm}^{-1}$. These methods were superior to those involving pre-drying with IR radiation, which did not result in consistent conductivities at these feed rates (**Paper C** and **Paper D**).

- **Contribution 5:** The findings from the measurement techniques developed, as well as the sintering optimization were applied to different applications. Firstly, stable low volume droplet ejection was developed for the application in *Jet-and-Flash* imprint lithography (JFIL). In a first step the droplet volume ejected from a commercial printhead was reduced from 6 pL to 2.4 pL by adjusting the driving waveform. The meniscus pressure was found to reduce the result by an additional 0.4 pL within a stable meniscus pressure window.

By additionally changing the geometry of the printhead, the volume was reduced to as low as 0.9 pL. This droplet size enabled a reduction in squeeze time by 500 ms, or 20%, at a constant defect density (**Paper E**).

Findings from the sintering process optimization were applied to the generation of conduction paths through blind vias in polymeric substrates for the electrical connection to buried LEDs as well as the creation of the electrodes in polymer-based linear ion-traps (LIT).

- IPL sintering using passive damping was used to produce the electrical series connection of three LEDs through via connections with a silver film within six seconds. Cracks appeared in the deposits at currents above 400 mA, caused by Joule heating, which induced failure at the rim. However, the application only required 20 to 40 mA, such that inkjet printed conductors were suitable to drive these LEDs (**Paper D** and **Paper F**).
- Conventional thermal sintering of silver nanoparticles was performed on 3D-printed ion-trap electrodes for mass spectrometry applications. A resistance of $500 \text{ m}\Omega \text{ cm}^{-1}$ was produced. This was higher than the $250 \text{ m}\Omega \text{ cm}^{-1}$ achieved by standard plated specimen, however, at a fraction of the material thickness. The electrode arrangement was found to be sufficiently conductive for the application. It was shown that outgassing from sintered samples was sufficiently low when sintering was performed at 200°C . Therefore no increase in the backpressure of the measurement chamber was expected (**Paper G**).

The following chapters focus on different aspects of the outlined contributions. Chapter 2 is an introduction to the inkjet technology and discusses a set of challenges faced in new application fields. Chapter 3 first discusses the high resolution measurement techniques currently used to study droplet formation and the approach proposed in this thesis. A second part focuses on the standard techniques for reliability measurements and introduces the developed *linescan* approach together with the algorithms and example data. Chapter 4 presents the digital fabrication of conductors on low-cost substrates with a focus on the sintering process. The results described are then discussed in Chapter 5 with respect to applications, where the consistent generation of small droplets as well as the creation of conductive surfaces for LED interconnects and electrodes for linear ion traps are presented. Chapter 6 summarizes the thesis.

Inkjet Technology

Drop-on-Demand (DoD) inkjet printing is nowadays considered a mature technique for digital printing in applications such as SOHO printing, wide-format graphics and ceramic tile production. Transitioning into new fields, such as single-pass production printing, printed electronics, and 3D printing, requires improvements in print frequency, fidelity and reliability.

This chapter presents a brief history of inkjet technology as a way of delivering pL-sized droplets. The physical principles of piezo inkjet droplet generation are described, along with challenges inherent to this particular technology.

2.1 History

The development of the inkjet technique as way of producing small droplets is based on the 19th century ground-breaking work on the flow of fluid by *Navier* (1822) and *Stokes* (1845) alongside with the description of disintegration of a liquid jet by *Plateau* (1843), *Hagen* (1873) and *Lord Rayleigh* (1878). The actuation principle can be largely related to the description of electro-magnetic forces by *Maxwell* (1865) and the discovery of the piezoelectric effect by the brothers *Curie* (1880).

From first printing machines using solely the Rayleigh breakup for the production of electro-cardiograms,⁶⁰ continuous inkjet (CIJ) printers emerged (e.g. Videojet 9600, 1968). CIJ employs the controlled break-up of a liquid jet emerging from a pressurized chamber, often assisted by a superposed disturbance created with a piezo element. With the ability to precisely predict the break-up point of a droplet, charging electrodes can be used to displace charges from the conductive ink into the forming droplet and provide it with a well controlled charge. This can then be utilized to deflect droplets in an electric field and remove non-printing droplets via a gutter. Derivatives of this technique include multi-deflection of droplets using quantized charge levels⁶¹ as well as grayscale printing.⁶² The latest development was the integration into a MEMS printhead by Kodak,⁶³ where heaters around the nozzle locally reduce the surface tension along the jet and thereby allow for the creation of differently sized droplets. The selection of droplets is conducted by a laminar air-flow that deflects droplets depending on their volume (*cf.* Figure 2.1).⁶⁴

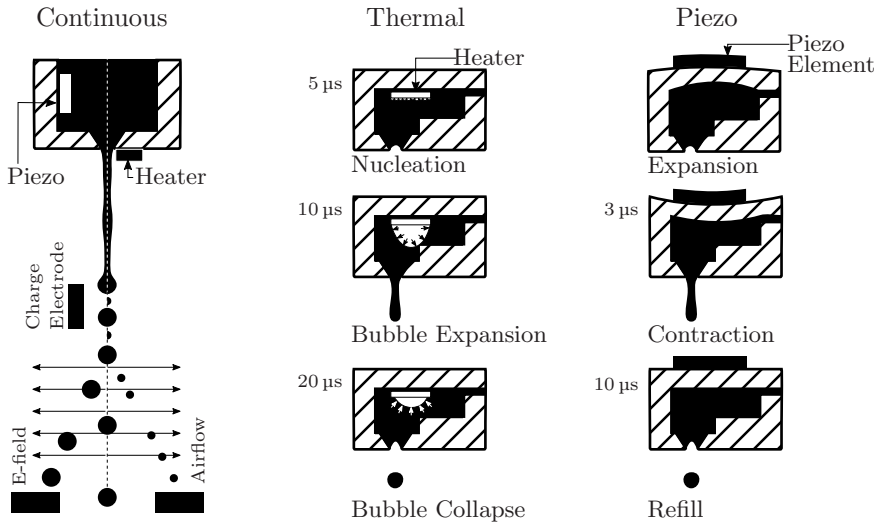


Fig. 2.1. Basic principles of inkjet printheads: (a) continuous (CIJ), (b) thermal (TIJ) and (c) piezo (PIJ) inkjet (adapted from ^{64–66}).

The challenges of CIJ with respect to the charging, deflecting and catching of unwanted droplets, sparked research into the field of Drop-on-Demand (DoD) inkjet, which would produce droplets only when needed. The potential of creating pressure by way of the deformation of a channel using a piezoelectric ceramic was realized early on, but was not the first technique to enter the market. Electrostatic pull inkjet, which extracts a volume of fluid from a nozzle filled with conductive fluid when a strong electric field is applied was introduced in the 1960s.

The effect of droplets leaving a nozzle when quickly heated, found accidentally in the attempt to develop a piezo inkjet,⁵ led to the introduction of thermal inkjet technology. Here the spontaneous nucleation of vapor bubbles on the surface of the heating element at heating rates higher than 10^7 K s^{-1} is utilized. The nuclei form into a thin vapor film that starts forming a bubble. The increasing vapor bubble exerts a pressure pulse into the confined channel and towards the nozzle, which leads to the ejection of a droplet.^{61,67,68} The bubble then collapses when the heat source is switched off. Developed in the end of the 1970s by Canon and Hewlett-Packard this technology enabled the first low-cost inkjet printers that dominate the SOHO market until today due to the cost-efficient MEMS manufacturing processes. The technique has progressed into a variety of large-scale industrial applications with nozzle densities of up to 2400 DPI.^{69–71}

The patents filed on piezo inkjet (PIJ) between 1970 and 1985 described all modes commonly known in inkjet, with the most dominant in current printheads being the bend mode as used by Xerox, Epson, Dimatix, Konika Minolta and Xaar. Both shear mode (Xaar, Spectra/Dimatix, SII Printek, Microdrop) and bump or *direct* mode (Epson, Ricoh, Trident, Hitachi) are used due to its relatively simple manufacturing and integration. High integration densities are much more difficult with piezo inkjet compared to thermal inkjet due to the required deformation of the chamber, which is typically governed by the size of the piezo.

2.2 Droplet Generation with Piezo Inkjet Technology

The jetting of a droplet from an orifice is based on the creation of an overpressure behind the nozzle opening. The amplitude of this pressure needs to be high enough to overcome the viscous resistance, inertia and capillary pressure in the nozzle.

In piezo inkjet a force is created by a piezoelectric element as a result of the inverse piezoelectric effect,⁷² which exerts a deformation on the wall of a microchannel. Depending on the orientation of the electric field \mathbf{E} in relation to the elastic, electric and piezoelectric coupling tensors, expansion/contraction or shear motion can be realized. By adequate clamping this motion can result in an expansion, bending or torsion. The motion of a wall or channel results in a change of pressure Δp due to its change in volume ΔV , which can be expressed using the compressional modulus K of the ink by $-K(\Delta V/V)$.⁷³ As is evident, both positive and negative pressure amplitudes can be realized by an increase or decrease in chamber volume. With typical compression moduli of fluids being 2×10^9 Pa the required deformation $\Delta V/V$ to achieve approximately 2×10^5 Pa with a factor of safety of five for dynamic losses⁵ would be 5×10^{-4} .⁷³ A high positive pressure can be directly utilized to form a droplet but is commonly avoided due to limited breakdown field or the coercive field strength of the piezoelectric. Therefore wave superposition principles are commonly employed to minimize drive voltage requirements and electrical loss.

The pressure waves initiated by the deformation of the chamber travel along the length of the actuator with a phase velocity c_c in the channel. This velocity deviates from the speed of sound c_0 measured in the bulk liquid since the surrounding microchannel acts as a pseudo-compressibility through its compliance β . This can be described by

$$c_c \propto \sqrt{\frac{c_0^2}{1 + \rho c_0^2 \beta}}$$

where ρ is the density of the fluid and the proportionality is described by a geometry factor of minor influence.^{39,74}

Figure 2.2 depicts a typical driving scenario by taking the example of a Xaar-type hybrid-sideshooter printhead. In this case both ends of the channel are open to a large reservoir of fluid and the nozzle is located in the center facing downwards. The initial step change in the electrical potential difference across the PZT (a) widens the channel cross-section and two negative pressure waves start to propagate towards the ends of the channel. As both ends are open to a large fluid reservoir, the acoustic impedance discontinuity acts as an open end and initiates a 180° phase-change of the reflected pressure wave with some minor transmission loss due to imperfections in the reflection. These two waves of positive sign then travel towards the center of the channel and superpose. To enable an optimal superposition, the timing of the subsequent set of waves is aligned to half of the acoustic period t_a , which is prescribed by the damped natural frequency of the channel f_D^{-1} . This timing can, in a first order approximation, be related to the length of the channel l_c as $l_c c_c^{-1}$. Hence, after a time interval of t_a the electrical potential difference is removed from the PZT forcing the channel to contract and superpose two additional positive waves (d). The result is a sufficiently high

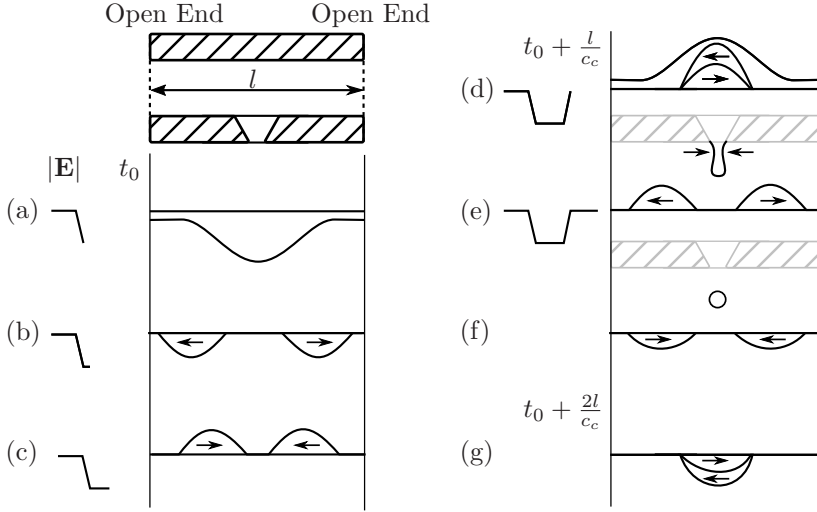


Fig. 2.2. Schematic pressure development in a side-shooter type printhead with both ends of the channel open to the manifold and the nozzle positioned in the center. The magnitude of the electric field $|E|$ indicates the electric drive to the piezo ceramic, where a more negative value relates to an increase in the channel cross-section.

pressure to deform the meniscus and force fluid to flow through the nozzle. As the waves continue to travel, an inversion of the pressure after another acoustic period will revert the flow in the nozzle and eventually force the meniscus inwards. The meniscus will, depending on the structural and viscous damping, continue to oscillate until the waves have died away.

The described sequence of pulses is the most simple arrangement for actuators employing the superposition of waves to minimize electrical drive power and is referred to as a unipolar pulse. Bipolar pulsing schemes are often employed to further optimize the efficient use of drive voltage at the expense of complexity in the drive electronics. In the case of a bipolar drive, the channel cross-section cannot only be relaxed to the quiescent state by the removal of the field but is actively reduced to create an even higher positive pressure. In addition the relaxation to a zero field can be timed in such a fashion as to quickly minimize residual oscillations in the channel by the superposition of out-of-phase pressure waves. The reduction of residual oscillations may also be accomplished by unipolar pulses. This is restricted, however, to the polarity of the wave in the channel being opposite to the canceling pulse. This typically results in longer waveform durations and consequently lower maximum actuation frequencies.

As the fluid is forced through the nozzle by the pressure, the surface energy of the meniscus is overcome and the fluid starts to extend out of the orifice as a circular jet. At this time the meniscus experiences an acceleration in the order of 10^6 m s^{-2} , where surface active molecules have insufficient time to diffuse to the newly created surface. The surface tension in this initial stage is therefore mostly related to that of the base solvent, which is approximately 72 mN m^{-1} for water and $20\text{--}40 \text{ mN m}^{-1}$ for organic solvents.⁴ In the initial stage the extension of the

jet is controlled solely by the inertial forces on the liquid filament, while at later stages surface tension and viscous forces govern the formation of satellites. As soon as the velocity of fluid flowing from the nozzle is lower than the velocity of the leading droplet, the fluid column closest to the nozzle will begin to reduce in diameter. This thinning can already induce backflow towards the nozzle before the pressure behind the nozzle has transitioned into the low-pressure regime and reverted the flow direction towards the channel.⁷⁵ The local reduction in diameter will trigger surface tension forces to minimize the surface energy and initiate the pinch-off process. The most likely position for this pinch-off is for low-viscosity fluids close to the nozzle and moves closer to the main droplet for higher viscosity, where the viscous effects counterbalance the growth of the instabilities. Depending on the acceleration of the meniscus, instabilities may be triggered on the meniscus surface, resulting in asymmetric droplet formation or the detachment of small droplets from the leading surface of the main droplet.^{76,77} The high surface curvature after pinch-off drives the tail towards the main droplet with a high velocity, which reduces as the tail accumulates volume. Upon merging with the main droplet a velocity increase of the final droplet is observed.

The fluid and its physical properties play a critical role in the drop generation process. The density ρ and the speed of sound c_0 , combined into the compressional modulus K as ρc_0^2 , relate the volume change of a chamber to the change in pressure inside the channel. The viscous dissipation inside the small channel impacts both the damping as well as the phase velocity, reflected in the reduced frequency, even when excluding the elasticity of the wall.⁷⁸ Viscous dissipation is commonly described by the Stokes boundary layer given by $\sqrt{2\eta/(\rho\omega)}$, where η describes the dynamic viscosity of the fluid and ω the angular frequency. Its magnitude for a typical resonance frequency of 200 kHz, viscosity of 10 mPa s and a density of 1000 kg m⁻³ is approx. 10 μ m and gives rise to appreciable contribution of the wall friction to the damping in the channel, while being dominant inside of the nozzle. For *Newtonian* fluids, viscosity is only dependent on the temperature. Temperature variations therefore impact the consistency of droplet formation due to a change of the damping of the traveling waves. This in turn has an impact on the pressure magnitude at the entrance of the nozzle, typically resulting in strongly increased droplet velocities as a result of an increase in temperature. The main sources for temperature rise are the energy dissipation from the piezo element and the electronics located close to the fluid path. Commercial printheads counteract these effects either through temperature compensating drive voltages⁷² or convective removal of heat using the ink as coolant.^{79,80} For *non-Newtonian* fluids, which exhibit shear dependent viscosities or viscoelastic properties,⁸¹ the behavior becomes more complicated due to altered timing and energy efficiency of the actuation as well as altered flow behavior at the shear rates of 10⁶ s⁻¹ inside the nozzle. Shear-thinning fluids were shown to produce satellite-free droplets as result of the strongly reduced shear-rate when the droplet has detached from the meniscus and the increased viscosity counteracts capillary break-up of the tail.⁸²

2.3 Print Artifacts

Commercial PIJ printheads have improved greatly over the last decades to provide substantial amounts of droplets per second and extended time between maintenance operations. This evolution is attributed to both an increase in understanding of the underlying phenomena of drop formation and their consideration in the design alongside with an improvement in manufacturing capability. However, there are still influences that deteriorate the printed product, such as satellite droplets, variations in velocity, volume or trajectory as well as nozzles ceasing to fire.

The following sections describe some of the challenges commonly experienced in inkjet printing, which result in artifacts in the printout.

2.3.1 Crosstalk

Crosstalk describes the interaction of an actuated channel with the neighboring ones. While there are other possible interactions such as electrical crosstalk in drive electronics, we will focus here on the phenomena introduced by the actuation, which can be defined as structural and fluidic crosstalk.

The change of cross-sectional area in an actuated channel will also trigger a deformation in adjacent channels, as these are not structurally decoupled from one another. Reasons are found in the design of the printhead, which has to consider trade-offs between stiffness and nozzle density. If adjacent channels are actuated simultaneously the crosstalk waves travel in-phase with the waves introduced by the actuation of that particular channel. If nozzles are being fired with a time offset, the timing and damping are important, which results in constructive or destructive interference as well as a reduced influence with an increased time offset due to viscous damping.

The shared-wall actuator used in our studies exhibits by design a very specific structural crosstalk. For an actuation the two walls of the particular channel that are shared with the neighboring channels (*cf.* Figure 2.3 (a)) move in opposite directions. The two neighboring channels therefore experience a pressure of half the magnitude and opposite sign of the active one, which is too low to eject droplet from the adjacent channels. At actuation of every second channel the intermediate channel will experience a pressure of opposite sign, but of the same amplitude as the jetting channel, which could result in sufficient pressure to eject so-called *accidental* droplets. Therefore only every third channel is actuated at a time, which reduces the print frequency by a factor of three. One workaround is the insertion of gas filled isolation channels. This implies reduction of nozzle density by a factor of two, but allows to fire all active channels simultaneously. It was shown that the elimination of this type of crosstalk could enable a threefold increase in productivity.⁸⁰

A second source for crosstalk results from the fluidic coupling of the channels through the shared ink manifold (*cf.* Figure 2.3 (b)). The varying pressure in channel or throttle act as point sources for pressure waves. The manifold allows waves to propagate and alter the pressure boundary condition at the inlet of other channels and initiate traveling waves. The time-dependent superposition of

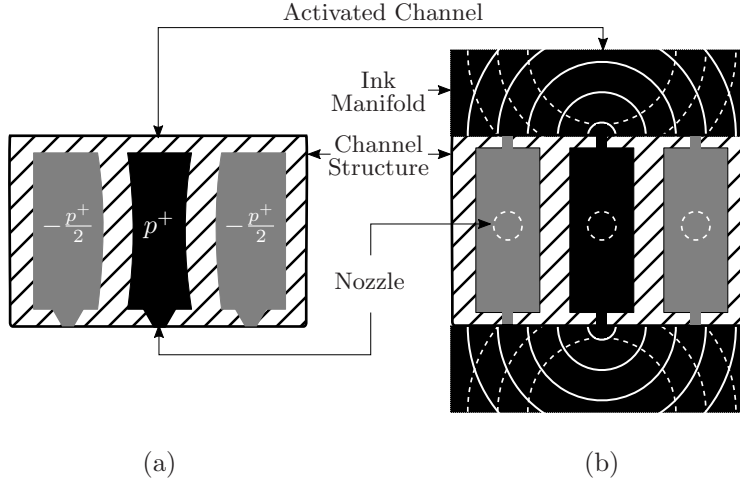


Fig. 2.3. Schematic representation of crosstalk induced in a printhead structure by actuating a single channel: (a) structural crosstalk in a shared wall actuator and (b) fluidic crosstalk created by the emanating wave (solid) and reflected (dashed) waves in the ink manifold.

those waves can have a noticeable impact on the jetting performance at different frequencies.⁸³ Therefore compliant features are often added to the manifold to aid the damping of the traveling waves.⁸⁰

One further type of crosstalk is commonly referred to as *in-channel* crosstalk. Here the interaction refers to the presence of residual pressure oscillations from a previous actuation. These interfere with waves generated in an actuation and result in a characteristic frequency response of both droplet velocity and volume. By considering only the last deformation in the waveform it was shown that the value of a damped cosine function can be used to predict the variation of the droplet characteristics at the different harmonics of the actuator. Relating the response to the damped frequency of the actuator with the intrinsic damping of the actuator-fluid combination shows the influence of the damping on the frequency response and allows for the extraction of these parameters from experimental data. Based on the reduced frequency f_D and the Q -factor of the actuator, a good first order approximation can be made to predict the behavior of the droplet characteristics without the requirement for jetting.⁸⁴

2.3.2 Air Ingestion

Acoustic variations inside or close to the channel alter the performance of the resonator and shift timings as well as achievable pressure amplitudes. Such variations can be present in changing boundary conditions at the inlet of the channel by the mechanisms described above, by an unbalanced ink system or blocking of channels by insufficiently stabilized particles.

Another strong interaction originates from the presence of an additional compliance in the form of micro air bubbles inside the channel. Air bubbles can be found in inkjet system by unbalanced menisci, water-hammer effects, cavitation on particles and anomalies in the negative pressure cycle as well as unsuccessful jetting of a nozzle or by nozzle plate flooding.^{34,85,86}

The bubble reacts on the acoustic field by compression and expansion. Specifically an expansion towards an equilibrium state of the bubble is observed when surpassing a threshold value. Rectified diffusion is observed, where the combination of effects relating to the surface area and interface collectively drive a net flux of dissolved gas from the ink into the bubble.⁸⁷ The surface effect relates to the increased surface area of the bubble during expansion which leads to a net flow of molecules into the gas volume. The interfacial effect influences the local gas concentration outside the bubble, which increases during expansion.

During continuous actuation of the channel bubbles therefore do not dissolve into the surrounding liquid and either drive frequency or amplitude need to be reduced to enable the gas to dissolve.^{5,88} Alternative approaches can be found in modern printheads, where convective removal of air bubbles is accomplished by continuous circulation of the ink through the channel.^{80,89–91}

2.3.3 Satellite and Mist Generation

The droplet formation, as briefly described in Section 2.2, does often not result in a single main droplet but is accompanied by a number of smaller, differently sized droplets. These can be classified by their momentum into satellite and mist droplets. Satellites possess sufficient momentum to reach the substrate in the vicinity of the main droplet whereas the low momentum of the mist droplets make them susceptible to air currents so that they accumulate in random locations in the printer. The droplet velocity will diminish as a function of time as Stokes drag acts on the moving droplets and is strongly dependent on the droplet size as well as the instantaneous velocity. Satellites and even small main droplets can reduce strongly in momentum, so that they can be classified as mist and will not reach the substrate in a controlled manner, which is challenging for distances between printhead and substrate larger than 1–2 mm.

Satellite droplets evolve from the filament after pinch-off, as the system strives towards a state of minimum surface energy. The growing instabilities in the filament will then result in local necking and disintegration, if the recoil time of the tail is larger than the capillary time $\sqrt{r^3\rho/\gamma}$.⁹² The source for this Rayleigh-Plateau instability is noise, which explains the random nature of the satellite break-up. As mass transport from the necking to the bulging region is required, viscosity does play a role in selecting the most unstable wavelength for break-up. This influence is more pronounced as the filament radius becomes smaller than the viscous length scale $\eta^2/(\gamma\rho)$. Discrepancies in estimated break-up times are attributed to an additional stabilizing mechanism, where the tension of the interface contributes to the damping of the growing instability.⁵

Secondary tailing is observed just before the pinch-off from the meniscus. As the neck decreases in size, the capillary pressure increases and a flow from the neck to the meniscus is initiated, leaving a thin filament. The opposing motion of the

tail and the meniscus exert a tension on the filament, which aids its stabilization to a diameter around 1 μm . At this scale the viscous length scale is more significant than the capillary one, which results in an increasing length of the filament with increasing viscosity. The mechanisms governing these processes are still not fully understood.³⁴

2.3.4 Nozzle Plate Wetting

The conditions on the nozzle plate are important for the consistent and directed acceleration of droplets towards the substrate. It is the component of the print-head that, apart from a nozzle guard, is exposed to the substrate and air-borne contaminants such as lint and satellites. Physical maintenance is therefore inevitable to keep the nozzle plate surface in clean and controlled conditions, but bears the possibility of physical damage to the front of the nozzle plate surface and the exit of the nozzle.

The presence of an ink layer at the nozzle exit or on the whole nozzle plate can have significant implications. Wetting of the area around the orifice can be attributed to the overfilling of the nozzle during refill.³⁹ Once contact of the ink inside the nozzle with the surface outside the nozzle rim is established will the combination of the surface energies at the triple point ink–nozzle plate–air determine the behavior. The contact angle θ is typically used to discriminate between wetting or non-wetting behavior, where contact angles below 90° are considered wetting. This value is strongly dependent on the ink chemistry as well as the nozzle plate material and is for inkjet inks commonly found to be below 30° . For wetting nozzle plates an ink film of the order of 10 μm is often observed, which affects the droplet formation by reducing the droplet velocity due to the increased inertia.

A second implication of an ink layer on the nozzle plate is the transport of debris towards the nozzle. As the ink droplets leaving the nozzle carry air with them, an airflow towards the jetting nozzle to equilibrate the created pressure gradient can be observed. This airflow is capable of creating a Couette flow in the ink layer on the nozzle plate towards the nozzle.³⁹ Also Marangoni flows were shown to create a transport of fluid towards the nozzle.⁹³ Both flow scenarios transport ink as well as debris towards the nozzle, which may result in trajectory deviation of ejected droplets or nozzle failure.

Some commercial printheads employ special non-wetting coatings or physical barriers to prevent wetting of the nozzle, especially at high ejection frequencies, where the time intervals between ejections can be short enough to prevent the retraction of the meniscus into the nozzle. In this case the ink remains constantly in contact with the nozzle plate and can swiftly result in nozzle plate flooding. Non-wetting coatings in practice are challenging, as they are strongly dependent on the ink chemistry and are prone to deterioration through mechanical or chemical interaction.

The challenges to print quality and reliability outlined in this chapter are key to the implementation of single-pass, high-throughput as well as functional applications where the presence and exact placement of every droplet need to be ensured.

An experimental assessment requires to consider both, the time scales and length scales involved in the process. The time scales relate to that of droplet formation ($<300\text{ }\mu\text{s}$), the wetting of the nozzle plate (ms to minutes) or the interaction with contaminants in the printing process (minutes to hours). The length scales in contrast range from $1\text{ }\mu\text{m}$ for secondary tailing, $20\text{ }\mu\text{m}$ for the main droplet size, to the nozzle spacing of $100\text{ }\mu\text{m}$ and to the full printhead of 100 mm to meters in the printer's writing system.

The following chapter will show our approach on advancing the understanding of the characteristics at the different scales, to improve the laboratory assessment of the jetting process.

Measurement Techniques

The evolving inkjet technology lead to increasingly complex printhead arrays, comprising thousands of nozzles, typical droplet sizes in the order of 5 pL and repetition rates of 100 kHz, which requires accurate mathematical models as well as fast and reliable measurement techniques.

Inkjet printheads present a multi-scale problem, which involves high velocities of 10 m s^{-1} as well as the length scale of droplet formation alongside with the dimensions of a physical printhead and printing systems, which commonly span five orders of magnitude. Therefore temporal resolutions of hundreds of nanoseconds with spatial resolutions in the sub-micrometer range would be required. As this is challenging, problems typically are separated into either scale of the printhead operation in both modeling as well as metrology.^{73,94–96}

The following sections provide an introduction to the two methods investigated in this thesis. Firstly we aim to provide an insight into the ejection of a single droplet from a nozzle in time. The second section in contrast displays a method to investigate the full printhead width and all ejected droplets.

3.1 Imaging Methods for Single Droplet Studies

Many studies focus on the predictability of jetting behavior on dimensionless numbers such as Ohnesorge Oh, Deborah De and elasto-capillary number Ec.⁹⁷ However, correlation of satellite and mist formation is especially challenging, where the break-up is influenced by perturbation introduced by the printhead or other noise sources leading to capillary break-up of filaments. In addition physical properties of complex ink formulations are often unknown in the present stress state. Observing one single droplet during its formation is therefore of high interest to understand the flows inside a droplet based on the local surface tension-induced deformation. This would be a suitable extension of the recently published tracking of volumetric flow inside a contracting primary tail.³⁰

Two competing techniques are commonly employed to visualize droplets in flight, namely stroboscopic and high-speed camera imaging. In stroboscopic imaging, pulses of light are synchronized with the ejection of a droplet to project the shadow of the droplet onto a high resolution CMOS or CCD chip. Depending

on the shutter times available, single droplets or an average of many droplets will be recorded, which provides a medium to high quality shadowgraph of the droplet. Typical systems employ high power LEDs with pulse widths shorter than 200 ns to minimize motion blur. The techniques will sharply image the reproducible part of the droplet and tail formation, but will fail to give a concise image of the time development related to the random nature of the tail disintegration. These techniques strongly increased in fidelity with ultra-short light pulse sources as in the spark flash approach and illumination by laser-induced fluorescence (ILIF).^{35,98} Furthermore improvements were proposed to overcome the limited contrast in multi-flash imaging using multi-wavelength illumination in conjunction with spectrally separated recording.⁹⁹

Another approach uses a constant illumination along with a high-speed camera. To photograph a droplet ten times, when traveling from the nozzle plate to the substrate, approximately 10^5 frames per second (FPS) are required. Considering the available pixel throughput of the cameras, resolution needs to be reduced in order to facilitate a fast read-out. Available shutter times further limit the resolution of the recording. The result is the possibility to record a single droplet on its trajectory away from the nozzle plate, but with limited spatial resolution.

The approach presented in this work attempts to overcome the limitation by using a high resolution camera in combination with a resonant micro-mirror and a laser producing a train of short light pulses.

3.1.1 Experimental Setup

Figure 3.1 presents the working principle of the developed method. As in conventional stroboscopic illumination techniques light pulses are synchronized between the printhead and the camera. A non-circular spot produced from a laser diode

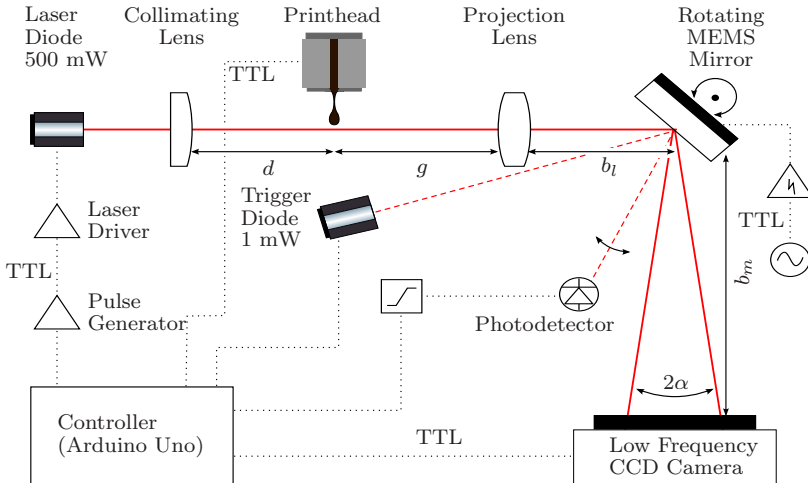


Fig. 3.1. Schematic beam path and triggering circuit as used in the developed multi-pulse imaging technique.

is collimated and produces a sharp projection of the droplet's shadow on a CCD sensor. On the projection side of the setup the optical path is being diverted using a resonant MEMS micro-mirror, which distributes the snapshots of the moving droplet across the CCD sensor. By considering the angular velocity of the mirror and droplet velocity, it is possible to image multiple stages of drop formation along the trajectory.

In order to facilitate a sharp reproduction of a moving object, motion blur is a key challenge that requires attention. A common approach is to limit the motion of the object to 10% of its characteristic size during an exposure. For a feature resolution of $5\text{ }\mu\text{m}$ and an object traveling at 10 ms^{-1} , a maximum illumination time t_{ill} of 50 ns is required. This illumination time restricts the choice of illumination sources, as a high photon flux is required to allow for a good signal-to-noise ratio (SNR) on the sensor. To achieve this, the light source needs to produce a sufficient number of photons to account for losses in reflection and absorption in the optical path. A laser emitting at a wavelength λ and a power P produces during the illumination time $\lambda Pt_{\text{ill}}(hc)^{-1}$ photons. Here h is Planck's constant and c the speed of light. To establish an estimate for the SNR, the number of incident photons is compared to noise sources, i.e. photon, dark and read-out noise. Assuming the dark noise to be nil for the short exposure times considered, the number of photons required per image pixel is given on the left-hand-side of Equation 3.1, whereas the right-hand-side gives the total number of photons per pixel provided by the laser.

$$\frac{\text{SNR}^2}{2Q_e} \left(1 + \sqrt{1 + \frac{4\delta_r^2}{\text{SNR}^2}} \right) \ll \frac{\lambda Pt_{\text{ill}}}{n_{\text{pix}}hc} \quad (3.1)$$

Here Q_e is the quantum efficiency of the sensor, δ_r is the read-out noise and n_{pix} is the number of pixels to be illuminated. Using Q_e of 0.5, a SNR of 20,¹⁰⁰ an assumed read-out noise of 10 electrons, the number of illuminated pixels to be $128 \times 960\text{ px}^2$, a wavelength of 630 nm , a power of 600 mW as well as the estimated illumination time of 50 ns , we find that such a light source produces 800-fold the amount of photons required to illuminate the strip on the CCD.

Triggering was implemented using a microcontroller (Arduino UNO, IT) with a clock frequency of 16 MHz . Using the standard libraries simultaneous opening of the camera shutter and start of the print was realized. The laser was triggered with an offset until droplets were visible on the screen and then triggered in intervals of $10\text{ }\mu\text{s}$ within the error of the available delay functions. To convert the signal from the microcontroller to the short pulses required to drive the laser diode, a monostable multi-vibrator (DM74123, Fairchild, US) was fitted with $5\text{ k}\Omega$ resistor and a capacitance of 1 pF to create a nominal pulse-width of 50 ns . This pulse was fed into a dedicated laser trigger circuit (iC-HG HG1D, iC-Haus, DE), which then connected to the laser diode (ML520G72, 600 mW , Mitsubishi Electric, JP). Measurements of the light pulse confirmed a pulse width of $32.6 \pm 0.5\text{ ns}$.

In order to image the shadow of the droplet at subsequent instances across the CCD sensor, the half-angle α_m of the required rotation of the micro-mirror can be computed using

$$\alpha_m = \tan^{-1} \left(\frac{w_s}{2 b_m} \right)$$

where w_s is the width of the sensor and b_m is the distance between the mirror and the sensor. For the given sensor (ICX445, Sony, JP) and b_m of 100 mm this results in a tilting angle of 1.37° . Given a typical transit time of the droplet over the distance of interest of $100 \mu\text{s}$, this translates into a resonating frequency of 5 kHz and, hence, a speed of the beam on the CCD of 48 m s^{-1} . Recalling the discussions of motion-blur and considering an illumination time of 50 ns this decreases the resolution to a minimum spherical feature of 5.4 pL .

The change in path length due to the tilting of the mirror can be estimated using the Pythagorean theorem. In this fashion using b_m of 100 mm results in a difference of $29 \mu\text{m}$, which is insufficient to blur the image as it is smaller than the depth of field.

3.1.2 Results and Discussion

Figure 3.2 shows the recording of a single droplet ejected from a Xaar 126 printhead with a nominal volume of 50 pL. The sinusoidal distribution of the mirror motion was removed from the image for cosmetic reasons.

The image sequence starts with a droplet fully ejected from an inkjet nozzle. Note the tail-hook close to the main droplet in (1), which moved along the filament during the course of time as a result of the local tension of the thinning filament as well as its local rheological properties.⁹⁵ The beginning disintegration of the filament started after approximately $30 \mu\text{s}$ (4) and progressed all the way through (6), where the final stage with a connection between the lower and the upper part of the filament is visible. As the tail disintegrated in this sequence, we

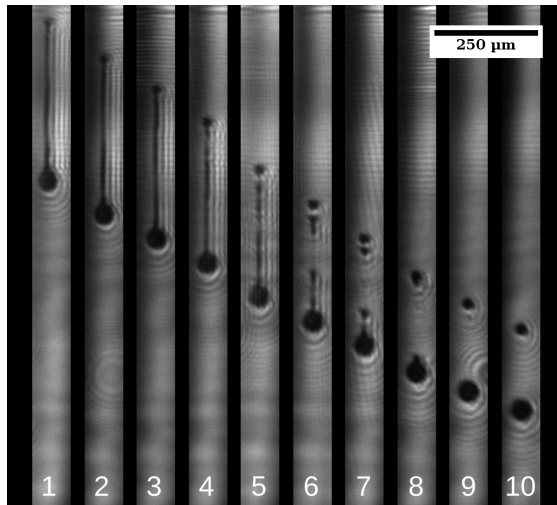


Fig. 3.2. Droplet formation from a Xaar 126 50 pL printhead as recorded with the multi-exposure system. [Analogue ink, v_d 6 m s^{-1} , Δt $10 \mu\text{s}$, VHDL voltage 3.4 V, $V_{\text{mirror,pp}}$ 110 V]

could observe the detachment of the tail bead with the formation of a secondary tail in (5). This was followed by the decomposition of the residual filament into two parts, one connected to the main droplet and another one associated with the lower part of the remaining filament by a secondary tail in (6). This secondary tail, stabilized by its tension and viscosity eventually broke up into multiple small particles as is visible in instance (7). These merged eventually with the satellite approximately $20\text{ }\mu\text{s}$ later. The disintegration of such thin filaments is the main driving force for the generation of mist. From instance (8) onward, surface tension had minimized the surface energy by creating round droplets, which now travel at a relatively constant separation, i.e. velocity, onward. Note also the drag-induced deceleration of the 50 pL main droplet, which could be estimated from leading edge of the droplet, to reduce from approximately 6 m s^{-1} at the beginning to 4.5 m s^{-1} at the end of the sequence.

The quality of the images presented in Figure 3.2 was sufficient to perform the qualitative descriptions given above but poses challenges to the quantitative assessment with image analysis techniques. An obvious challenge was the limitation of the quality by the diffraction fringes created as a result of the coherent light source. Techniques for overcoming this limitation are presented in the literature,³⁵ but the limited energy of the used light source in conjunction with the quantum yield of the fluorescent dyes were prohibitive for the application in this setup.

A second challenge is the pixel size of the sensor, which also relates to the number of photons required for good contrast. Increased pulse energies would enable the usage of higher resolution sensors, but given the motion blur in the current system only a reduction in illumination time would be beneficial.

An error source introduced by the current setup was the angular velocity of the mirror sweeping across the CCD array. With a typical transit time of the droplet of $100\text{ }\mu\text{s}$ and the width of the used sensor being 4.8 mm , the image moved with 48 m s^{-1} across the sensor and introduced motion blur, limiting the reproduction on the sensor to 2 pixels. Limiting the resonant frequency of the mirror to $3\text{--}4\text{ kHz}$ may present a reasonable compromise between resolution and the transit length that can be imaged.

Lastly, triggering of the illumination in the current implementation was limited, as the internal accuracy of the microcontroller's *delay*-function was bound to an accuracy of $\pm 4\text{ }\mu\text{s}$. Such a deviation can be detected in Figure 3.2 (5) indicating the triggering light pulse is delayed.

3.1.3 Summary

We could show that a MEMS micro-mirror can be used to project the shadow image of one and the same developing inkjet droplet during its travel from the nozzle plate to the nominal throw distance of 1 mm . The development of multiple satellites alongside with secondary tail formation was visualized between the developing fractions of the main tail. The formation of mist droplets from the secondary tails that merged with trailing satellites could be observed.

Despite being limited by the light source and trigger circuit used, the basic applicability of the technique could be shown and further improvements were

proposed and would be readily available. With the discussed improvements in the light source, diffraction patterns could be omitted and would improve background homogeneity as well as contrast at the droplet contour. This consequently opens up the analysis using improved image processing algorithms as presented in the literature.^{30,101}

3.2 Qualitative Reliability Assessment by Measuring Every Droplet

Reliability refers to the presence and full functionality of all jets and is dependent on many input parameters such as print pattern and duty, temperature fluctuations, meniscus pressure variations, external vibrations as well as the condition of the nozzle plate. The main driving mechanisms leading to an outage of a nozzle were discussed in Section 2.3.

Reliability is commonly measured very late in the development process by printing onto media and visual inspection. This has strong implications on the cost and time of process development due to cost of ink, media as well as labor to estimate the failure statistics qualitatively at best. It is therefore desirable to include reliability assessment early on in either the printhead or during waveform development using droplet-in-flight systems. The developed waveform can be swiftly screened for any crosstalk related deficiencies by using a set of typical print patterns. In addition the destabilization of the ink system due to water hammer or air ingestion can be studied.

In the following sections we analyze different approaches with respect to their applicability in the waveform design cycle and present an alternative approach to the evaluation of printhead reliability.

3.2.1 Reliability Measurement Approaches

A conclusive answer as to whether a firing event was successful is given when a droplet of the desired size, velocity and trajectory is propelled from the nozzle towards the substrate. Measuring all these characteristics in the gap of typically one millimeter between the printhead and substrate is very challenging due to the limited accessibility. Hence, there is a desire to measure the success of a firing event already inside the printhead on the actuator level, where the feedback can be directly used to employ various compensation and redundancy schemes or to trigger a maintenance cycle.

Acoustic Response Measurement

A piezoelectric material can act both as an actuator as well as a sensor by employing the inverse and direct piezoelectric effect, respectively. In the latter case, the pressure in the channel results in a net charge in the ceramic, which is proportional to the applied force exerted by the pressure.¹⁰²

The generated charge can be measured using a charge amplifier, an impedance converter or a sensing resistor. The observed charge-time relationship does not

directly provide information about the traveling waves, as it represents a superposition of the charge currently stored and moved in the capacitance of the dielectric layer as well as the charge generated by the pressure distribution across the surface of the piezo.³⁹ Hence, the total current can be represented as

$$i(t) = C_p \frac{dv(t)}{dt} + d_p b_p \int \frac{dp(z, t)}{dt} dz \quad (3.2)$$

where i is the current, v is the voltage across the piezoelectric element, C_p is the capacitance, d_p is the piezoelectric coefficient in the direction of the applied force, b_p is the width of the sensor, $p(z)$ is the pressure at any given point along the channel and t is time. From Equation 3.2 it is apparent that the dimensions of the actuating-sensing element with respect to the channel are important in the interpretation of the results, as the charge is integrated over its length. A challenge is posed by the difference in amplitudes between the displacement current originating from the capacitance and the generally very low signal from the pressure-induced charge. Several methods have been proposed to eliminate the influence of the capacitor charging from the signal, which include the application of a switching circuit, which ensures the complete discharge of the capacitance before the measurement of the pressure signal. A second approach extends the measurement circuit with an equivalent electrical capacitance into an electrical bridge circuit,³⁸ which is then used to remove the capacitive part from the measurement signal.

The resulting signal comprises several key features that may be utilized to assess the channel's condition. deJong *et al.* investigated the signal in depth and concluded the variance of the acoustic signal between ejections of 50 μ s is sufficient to determine for instance the presence of an air bubble in the ink within the channel, as the compressible gas absorbs a majority of the acoustic energy.⁸⁵

By analyzing the frequency spectrum of the acquired signal, the natural frequency of the resonator can be easily determined.¹⁰³ Any disturbance altering the acoustics in the channel, such as the absorption and reflection of acoustic energy as a result of an air bubble, clearly changes the intensity and location of the fundamental tone. This influences the optimal superposition as well as amplitude of waves and results in insufficient energy available for the ejection of a droplet.

Figure 3.3 shows the Fourier spectra for air bubbles positioned at different locations along the channel of a side-shooter printhead. Compared to the undisturbed channel, all measurements depict a clear reduction of the peak amplitude along with changes in the maximum positions as a result of the reflection from the air inclusion. Other local maxima appear due to the two-way coupling between the acoustics of the channel and the oscillations of the bubble.¹⁰⁴ Placement of the air bubble close to the center of the channel (1.0 mm) results in two equally sized resonators with half the length of the channel and consequently twice the resonating frequency. Here a harmonic of the resonator is excited and the waves experience a minimum of damping. The fundamental tone remains present with a strongly reduced magnitude. When moving the bubble along the channel, the secondary resonator does not gain significantly in amplitude due to the frequency filtering characteristics of the channel and most likely the low signal-to-noise ratio. Only some minor peaks do appear at intermediate frequencies. When moving

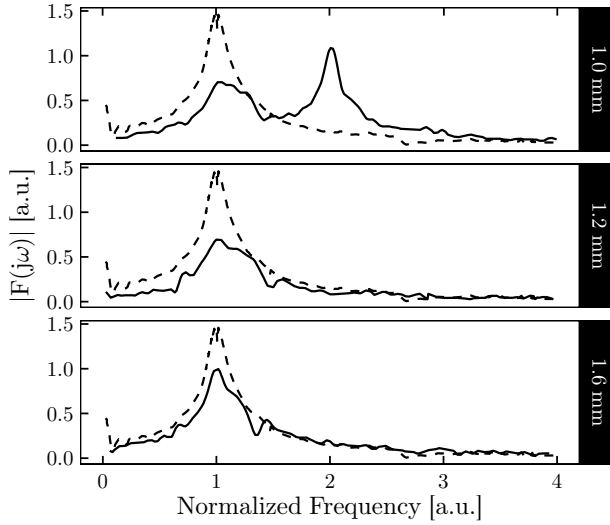


Fig. 3.3. Fourier spectra of measurement signals from printhead with an air bubble purposely located 1.0, 1.2 and 1.6 mm away from the entrance of a 1.8 mm long channel as a function of frequency normalized to the natural frequency of the channel. The undisturbed channel (dotted line) is shown for comparison [data reprinted from Sack¹⁰³].

the disturbance to the edge of the channel the fundamental tone is nearly fully recovered. It can be assumed that in the scenario depicted in Figure 3.3 (1.6 mm) the channel becomes operational.

The information that can be gained from the acoustic monitoring gives a representative image of the operational state of the channel and is used in the high-end segment of printheads due to the implications of the complexity of the ASIC design.^{105,106} With the additional functionality in place, these metrics can be successfully used in the optimization of waveforms for the optimal active damping of the channel for high-speed jetting.^{36,37,107,108}

Capacitive Sensing of the Meniscus

Sensing of the meniscus position offers the possibility to investigate potential failures closer to the final ejection of the droplet.

Wei *et al.* presented a method for the inline measurement of the filling of an inkjet nozzle using a capacitive sensor with a resolution of 10 aF. The sensor employs a three electrode arrangement for optimal coupling and reliable detection. The measurement concept is based on the lock-in principle in order to separate the low sensor signal from other noise sources such as $1/f$ noise. Using their approach, the authors could demonstrate the motion of water exiting from the nozzle of a printhead. The sensor was capable of monitoring the forward movement of the meniscus until the capacitance was maximized before the fluid retracted back into the orifice. The measurement signal then followed the damped residual oscillation of the meniscus inside of the sensor cavity.

While the overall principle was demonstrated, the integration into a full, industrial-scale printhead remains challenging. The prospective integration into a nozzle plate, however, offers a scalable alternative to on-printhead monitoring of nozzle health.

Ernst *et al.* presented a similar technique, but aimed at large drop volumes of nanoliters, which is often used in jetting of biological materials. Their sensor is positioned away from the printhead and consequently measures a droplet in flight. The employed half-shell electrodes are surrounded by a grounded guard ring to shield the sensitive measurement from external influences. The resulting time signals were used to deduce empirical correlations to droplet velocity and volume. The major challenges for its application to picoliter-sized droplets are reported by Wei *et al.* and relate to improving the robustness for lower droplet volumes and higher droplet velocities. Challenges remain in the scalability of the device in conjunction with the accurate positioning in the vicinity of a nozzle plate, specifically considering trajectory variations.

Superimposed Imaging

An alternative approach was presented by Renner,⁴⁰ where droplets are imaged onto a low-cost camera using multiple LED flashes synchronized to the ejection of the droplets. With the use of a long exposure time, the shadows of multiple droplets are captured. The result is a linear relationship between the number of droplets present in a camera frame and the gray-level at the nozzle position, such that dark areas indicate the superposition of multiple drops.

Local and temporal variations in the illumination require calibration and local background removal to extract characteristics of the nozzle.

Linear Contact Image Elements

Detecting the errors originating from a non-firing or misbehaving nozzle is straight-forward in a final print and are implemented in many machine concepts.¹⁰⁹ In these scenarios a linear contact image sensor (CIS or Image on Web Array sensor - IOWA) is used to digitize the printed image during printing. With typical resolutions of 600 or 1200 DPI in cross-print direction and line rates of tens of kilohertz this technique can be used both for analyzing missing jets and initiate compensation. Including the gray-level response of a pre-calibrated sensor it is possible to detect the location of a firing nozzle with sub-pixel accuracy and hence allow for digital alignment of printheads.¹¹⁰

While this technique provides the required statistics this approach still requires jetting onto a media and therefore can only find limited application in drop-in-flight systems.

3.2.2 Linescan In-Flight Imaging

We attempt to enable a printhead independent analysis by the linescan method proposed below. We overcome the limitation of high-speed imaging typically used in high-resolution droplet imaging and the limitation of the field-of-view typically

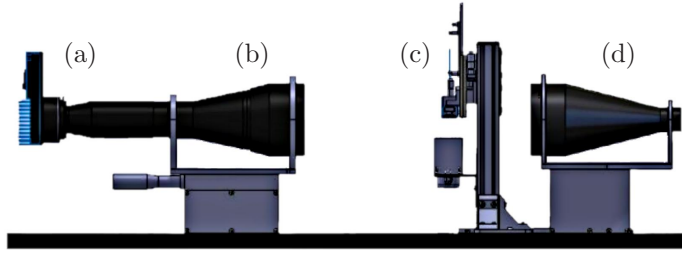


Fig. 3.4. Schematic layout of the experimental setup. (a) linescan camera, (b) telecentric projection optics, (c) printhead and catcher, (d) telecentric illuminator.

encountered by high frequency imaging techniques. This is possible because the information required for determining the presence of a droplet can be condensed into a single line and a few lateral pixels, which are recorded at high frequency using a linescan camera. In this fashion a printhead may be imaged over its full width at frequencies up to 120 kHz.

Figure 3.4 shows a schematic representation of the experimental setup. In order to image the full width of a printhead as well as allowing for multi-row printheads to be imaged, a telecentric imaging setup is essential and realized using a custom telecentric lens (Magnification: 0.3x, Opto-Engineering, Italy) with a complementary illuminator. The linescan camera (Piranha3, Teledyne Dalsa) and the printhead are synchronized and triggered externally through a CC320 timing controller (Gardasoft, UK).

By recording the printing process in a line-by-line fashion, the resulting image comprises the information of all the nozzles horizontally in the image, while the time is represented in the vertical direction. Here every pixel represents the state of the nozzle for the exposure time t_e of the camera. To ensure that the full information is being captured it is practical to oversample the ejection event, which for the given printhead configuration in three-cycle mode, is naturally given by selecting the camera frequency f_{cam} equal to the cycle frequency of the printhead. In this fashion three pixels in the vertical direction hold the information of a droplet and allow reliable detection even with variations in droplet velocity v_d or the position of the nozzle plate x_0 .

One of the challenges in the implementation of this technique is the requirement for a constant background illumination due to the statistical distribution of droplet velocity jitter and variation of the starting positions across the width of the printhead. While stroboscopic illumination would be beneficial to optimize contrast, the limited field of view along the droplet trajectory of approximately $20\text{ }\mu\text{m}$ and the residence time of the droplet of $4\text{ }\mu\text{s}$ within the field of view render this option impractical. The exposure time was chosen to be the inverse of the camera frequency reduced by a short read-out time of the pixels. Assuming a droplet velocity of 5 ms^{-1} , a field of view of $20\text{ }\mu\text{m}$ and a camera frequency of 18 kHz, the droplets reside in the field of view for $4\text{ }\mu\text{s}$ out of a $55\text{ }\mu\text{s}$ exposure. This equates to only a 7% difference in photon influx between fore- and background pixels.

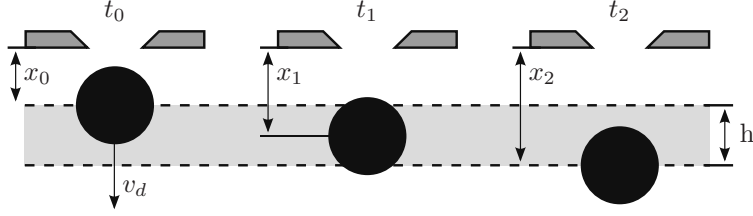


Fig. 3.5. Schematic representation of a droplet at a velocity v_d moving through the field of view of the camera of size h at times t_0 to t_2 with the corresponding distances traveled.

To estimate the resulting gray-level distribution a one-dimensional model was devised. The transition of a droplet through the imaging area as shown in Figure 3.5 can be modeled as a convolution of three functions. The droplet possesses a diameter d and travels at a velocity v_d . Hence, the cast shadow f_d can be written using the boxcar function Π as

$$f_d(x, t) = 1 - \Pi_{0,d}(x - v_d(t - t_d)) \quad (3.3)$$

where t_d is a system-based lag.

The linear imaging array is placed at a distance x_0 from the printhead and has a finite length h along the droplet trajectory. The exposure time of the camera t_e can be delayed by t_0 to aid matching the position of the droplet to the exposure. The equation for the camera can therefore be written as

$$f_c(x, t) = \Pi_{0,h}(x - x_0) \Pi_{0,t_e}(t - t_0) \quad (3.4)$$

To calculate the normalized intensity reaching the image sensor Equations 3.3 and 3.4 are multiplied and integrated in both time and space to represent the intensity I . To find an equivalent to the gray representation in an image, we divide the found intensity with the intensity I_0 of the camera without the droplet to define the ratio I/I_0 . This has the value of unity when no shadow is recorded and zero, when the pixel is blocked for the whole exposure.

Figure 3.6 shows a summary of a Monte Carlo-type simulation, where the input parameters camera frequency f_{cam} , starting position x_0 and droplet velocity v_d were varied for a grayscale printhead with 40 pL subdroplet volume. It is obvious that for a exposure time of 55 μ s, or 18 kHz cycle frequency, the shadow cast onto the sensor was weak and showed a difference of 20% in photon flux. It is noteworthy that this difference equated to twice the amount of the rough calculation presented above, as now the physical size of the droplet was taken into account. For significantly smaller droplets did simulations show a 10% difference in photon flux. The sensitivity to variations in velocity as well as starting position for the 18 kHz case were minute, as the long exposure time minimized these effects on the final result. The challenges were much more pronounced for higher camera frequencies, where the contrast was expected to increase due to the shorter exposure time. However, the distributions broadened as a combined effect of the variations in droplet velocity and the resulting residence time and also due to

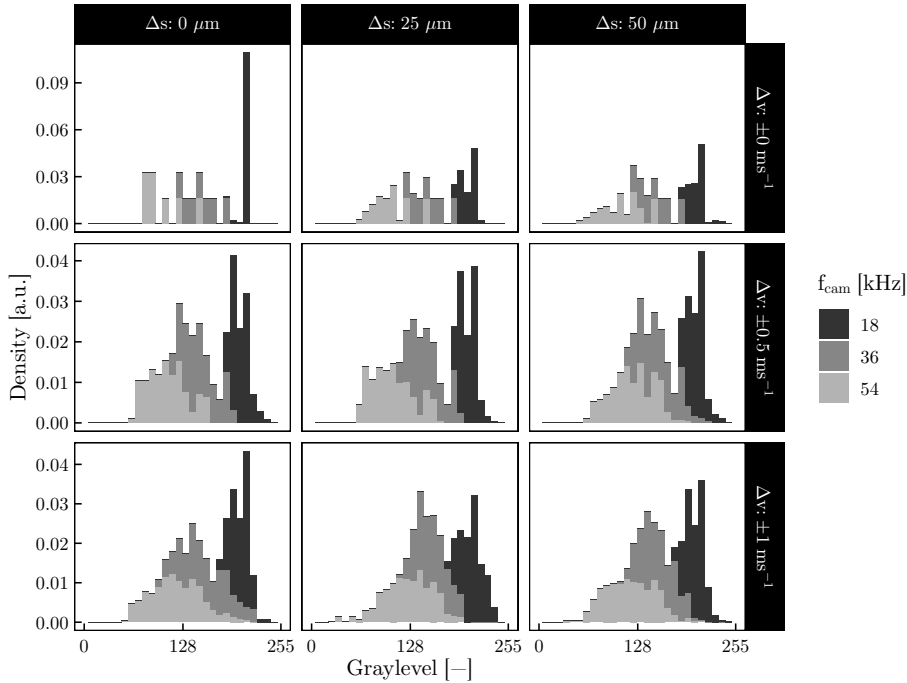


Fig. 3.6. Simulated gray-level distributions for one to seven drops-per-dot gray-levels at different camera frequencies. [stacked histogram, nominal droplet velocity 6 ms^{-1} , camera position $250 \mu\text{m}$ from the nozzle plate, sub-droplet size: 40 pL , Δs variation in starting position, Δv variation in drop velocity]

a segmentation of a firing event onto subsequent exposures. This resulted in a reduced contrast but increased numbers of darkened pixels.

3.2.3 Low Contrast Handling

The low contrast complicated the thresholding of the images, as the two normal distributions N_d and N_b , describing the gray-levels of the droplets and the background, respectively. With the known locations of the droplet pixels in the image, the actual distribution of grayvalues for fore- and background can be extracted. Histogram matching was therefore devised to divide the distributions with minimized uncertainty in the overlapping region.¹¹¹ Histogram matching is based on the two-fold application of a histogram equalization operation, which uses the inverse of the cumulative distribution function (CDF) to force the histogram to linearly grow within the interval $[0, 255]$ (*cf.* Figure 3.7). Applying this operation to the distribution found in the source image and a desired destination distribution, the matching can be accomplished by a simple nearest-neighbor allocation.¹¹¹

Figure 3.7 illustrates this transformation. The source distribution N will be transformed with the scaling factors s for the amplitude, s_μ for scaling the distribution mean and s_σ for standard deviation. These factors are chosen for both

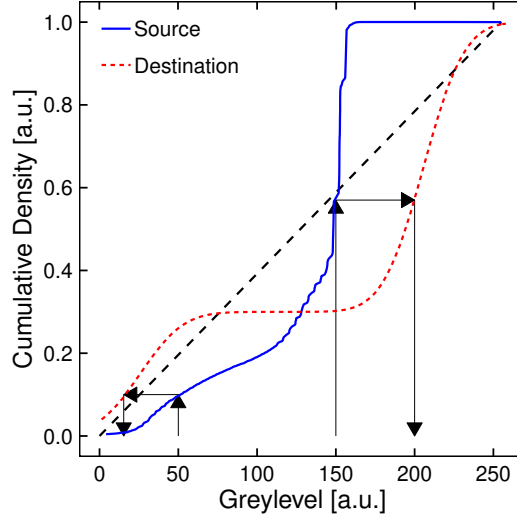


Fig. 3.7. Cumulative distribution functions for the source and the destination image with two examples (indicated by the arrows) of how the gray-levels are mapped. The arrows show the histogram matching operation by selecting a gray-level in the source image and finding the corresponding gray-level in the destination image via the linear distribution function of a histogram equalization operation [$s_d=0.3$, $s_{\mu,d}=0.5$, $s_{\sigma,d}=1$, $s_b=0.6$, $s_{\mu,b}=1.5$, $s_{\sigma,b}=1$].

the droplet (d) as well as the background (b). The sum of the two newly created distributions will then be used to define a look-up-table (LUT) to transform the gray-levels of the source image to match the prescribed distributions.

3.2.4 Analysis Results

A combination of preflight techniques was executed sequentially to optimize contrast and enable the discrimination between the present or missing droplets. Figure 3.8 summarizes the steps undertaken to achieve an analyzable image. We first used a linear grayscale erosion element to reduce the influence of the background pixels in the vicinity of the droplet. As a next step the dynamic range was maximized by stretching the histogram with the exclusion of the outliers at either side to the full scale between $[0,255]$. Subsequently the statistics were calculated and histogram matching applied to yield a clear separation of the background and the foreground pixels, which facilitates the choice of the threshold value.

Many different parameters, such as average, standard deviation, minimum and maximum calculations as well as morphological features can be used for describing the characteristic of an area of interest (AOI) around the dedicated droplet position. We focus here on an implementation using the minimum gray-level value. If the minimum gray-level is above the threshold calculated from the histogram, then the AOI does not contain a droplet. Further information is provided by the location of the minimum within the region under investigation.

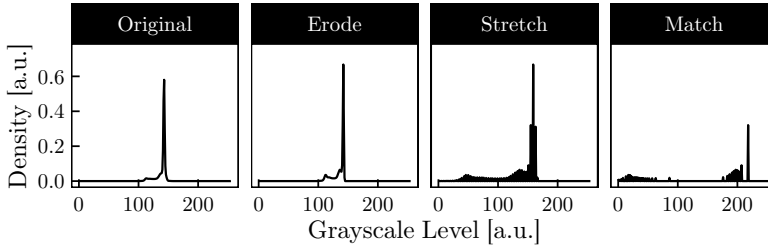


Fig. 3.8. Histogram development as a result of the application of the selected preflight techniques: (1) Original, (2) Eroded with a 3×1 element, (3) Stretched histogram within [104, 167], (4) Histogram matching with $s_d=0.3$, $s_{\mu,d}=0.5$, $s_{\sigma,d}=1$, $s_b=0.6$, $s_{\mu,b}=1.5$, $s_{\sigma,b}=1$ [Xaar 1002GS40, 6 kHz printhead frequency].

In this fashion one can observe lateral variations as well as velocity variations when choosing a two-dimensional AOI.

Figure 3.9 (b) shows the composite results image, where the results are coded using different gray-levels. Figure 3.9 (c)-(g) show the decoded results. In this experiment the print pattern shown in Figure 3.9 (a) was printed with a purposely detuned waveform to promote unstable jetting and thus providing numerous missing droplets or drops with large velocity variations.

Figure 3.9 (c) shows the failure of a single nozzle, which exhibited a start-and-stop failure behavior most likely due to debris in the vicinity of the nozzle, which moved during the continuous actuation. The potential air ingestion as a result of a failed nozzle was then removed by the convective flow through the channel and resulted in the nozzle operating again. The disturbance, however, was not fully removed as the nozzle repeatedly failed towards the bottom of the image. This method obviously yields statistics on the length of the outage, recovery times and influence on the neighboring channels.

Furthermore the technique can give information on the drop velocity variations. Figure 3.9 (d) and (e) are velocity indications based on the analysis of a 5×3 AOI. The variation of the nozzles surrounding the failing channel seen in (c) was visible, which resulted from altered crosstalk or the movement of fluid from local flooding on the nozzleplate. Figure 3.9 (e) depicts a pronounced wavelike pattern in the class of slow droplets. Here the start-up of a 100% duty print pattern induced an oscillation most likely due to the insufficient active damping in the detuned waveform. When changing to a lower gray-level, which maximized the time available for damping in the channel, this oscillation disappeared and did not reappear until the next block of the highest gray-level was triggered close to the bottom of the image.

The graphs in (f) and (g) can be used as control figures, when applying the linescan methodology to a vast number of images. The *ghost* droplets refer to droplets in designated white areas in the print pattern. These can be related to mist and satellite droplets remaining in the field-of-view or an erroneous image matching as a result of an image shift or mistriggering. *Untrustable* AOIs are used to categorize events where the variance of an AOI is essentially nil and the mean suggests a black pixel. This is often observed in the case of flooding on

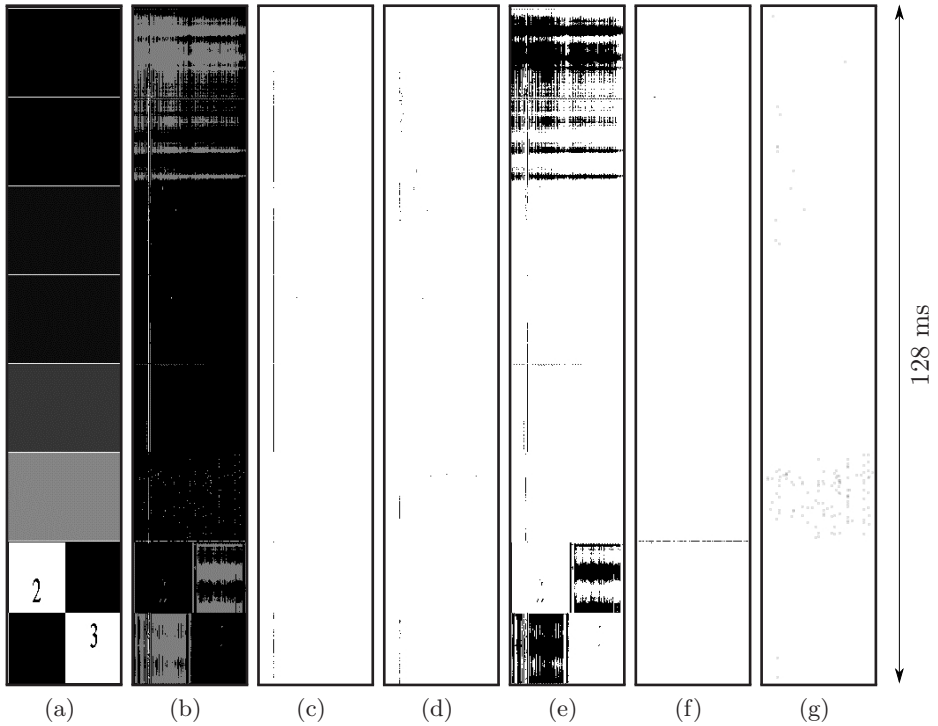


Fig. 3.9. Print pattern and the characteristics decoded from the results by processing a single recorded image: (a) print pattern, (b) composite result from the linescan measurement, (c) missing pixels, (d) fast droplets, (e) slow droplets, (f) ghost droplets, (g) untrustable AOIs.

the nozzleplate where the fluid curtain blocks the light permanently. It is also encountered in the case of very slow droplets, which are exposed multiple times and render a reliable detection impossible.

Eventually, Figure 3.9 (c) can be used to calculate the duration and location of missing droplets, which provides a useful tool for in-flight analysis during waveform development and has the potential to shorten development times.

3.2.5 Summary

The developed linescan technique improves the capabilities of droplet-in-flight systems to perform quantitative assessments of reliability. The technique not only reports the number of missing pixels per time, but provides further information, such as nozzle combinations in the print pattern that are prone to create a certain misfire, time- or pattern-dependent trajectory variations as well as qualitative velocity variations. With the data available from the method, printhead driving signals and the influences from external variations such as temperature or vibrations can quickly be assessed with respect to reliability. This enables a considerable reduction in development time.

Inkjet-Printing and Post-Processing of Metallic Conductors

The additive fabrication of functional deposits from a liquid phase is attractive from the material cost point of view, where a noticeable reduction of material waste can be achieved. This benefit is somewhat counterbalanced by the cost and effort of the formulation of fluids, which will need to accommodate both the functionality and the processability as well as the jetability of the fluid. As the functionality is the driving characteristic, the usage of additives to facilitate the jetability and substrate wetting often needs to be minimized, as any contaminant will need to be removed from the final deposit in order to prevent interference with the performance. Yet another challenge originates from the anticipated printing onto low-cost, non-absorbing polymer substrates. These commonly exhibit inferior surface quality where both substrate wetting as well as the drying behavior need to be controlled by the process or ink additives, such as solvents and surfactants. For thermal processing the low glass transition temperature T_g imposes limitations and finding suitable post-processing techniques is subject to numerous research activities.

After an ink is applied to the substrate, its solvent needs to evaporate and the colloids have to coalesce preferably into a dense solid. A porous network, as it is often observed, shows an increased electric resistance as a result of the contact resistance in a multitude of point contacts, since the resistance is inversely proportional to the neck radius between particles (*cf.* Figure 4.1).¹¹² A second contribution to resistance originates from the limited mean free path of electrons, which are scattered at inclusions and grain boundaries.^{113,114} While many percolation paths are created in the process of annealing or sintering of a printed structure, the formation of large necks and grains as well as minimum pore sizes is essential for good electrical properties. The typically reported value of thirty to sixty percent of bulk conductivity reflects the limited success in forming dense metallic films from inkjet-printed nanoparticle deposits.

4.1 Ink Concepts

Fluids for the generation of printed conductors can be discriminated based on the state of the metal atoms into solution or particle-based inks. The first class

of inks is based on the dissolution of a metal-salt or of metallo-organic complexes in an appropriate solvent. The release of the metal atom for the generation of nanoparticles can be accomplished through various stimuli, such as temperature, radiation as well as chemical reagents.^{115,116} A suitable complexation is often required to improve the solubility of the specific metal compound in the solvent and can also be used to optimize the release of the metal atom at lower temperatures. The challenge for this class often is the solubility limit, which results in relatively low metal loadings in the ink.

Synthesized nanoparticle inks are commercially available with 20 to 60 wt% of metal. Here the challenges lie often with the strong difference in density of the constituents, which favors sedimentation and agglomeration of the particles. Agglomeration is commonly counteracted by electrostatic, steric or electro-steric stabilization. The type of stabilization is dependent on the dispersing media used in the ink.¹¹⁶ In the case of steric stabilization the strength of the attraction between the stabilizing molecule and the particle surface is critical for the onset of sintering. It relates to the energy required to dislocate the stabilizer and bring particles into direct contact. While the desire is to minimize this required energy, a limitation is the stability of the ink, which could undergo destabilization by strong shear flows within ink systems, the printhead chamber or nozzle. The presence of larger polymeric agglomerates can trigger heterocoagulation in the extensional flow of a nozzle with only a small amount of particles present.¹¹⁷

With the ink concepts described above, the release of the metal from the stabilizing, typically polymeric, shell is the key challenge, as their decomposition temperature lies within or above the range of the glass transition temperature of anticipated substrate materials. The concepts for enabling neighboring particles to touch during or after drying include the supply of thermal energy, the use of UV-radiation to initiate chain scission or the utilization of a built-in chemical sintering mechanism.^{118–120} In the latter case the binding moiety at the surface of the nanoparticle is replaced by a halide-ion, which then leads to destabilization of the ink. Grouchko *et al.*¹¹⁸ showed a sharp transition in particle size beyond a specific critical concentration of halide ions. As an increase in the ion concentration is naturally given during drying, this mechanism can be used to trigger *self-sintering* as a result of the evaporation of the dispersing medium.

4.2 Sintering Mechanisms

Sintering is the reduction of the overall system energy without the need for liquefaction by atomic transport mechanisms, which comprise both interfacial and volume diffusion processes (*cf.* Figure 4.1). All of which follow an Arrhenius-type behavior, where the diffusivity of atoms is modulated by the supplied energy as well as the temperature to influence the amount of vacancies and free atoms. The overall sintering performance of particulate materials is among other influences dependent on composition, particle size, sintering time and liquid phase formation.¹²¹

In the low temperature regime as well as initial stage sintering, where the density is lower than 70% of the theoretical density, interfacial transport is dominant. The surface tension, resulting from broken bonds or defects in the parti-

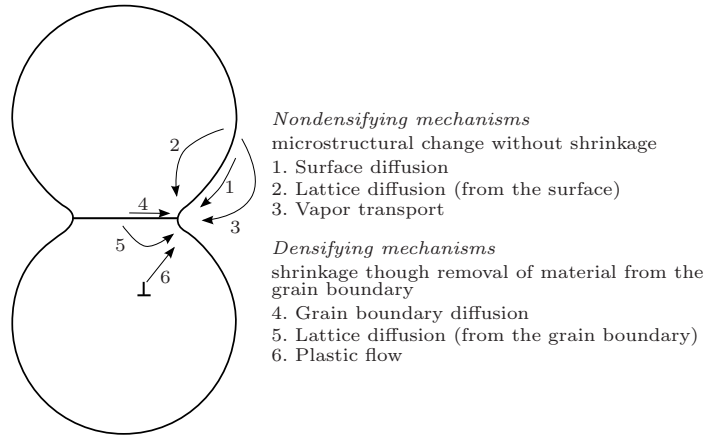


Fig. 4.1. Sintering mechanisms schematically depicted for the simplified case of two touching particles (adapted from¹²¹).

cle surface, in conjunction with the local surface curvature is herein the main thermodynamic driving force. Surface tension provides the activation energy by generating a capillary stress on the surface. As a result atoms will flow from convex (vacancy deficient) to concave (vacancy excess) surfaces to minimize the overall energy. This process will continue until the neck between two adjoined particles reaches an equilibrium, which is determined by the surface energy, the grain boundary energy as well as the dihedral angle. For nanometer-size particles the Gibbs-Thomson equation predicts an exponential increase in the driving force for mass transport on the surface with decreasing particle diameter.¹²¹ In this fashion, surface diffusion can trigger coarsening, i.e. growth of large particles at the expense of small ones. Higher diffusivity as well as enhanced grain growth at lower temperatures is furthermore facilitated by surface melting on nanoparticles,¹²² which promotes processes such as particle rotation, sliding and viscous flow.

An additional driving force is the grain boundary energy, which originates from misaligned lattices of neighboring grains. With an activation energy in between surface and volume diffusion, this process is found in intermediate sintering (70-90% of the theoretical density) and contributes significantly to densification.

Finally, bulk transport requires high activation energies, which occur at considerably higher temperatures and longer sintering times. Here volume diffusion, dislocation climb and plastic as well as viscous flow allow for the atomic motion from the inside toward the surface of the particle or the growing neck region. This results in a net reduction in the distance of the particle centers and, hence, densification. Due to the thermal limitations of the involved substrate materials, these high temperature processes are rarely used in sintering of printed structures.

4.3 Selective Sintering

The thermal integrity of the substrates used for inkjet-printed conductors constitutes a major obstacle for the application of isothermal heating to trigger strong surface diffusion or even late stage sintering. Many reports in the literature therefore focus on the development of alternatives to equilibrium thermal annealing, where the thermal energy is selectively supplied to the deposit. The approaches taken include plasma^{123–126}, chemical,^{118–120} microwave and electrical,^{127–131} UV or UV-assisted,¹³² IR,^{49,133} laser,^{134–137} as well as intense pulsed light processing.^{131,135,138–145} A good overview on most of the techniques and their performance are presented in recent literature.^{47,146–148}

Many of the approaches use electromagnetic radiation to selectively couple energy into the printed structures. We therefore summarize the interaction and limitations shortly below.

The wave interaction with matter is characterized by both, the frequency-dependent dielectric permittivity ε and magnetic permeability μ as described by Maxwell's equations.¹⁴⁹ The energy density w released in a material is then proportional to the squared magnitudes of the field components and can be described by¹⁵⁰

$$w = \frac{\omega}{2} (\varepsilon_0 \Im \{\varepsilon_r\} \mathbf{E}^2 + \mu_0 \Im \{\mu_r\} \mathbf{H}^2) \quad (4.1)$$

where ω is the angular frequency, \Im the imaginary part, \mathbf{E} the electric field and \mathbf{H} the magnetic field vector. The subscripts 0 and r denote the free space and the frequency-dependent relative material properties, respectively. The heating efficiency is dependent on the position of the sample with respect to its main loss mechanism and the magnitude of the respective field component. The equation furthermore allows for the description of the phenomena in DC current situations, where $\Im \{\varepsilon_r\}$ reduces to σ and describes the effects of Joule heating.

The interaction with the particulate or multi-phase materials is highly complex, as material properties as well as length scales change due to diffusion processes as well as evaporation of volatile components. Significant interaction with a material is only given when the size of the materials exceeds the order of the skin-depth δ given by $\sqrt{2/(\omega\sigma\mu)}$. Hence considerable interaction with microwaves can be expected for particles of 1 μm in size, while for the visible spectrum this reduces to 2–3 nm. For nanoparticles the main effect is found to be the excitation of a surface plasmon resonance, which is dependent on shape, dimension as well as optical properties of the particle. The size-dependent change of the absorption spectra can then result in an overlap with the absorption spectra of other materials in the stack and trigger thermal runaway.¹⁵¹ In the case of a process tailored to a specific spectral band the energy coupling may reduce significantly and result in insufficient sintering.¹⁵²

4.4 Influence of Drying

In inkjet printing the amount of functional material typically must be kept lower than 10 vol%. Reasons are to prevent an increase in viscosity and to omit strong

damping inside the printhead or jamming inside the nozzle. Hence, more than 90 vol% of solvent has to be vaporized from the substrate before final sintering can be initiated. This drying step can be time limiting as evaporation from the non-porous substrate may be constrained by the glass transition temperature of the substrate before permanent deformation occurs. Another reason for working at reduced temperatures is to prevent explosive evaporation of the solvent.

The presence of the surrounding liquid often impedes the formation of well-defined structures as a result of instabilities originating from the surface tension of the liquid in combination with the constricted pattern of the deposited droplets. Soltman *et al.* studied the influence of surface tension and droplet spacing and provided a model for the pre-flight examination of print patterns to omit instabilities based on the bulk physical properties of an ink.^{48,153,154}

The evaporation dynamics strongly influence the deposition of the solute and complicate the realization of the final functionality on non-absorbing substrates. As an example the differential evaporation rate due to the varying radius of curvature of the liquid surface can trigger a preferential deposition of material either on a pinned contact line (coffee stain) or in the center.^{155–157} Counteracting measures can be taken in ink formulation using binary mixtures of solvents¹⁵⁶ or the addition of fluorosurfactants.¹⁵⁸ Marangoni flow due to the developing tension gradient at the surface is initiated to counteract the concentration gradient-driven outward flow of the solute. Different results may be generated by an unpinned contact line, where the sequential evaporation of ink constituents can result in the contraction of a printed line and the generation of high aspect ratio functional deposits with a minimal footprint.¹⁵⁹

The drying step is also critical with respect to sintering, as the formation of agglomerates dictates achievable densities. The coordination number of a pore, defined by the number of particles it is surrounded by, alongside with the dihedral angle defines whether a pore will shrink or grow during the process of sintering.¹⁶⁰ In nanoparticle systems typical coordination numbers are larger than the critical value and densification is prevented. To progress grain growth the system needs to overcome the established equilibrium through additional energy, which may limit the pace of the process.¹²¹

4.5 Technologies for Continuous Post-Processing of Metal Inks

The limited time available for drying and sintering poses considerable limitations to the speed of a R2R process. Many techniques have been proposed and optimized for drying in the graphic arts industry. The products in this industry vary greatly from the generation of conductive or functional features, but employ similar techniques for the reduction in viscosity to enable penetration into the substrate, surface oxidation or solvent evaporation. This is facilitated by different technologies such as vertical blast, suspension, IR or excimer dryers.⁶¹

Typical IR drying systems employ the near infra-red (NIR) part of the spectrum (800 nm to 2 μ m), as these interact greatly with the inks found in the graphics arts and possess a high efficiency.⁶¹ The molecular vibrations excited in the

often polymeric substrates can mainly be found beyond $2\text{ }\mu\text{m}$, while inks exhibit a much broader absorption spectrum with a maximum in the visible part and significant absorption in the NIR band.¹³³

Photonic curing or intense pulsed light (IPL) processing is a method originating from *rapid thermal annealing*, where high-intensity lamps are utilized to rapidly increase the temperature on a substrate. The plasma arc lamps used produce radiation across the UV, visible and NIR part of the spectrum. This broadband characteristic makes them applicable to a wide range of materials, while it is limiting in terms of selectivity, which leads to partial absorption of the radiation by the polymeric substrate. The thermal flux from the highly absorbing ink must be controlled by short pulse durations to steer the temperature development. With the increase in repetition frequency and reliability, scalable radiation sources are now available with approximately 50% quantum efficiency and a wall-plug efficiency of 30%.¹⁶¹

It was attempted to benchmark IR drying and photonic curing against convective oven sintering for their applicability to R2R sintering. Figure 4.2 gives an overview of the achievable resistances with a commercial silver nanoparticle ink (EMD5603, Sunjet, UK) on polycarbonate substrates with a glass transition temperature of $145\text{ }^{\circ}\text{C}$ as a representative specimen of the polymeric materials.

Convective oven sintering showed deviant results, which could be mainly attributed to difficult line formation on the chosen substrate and the dynamics of the ink on the substrate during slow heating and the resulting instabilities. The two layer–four pixel combination was selected as the reference value with a mean resistance of $9.3\text{ }\Omega\text{ cm}^{-1}$ and a standard deviation of $0.7\text{ }\Omega\text{ cm}^{-1}$.

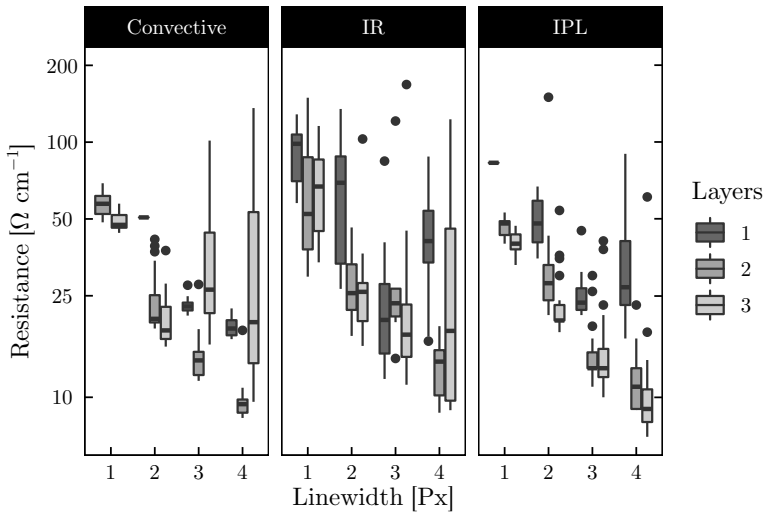


Fig. 4.2. Resulting resistance as function of line width and layer count for three different sintering methods: (1) convective oven sintering [Binder US, $130\text{ }^{\circ}\text{C}$, 30 minutes], (2) R2R IR sintering [HQE 500, Ceramicx, IRE, working distance 15 mm , 5 m min^{-1}] and (3) IPL processing [Pulseforge 3100, Novacentrix, US, 10 m min^{-1}] – all specimen printed with Xaar126-50 pL with $70.5\text{ }\mu\text{m}$ resolution on Makrofol (Bayer, DE).

IR irradiation of the printed samples showed strong scatter in the data compared to oven sintering. Clear evidence of substrate deformation around the ink deposits was visible, which related to the stronger absorption by the ink and the heat conduction into the substrate. The deformation and mismatch of the coefficients of thermal expansion (CTE) furthermore favored partial delamination and cracking of the deposits. The lowest achievable resistance was found for a combination of three layers and four pixel wide lines with $12.8 \Omega \text{ cm}^{-1}$ and a standard deviation of $3.8 \Omega \text{ cm}^{-1}$. The reliability of the process, however, does not support this as a viable option for a R2R process. Other authors have shown positive results using IR on paper or heat-stabilized PEN.^{49,133}

IPL processing was carried out with an empirically optimized pulse on predried deposits. It was found that the process gave consistent results with the expected reduction in resistance values with increasing layer count. The number of discontinuous tracks was comparable to the values seen with thermal sintering and can be attributed to the pattern formation on the substrate rather than the sintering process. The optimal value was found with four pixel wide lines and three deposited layers to yield $9.2 \Omega \text{ cm}^{-1}$ with a standard deviation of $1.6 \Omega \text{ cm}^{-1}$.

The results indicated that IPL processing offered a viable alternative to oven sintering with resistances in the order of $10 \Omega \text{ cm}^{-1}$ with a minimal susceptibility to the deposited volume. An increased variability of resistance was found, which related to the change of conformation of the conductor during rapid heating and requires further investigation. With respect to process speeds photonic curing does offer the potential to reduce the required timescale from 30 minutes to a few seconds, which enables realistic and compact machine designs for R2R printing of conductors.

In the following sections only IPL processing will be considered as one of the most promising high-speed annealing approaches for metal nanoparticles.

4.5.1 Influence of the Spectral Characteristics of the Underlying Layer

The characteristics of the material stack underneath the deposit has a significant effect. It affects the thermal boundary to the freshly printed layer, while its reflection and absorption characteristics influence the amount and spectral composition of the reflected light.^{162–164}

The dynamics of the sintering process were recorded with a two-point probe measurement setup during processing, where gold electrodes were sputtered onto polyimide substrates with a defined spacing of 20 mm. Silver ink traces were added subsequently as a triple-pass print with a nominal width of four pixels to ensure consistency. The resistance values were recorded concurrently with the current metric of the IPL equipment (Sinteron2000, Xenon Corp., US) to allow for synchronization of the measurement data.

The graphs in Figure 4.3 depict the results of the conducted experiments with varying absorption characteristics of the substrate holder surface to study the influence of the composition of the reflected light. To exclude any thermal runaway effects, the experiments were conducted at low pulsing frequencies of 1.9 Hz. Conductive features were observed with all spectral compositions but

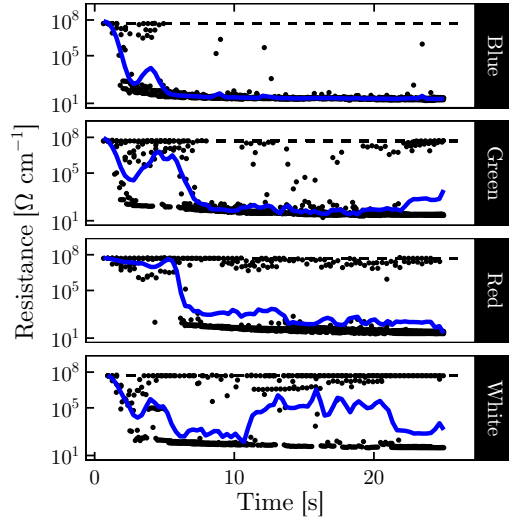


Fig. 4.3. Influence of spectral characteristics of the substrate holder on the resistance evolution during wet sintering [circular reflector, distance to housing 20 mm, flash energy 350 J, pulse width 580 μ s, repetition rate 1.9 Hz, acquisition frequency 3.2 Hz, 5 samples per spectrum, local polynomial regression fit (blue)]

values were found to vary significantly depending on the absorption spectra. The temporal development started with an open circuit,* which developed into a conductor in the course of the first five seconds. The observed rate of the reduction was found to be highly dependent on the absorber used in the experiment. During continued illumination of the sample strong variations in resistance could be seen, where an abrupt change from closed to open circuits was observed.

The behavior is strongly linked to the absorption spectra of the silver nanoparticles, which for a diameter below 50 nm typically exhibit a plasmonic absorption peak in the wavelength range below 450 nm. The particles interact with the incident electromagnetic wave and convert the energy into heat. Consequently, solvent is evaporated and the stabilizing agents start to detach from the nanoparticle surface. When the surfaces of two neighboring particles meet, surface diffusion and necking is triggered by the point pressure of the contact and the surface energy.¹⁶⁵ This surface diffusion can also trigger coarsening, where the growth of larger particles is promoted at the expense of smaller particulates. This growth increases the heat generation as a result of the redshift of the absorption spectrum and the increase in the absorption cross-section of larger particles.¹⁶⁶

The well-matched absorption of the particles to the spectrum of the blue reflector in Figure 4.3 resulted in the optimal conversion of particles into a conductive layer in less than two seconds or approximately four pulses. The particle growth and the rapid coarsening as a result of neck growth in conjunction with the removal of the green and red portion of the spectrum at the blue reflector

* The open circuit is defined as the maximum resistance value resolved by the multi-meter, which is $10^8 \Omega$ over 20 mm in the presented case.

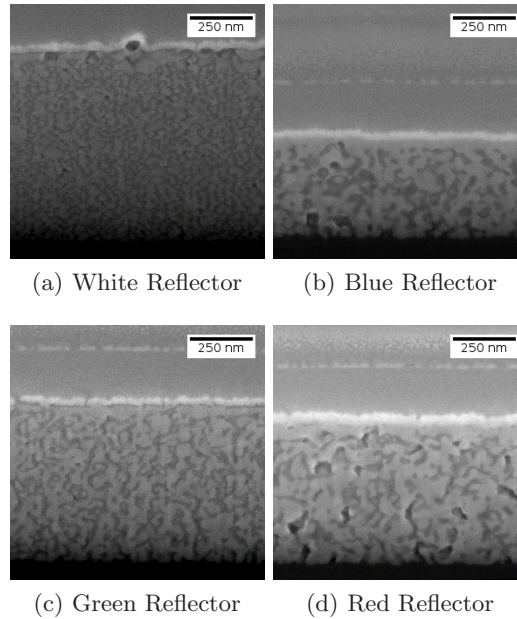


Fig. 4.4. Resulting micro structure after processing deposits on substrate holders with different spectral characteristics [circular lamp reflector, distance to housing 20 mm, pulse width 580 μ s, repetition rate 1.9 Hz].

resulted in a self-damping of the sintering process and hence kept the sintered layer intact.

When using a red reflector the initial drop-off was delayed by approximately five seconds, as the strong absorption from the blue spectral band was absent. The heating effect most likely resulted from the absorption of the incident light at the substrate until metal particle clusters grew large enough to absorb the energy in the red part of the spectrum, which resulted in thermal runaway.

An intermediate spectral irradiation was achieved by a green reflector and exhibited fast initial reduction in resistance but showed unsteady results at a later stage in the process. The initial drop in resistance resulted from the strong absorption close to the absorption peak of the particles. With increasing size of the particles thermal runaway occurred as layers became more susceptible at longer wavelengths.

Reflecting all the incident electromagnetic energy using a white reflector revealed a combination of the blue and the red reflector characteristics. The fast initial drop in resistance resulted from the strong absorption of the blue part of the spectrum. At later stages in the process thermal runaway and unsteady resistance could be observed. The excessive heating due to the particle growth may hence have damaged the substrate or disintegrated the conductor by cracking due to the unmatched coefficients of thermal expansion.^{167,168}

Figure 4.4 depicts the resulting microstructures, which were exposed by depositing a platinum layer on top of the specimen and cut with a focused ion

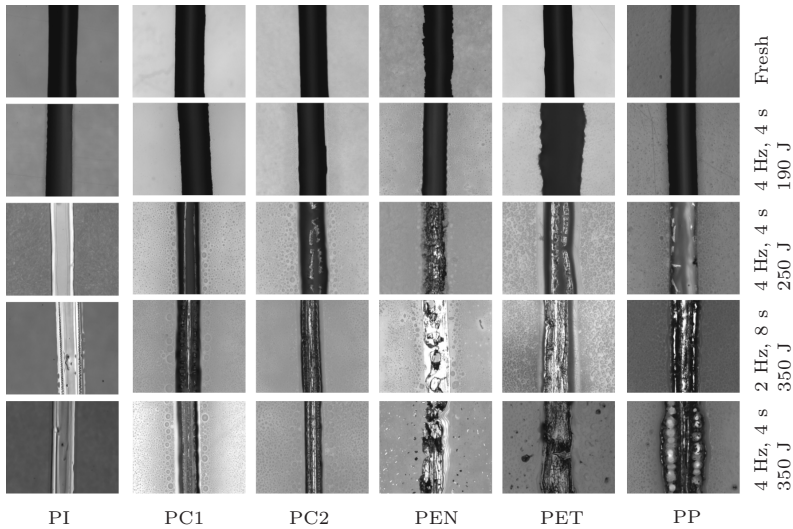


Fig. 4.5. Four pixel wide silver lines on different substrate materials processed with various combinations of pulse energies and repetition frequencies [circular reflector, distance to housing 20 mm].

beam. The clear difference between the formed structures with the differently colored reflectors corroborated the observed differences in electrical conductivity. An interesting effect, which is highlighted in these images, was the role of the green part of the spectrum, which appeared to have a significant influence on the microstructure of the sintered deposits. With the inclusion of the green portion of the spectrum, coarsening appeared to be inhibited as seen in (a) and (c) by the fine granular structure. Using mainly the blue or red part of the spectrum exhibited an efficient densification of the deposit resulting in a denser structure. Hence, a competing effect, which is triggered by the green spectral band, prevents the strong diffusion of atoms into a dense structure.

4.5.2 Substrate-Dependent Line Formation

Not only the microstructure of the sintered material was found to be dependent on the spectral composition of the effective radiation but also the macroscopic structure of the traces. The difference in heating rates altered both the lateral contraction of the line as well as evaporation of the solvent. Figure 4.5 depicts the resulting line conformation for substrate materials with different absorption characteristics and for different processing conditions. Line conformation worsened with increasing pulse power and repetition frequency for poly(ethylene-2,6-naphthalate) (PEN), poly(ethylene terephthalate) (PET), as well as polypropylene (PP), showing disrupted tracks and strong coffee-ring effects at the maximum settings. Stable results were observed for polyimide (PI) and polycarbonate materials (PC1&2), where polycarbonate showed the strongest line confinement of all materials.

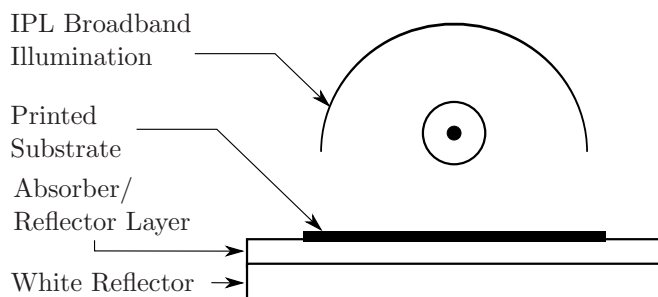


Fig. 4.6. Schematic representation of the passive optimization of the sintering process by placing an absorber layer underneath the printed substrate.

Apparent was also the clear presence of a sweating effect on all materials except polyimide. It was concluded that the fluid surrounding the traces originated from evaporated and recondensed solvent. Polyimide appeared to have been heated considerably by the incident radiation to prevent recondensation of the solvent.

4.5.3 Passive Optimization

From the findings described in the previous sections we deduced that placing a suitable absorber/reflector material underneath the substrate (*cf.* Figure 4.6) would enable consistent sintering. This could be applied to substrates such as PET, where the printed material was expected not to sinter at high repetition rates with good line conformation. Polyimide was chosen as an absorber of the blue part of the spectrum, thus being a red reflector, while its indirect heating would prevent line distortion and sweating.

Figure 4.7 summarizes the results. (a) shows freshly printed ink and the result of sintering with a white reflector, (b) largely reflects the characteristics discussed in Section 4.5.2 with no or absent electrical conductivity. (c)-(f) show the impact of adding layers of 25 μm thick polyimide sheets underneath the PET foil. As layers of absorber were added, line conformation improved drastically, sweating was suppressed and steady conduction paths were found by adding a total of 100 μm of polyimide in Figure 4.7 (f).

Highly conductive deposits were further generated on arbitrary substrates, while maintaining the highest possible repetition rate and energy. This simple passive adaptation with suitable reflectors underneath the substrate enabled a significant speed-up accompanied by an improvement in quality.

4.5.4 Active Optimization

In the previous section, the passive control of the energy flow into the deposited ink as well as the substrate stack was described. This approach is favorable as to generically optimize the performance for a given material-sinter system combination. On the other hand the build of IPL curing systems advanced to accommodate the variation of pulse length and intensity with a temporal resolution of 30 μs .¹⁶¹ This was necessary for the optimization with respect to process

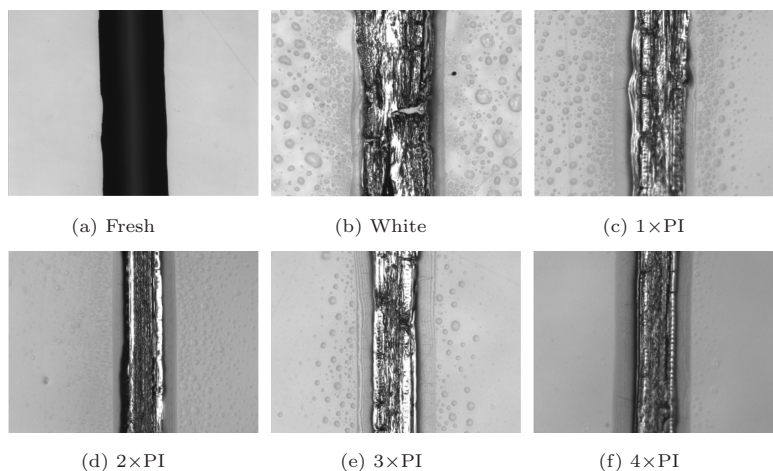


Fig. 4.7. Optimization of the overall sintering process for a thermally sensitive PET substrate with added layers of polyimide as absorber [4 px wide silver lines, flash energy 350 J, pulse width 0.58 ms, repetition rate 4 Hz, sintering duration 6 s].

speeds as well as temperature limitations of the thermally sensitive polymeric substrates used. Intermediate drying or the application of porous or particle-coated substrates to quickly remove the liquid from the printed deposit^{169,170} remained necessary to suppress superheating of the solvent at heating rates of 30–40 K ms^{−1}.¹⁷¹

By tailoring the pulse energy for the selective heating of the ink deposit, one can also adapt the pulse train to facilitate the slow evaporation of the solvent before sintering the remaining solid contents. The challenge here lies in the trade-off between optimal sintering and the movement of the substrate during the process, which may illuminate undried ink. An example of such a pulse train is presented in Figure 4.8. The intensity of the pulses is modulated to create two different sections in the temperature ramp. First a low energy drying segment, where the simulated surface temperature rises to approximately 300 °C to drive off the solvent and dry the deposit. In a second high energy section the used copper oxide is converted to elemental copper. The substrate temperature remains below 100 °C. The presented temperatures serve as an indication of the actual values, as only indicative material properties were available and the transient changes due to phase transition as well as densification are not considered in the simulation.

To study and optimize the applicability of the pulse modulation depicted in Figure 4.8, a commercial copper oxide ink (Metalon[®] ICI-002HV, Novacentrix, US), loaded with 16 wt% of 130–140 nm sized nanoparticles was printed with a Xaar 1001GS6 printhead (Xaar, UK). Processing was performed on a proprietary print rig (Propheteer, US), where optional pre-drying could be performed using an IR dryer (6 kW, DRI, US) with a length of 50 cm. IPL curing and drying was performed using a PulseForge[®] 3200X2 (Novacentrix, US) on a coated PET (Novele[™], Novacentrix, US).

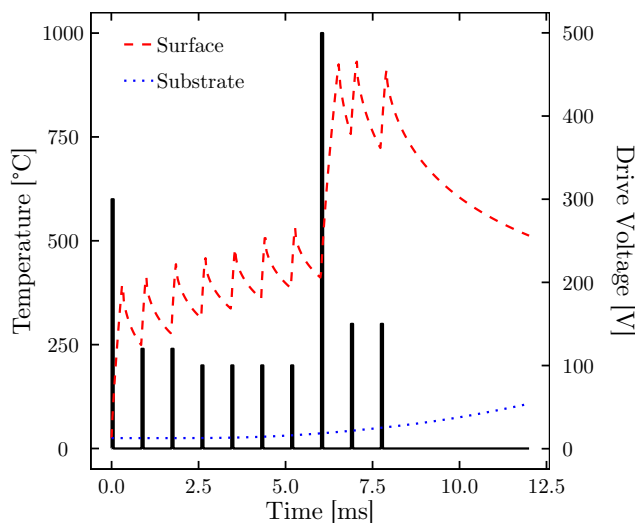


Fig. 4.8. Comparison of the temperature evolution on the top surface of the deposit (red, dashed) and the backside of the substrate (blue, dotted) with a train of pulses (black, solid) created by an arc lamp [simulated with SimPulse v3.40, Novacentrix, US, material stack: CuO, Novele™ top coat, Novele™ substrate].

Figure 4.9 shows the resulting resistance as function of substrate velocity for four pixel wide lines. At low velocities the minimum possible IR drying setting appeared sufficient to evaporate an adequate amount of solvent and the produced lines showed no signs of local disintegration or blow-off, which would be characteristic for the exposure of wet deposits to the high-power Xenon illumination. As line speeds increased higher IR power levels were required to drive off the solvent and produce consistent results with the uniform light pulses. At the maximum substrate velocity 100% of the drying power proved insufficient, leading to strong scatter in the data with an increased mean resistance. The arbitrary pulse as presented in Figure 4.8 produced lines of nearly constant and consistent resistance of approximately $12 \Omega \text{ cm}^{-1}$ at speeds higher than 0.09 m s^{-1} without the need for pre-drying. A noteworthy anomaly is the higher resistance at low velocities, which could relate to reduced heating of the chuck supporting the substrate underneath the sintering lamp. With increasing substrate speeds the nominal flux of thermal energy into the water-cooled chuck increased and might have enhanced the sintering performance due to the altered thermal boundary condition for the heat transport at the bottom side of the substrate.^{161,164}

4.6 Residues and Entrapped Gases

Depending on the utilized temperatures and microstructure generated during the sintering step, additives or solvents can be trapped by the capillary pressure inside the network of pores. These residues may over time alter the performance

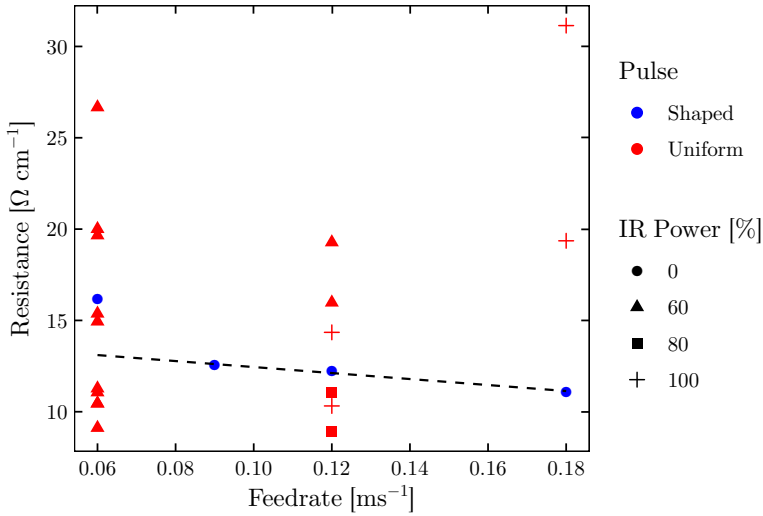


Fig. 4.9. Average resistance of the inline printed, dried and sintered structures as a function of IR drying power, pulse shape and set line speed for a four pixel wide copper oxide line. The dashed line represents a linear fit of the results with the arbitrary pulse depicted in Figure 4.8 [360×540 DPI, ICI-002HV on Novele™ substrate].

of the sintered structure due to aging effects or outgas during operation and contaminate the application environment.

To investigate the influence of the sintering temperature on the amount of trapped residues, thermally sintered samples of silver nanoparticle ink were analyzed with respect to their outgassing characteristics. Polyimide samples of 2×2 cm² in size were coated with a printed triple layer of silver ink and sintered at 100 °C and 200 °C for thirty minutes. The samples were subsequently heated again to temperatures between 100 °C and 200 °C, this time in a vacuum environment of 2×10⁻⁶ Torr. The escaping constituents were then analyzed using a high sensitivity quadrupole mass spectrometer. Figure 4.10 shows the difference between the coated and the blank polyimide sample.

The comparative study of coated and uncoated polyimide samples showed that mainly nitrogen was released from both types of samples, suggesting that this was trapped in the polymer film rather than the deposit. This was further corroborated by the reduced value, when part of the polyimide surface was coated with sintered silver ink, which prevented part of the outgassing from the substrate. The source of the contamination was most likely air, as could be deduced from the ratio of argon to nitrogen.

Outgassing of carbon compounds was found to be influenced by the temperature applied during sintering. Specifically for the sample treated at 100 °C strong outflow of carbon dioxide and methane was observed, which originated from trapped organic solvents or additives in the ink that was obviously not fully cured. By monitoring the resistance of the conductive layer it was found that the sample underwent sintering in the analysis step, which relates those measurements to the evaporative drive-off of the solvents and capping molecules. The

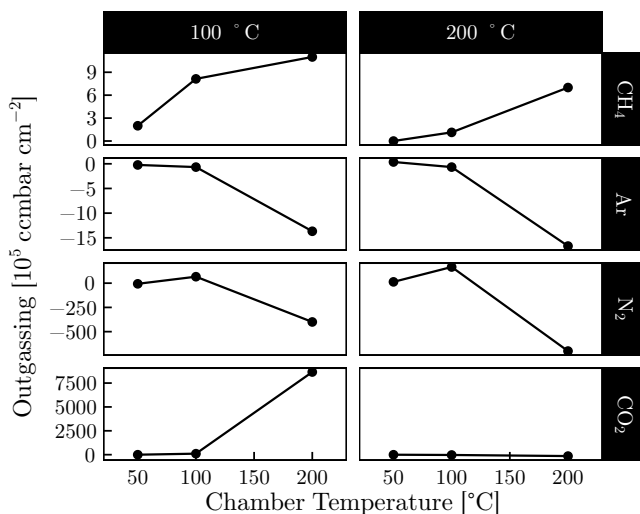


Fig. 4.10. Amounts of extracted gases compared between silver-coated and uncoated polyimide samples subjected to different sintering temperatures.

samples sintered at 200 °C, showed no noticeable difference to the gas flow from the substrate. The resistance value of these samples remained unchanged.

4.7 Summary

The conducted investigations showed that the combined drying and sintering process of metallic inks from freshly inkjet-printed, wet deposits was possible when the dynamics of the process were well controlled. Two different approaches were developed to demonstrate such a control.

A passive mechanism for the control of the energy reflected from the backside of the substrate was implemented using a tailored absorber, which provided good attenuation of the resonating radiation between the reflector of the sintering lamp and the substrate holder. In this fashion the blue spectrum was attenuated in the reflected radiation in order to prevent thermal runaway. A portion of the red spectrum was retained to provide additional heating of the substrate to ensure consistent contraction of the lines and prevent recondensation of solvent in the vicinity of the track.

In a second step an active time control of the pulse energy was attempted using arbitrary pulse shaping of high-energy pulses from an arc lamp. It was shown that wet deposits could be dried and sintered at a substrate velocity of 0.18 m s^{-1} using a segmented pulse train to ensure consecutive drying and reduction of copper oxide nanoparticles to elemental copper. Attempts to reproduce these results with a combination of IR drying followed by the application of uniform pulses showed inferior electrical performance and inconsistent sintering. The combination of IR and photonic sintering was unable to provide a solution for the highest substrate velocities of 0.18 m s^{-1} .

The residual organics and trapped gasses were analyzed to give an indication of both long term reliability as well as the potential for the application in low-pressure environments. Sufficient sintering, with a minimal amount of residues that contain carbon were found when conducting sintering at a temperature of 200 °C for 30 minutes. Treatment at only 100 °C revealed incomplete sintering and a strong increase in the release of carbon-based compounds such as CO₂. Air-borne argon and nitrogen remnants were found to be trapped in the substrate rather than in the printed structure. Some of the remnants such as argon and methane are challenging for certain vacuum systems, such as getter pumps, and would need to be removed with a separate system. The analysis did not indicate any technical issue that would prevent the combination of this particular ink and process being applied in low-pressure environments.

Applications

In applications such as graphical or industrial printing, inkjet is the key component. In other applications inkjet plays an ancillary role, where the dosing capability and positioning accuracy are utilized to optimize the overall performance of a process or add functionality.

In the following sections we explore three different applications, where inkjet and the post-processing techniques developed in this thesis are used in hybrid processes to reliably achieve high resolution and high-throughput as well as functionalities on non-flat surfaces.

5.1 Hybrid Approaches to High-Resolution Structure Generation

Nanoimprint lithography (NIL) is a $1\times$ lithography technique, where a nano-structured silica-glass stamp is pressed into a resist film to form a resist pattern. Depending on the process used for the fixation of the pattern in the resist, thermal and UV imprint lithography are discriminated. As a result of the high resolution of a few nano- to micrometers the applications range from memory and logic to optical as well as biomedical devices.^{172,173}

A simplified process diagram for the UV-based imprint process discussed here is shown in Figure 5.1. After initial alignment and the application of a hard mask layer onto a silicon wafer, a droplet pattern of low viscosity resist is dispensed in the desired area on the wafer. This fluid layer is matched to the feature density in the imprint stamp to enable swift and defect-free filling of the relief channels in the stamp. After the stamp is forced into the resist layer the fluid will flow out from underneath the elevated surfaces and fill the channels in the stamp. The capillary force is counterbalanced by the viscous forces resulting from the decreasing fluid film thickness, which results in a residual layer of finite thickness (*cf.* Figure 5.1). The imprinted resist layer is subsequently cross-linked using UV radiation and the stamp separated from the wafer. Thereafter the residual layer is removed in an ashing process and the hard mask layer is patterned using a CF_4/O_2 plasma.

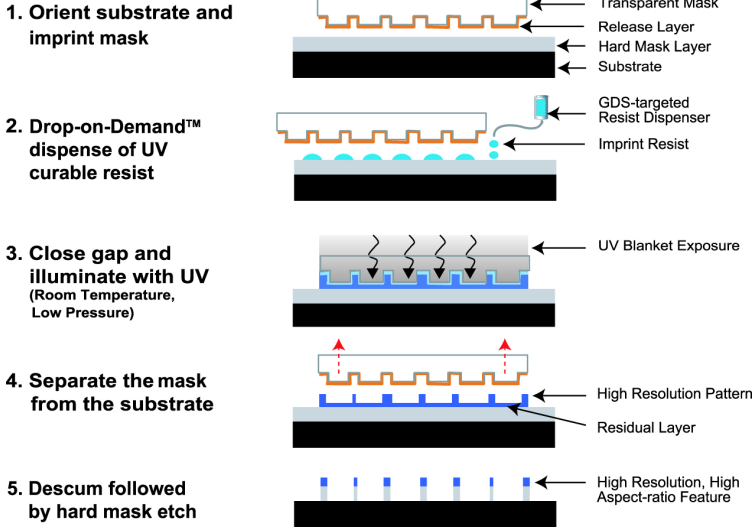


Fig. 5.1. Simplified process flow for resist patterning using Jet and Flash™ Imprint Lithography (JFIL) (Reprinted with permission of IS&T: The Society for Imaging Science and Technology sole copyright owners of *NIP30: International Conference on Digital Printing Technologies and Digital Fabrication 2014 Technical Program, Abstracts, and USB Proceedings*).

From the given overview it is evident that the residual layer is one of the key challenges, as its thickness variations have a strong impact on underetch in the isotropic CF_4/O_2 ashing process and therefore the critical dimension of the process. The spread time t_{spread} to reach a certain residual layer thickness (RLT) can be related to the viscosity η , surface tension γ and the droplet spacing Δ_s by¹⁷⁴

$$t_{\text{spread}} \propto \frac{\eta \Delta_s^2}{\gamma \text{RLT}} \quad (5.1)$$

From Equation 5.1 one can deduce that minimizing the viscosity and droplet spacing results in an appreciable reduction of the squeeze time, while the residual layer thickness cannot become zero. As the RLT is dictated by the required critical dimension of the process and viscosity as well as surface tension are linked to the performance of the resist material, only droplet spacing is left as a free parameter. Evaporation-induced viscosity changes within the deposited drop patterns are of concern as this can result in varying RLTs. Evaporation will be most pronounced at the circumference of the droplet pattern due to unsaturated gas mixture but viscosity gradients may be appreciable within the pattern at reduced jetting frequencies and low substrate velocities.

A secondary process is the diffusion of the entrapped air. Air can diffuse into the resist, the template or the hard mask layer. The presence of air in the resist is disadvantageous due to oxygen inhibition of the cross-linking reaction and changes in etching performance. Hence, diffusion through the template or the transfer layer is preferred and exhibits a dependency on (RLT^2) .¹⁷⁴

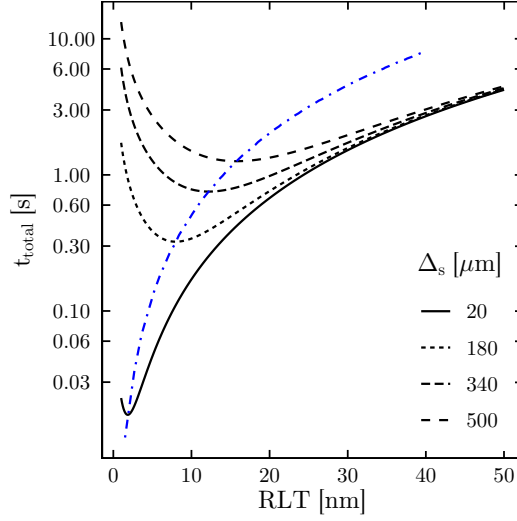


Fig. 5.2. Estimated total squeeze time t_{total} as function of the residual layer thickness (RLT) for different drop spacing Δ_s with a blank template. The total time is estimated using the summation of the visco-capillary spreading time and the diffusion time as computed from the diffusion into the template. The line (— · —, blue) highlights the development of the minimum time to fill with increasing drop spacing [viscous, capillary and diffusion contributions fitted from Wuister *et al.*,¹⁷⁴ Figure 2].

The combination of the viscous-capillary spreading and dissolution times results in an optimal total squeeze time t_{total} , which depends on the chosen droplet spacing and residual layer thickness as depicted in Figure 5.2. The overall time comprising spreading and diffusion of the entrapped air reduces with decreasing droplet spacing due to the reduction of area available for trapping gas. The increase of the droplet density on the wafer, however, requires a decrease in droplet volume. This aids to reduce the initial layer thickness as well as lateral outflow of fluid from underneath the stamp, which is critical in step-and-repeat lithography used for larger wafer sizes.

The complexity of the actual process relies on many more factors, which relate to both throughput as well as defectivity. These factors include the imprint time and pressure, the velocity of the stamp as well as the influence of meniscus pinning at the edge of features on the fill time.

To obtain a reduced droplet volume from a given printhead geometry, the traveling wave principle can be employed to tailor the time-dependent pressure behind the nozzle inlet. The dissipated heat from an increased number of pulses increases the ink temperature locally but is counterbalanced by a strong convective flow of ink through the Xaar-type actuator. Even slight temperature variations narrow the operational window of the process as can be seen in Figure 5.3 (a) for a specialized waveform on a Xaar1001 printhead. When increasing the temperature above the nominal value of 20 °C a strong increase in volume was observed. Here a reduction in the viscous dissipation changes the pressure amplitude and unbalances the forces during droplet formation. Thermal control of the printhead and

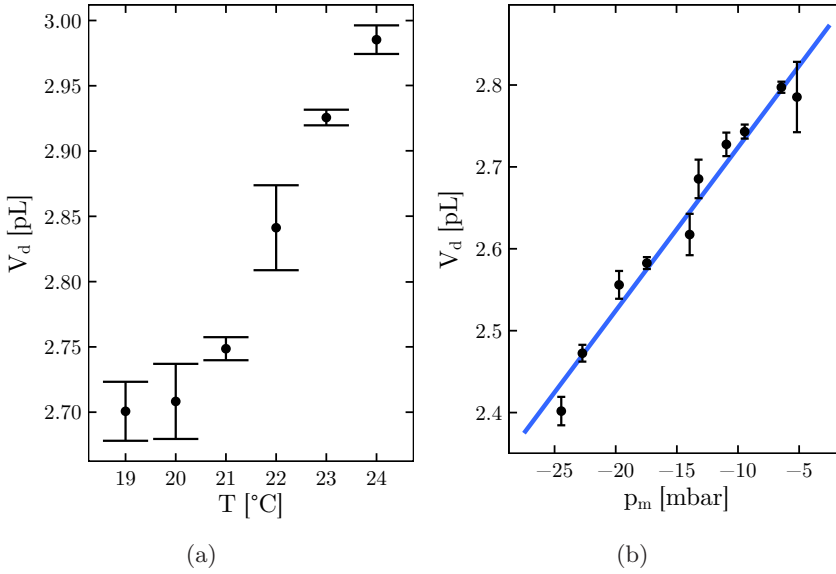


Fig. 5.3. Influence of (a) the fluid temperature T and (b) the applied meniscus pressure p_m on the resulting droplet volume V_d [Xaar 1001, 11.6 kHz jetting frequency, gravimetric analysis].

resist have a two-fold function in the process, as convective removal of heat from the printhead ensures minimal thermal drift as well as consistent RLT values.

The meniscus pressure and consequently the filling of the nozzle are crucial for the acceleration of the fluid from the orifice. The mean meniscus position located further inside the nozzle allows for the reduced mass of ink to be accelerated much quicker and results in higher droplet velocities.⁸³ The ejected droplet can therefore be expelled at a high velocity and lower volume, if the mean meniscus position is further retracted as shown in Figure 5.3 (b). For the used printhead design -25 mbar was the lower limit of the meniscus pressure before air ingestion was observed.

To enable a further volume reduction, limitations originating from the chosen printhead design needed to be overcome. Xaar 1002 AMp exhibits stronger damping and allows for a simplification of the waveform shape. With the improved design the thermal impact on the system at high ejection frequencies was reduced and higher meniscus pressures could be facilitated.

Figure 5.4 shows the droplet volume as a function of jetting frequency. The simplified waveform approach yielded a consistent characteristic with only a slight upwards trend of 10 fL kHz^{-1} , which hints at some residual oscillation in the channel. The average is found to be 2.1 pL with a 3σ of 0.3 pL. The volume could be adjusted to the required volume for a specific pattern by altering the voltage applied to the printhead actuator. The approaches to volume reduction described above can further be applied to the optimized printhead design.

Applying the reduced droplet volumes in the JFIL process yielded results as depicted in Figure 5.5. Here two different droplet volumes, 0.9 pL and 1.5 pL, were

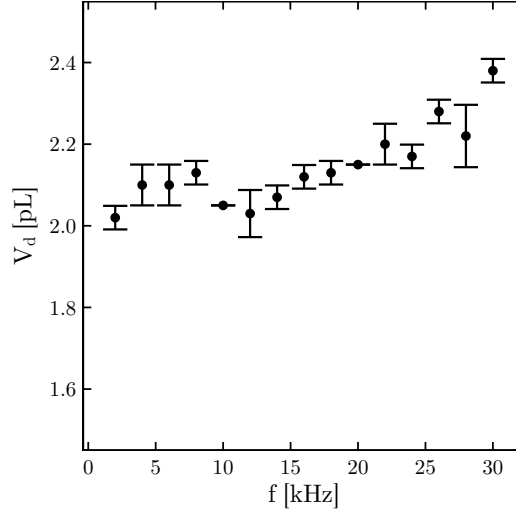


Fig. 5.4. Frequency response of the droplet volume V_d with simplified waveform approach a Xaar 1002 AMp printhead. [Resist temperature 23 °C, 100% duty pattern, gravimetric analysis].

compared with respect to non-fill defectivity and squeeze time for 28 nm Flash-like device gate patterns. The drop pattern density was adjusted to the target RLT of 15 nm for the specific stamp in use. The improvement of spread time by 500 ms with decreasing droplet volume at a constant non-fill defectivity level was apparent. Other experimental conditions (depicted in light-gray) converged to the desired low defectivity values at a holding time of 2.5 s, which is prohibitive for the throughput target of the process. Further optimization related to wetting performance of the droplet on the hard mask layer could reduce the spreading time to 1 s at a defectivity level as low as 0.1 cm^{-2} .¹⁷⁵ The use of the lower drop volumes furthermore enhances the versatility of droplet patterns, where small volume variations can be created in a small spatial envelope. This can be beneficial in partial fields close to the edge of the wafer.

Summary

The combination of the optimized printhead design for high-frequency generation of small droplets and suitable driving waveforms allowed the generation of sub-2 pL droplets at frequencies up to 30 kHz. This translates into achievable substrate velocities of 2.1 m s^{-1} and 1.05 m s^{-1} for 360 DPI and 720 DPI, respectively. The application of the small droplets in a JFIL process proved the assumption of faster and more optimal filling of nanometer sized structures. Here the RLT target was 15 nm with the previously reported variations of 3σ of 1.4 nm on a $22 \times 33 \text{ mm}^2$ imprint field.¹⁷⁵ An improvement in the required squeeze time of 20% at a constant non-fill defectivity level for 28 nm Flash-like device gate patterns was achieved using lower droplet volumes. Wafer sizes up to 300 mm were successfully patterned in full and partial areas with low defectivity levels.

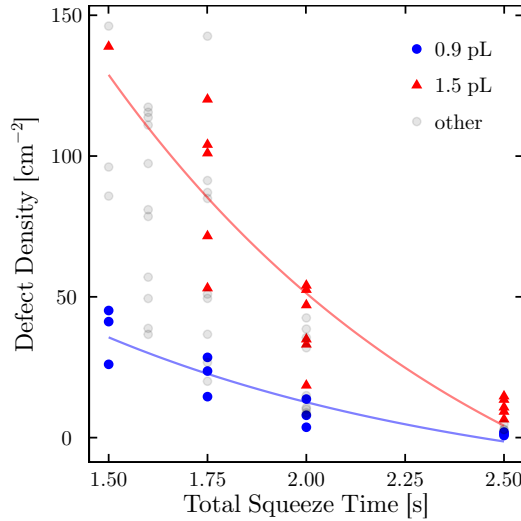


Fig. 5.5. Defectivity as a function of total squeeze time for a fixed test stamp with droplet patterns dispensed with a Xaar1002 AMP [data reproduced from Khusnatdinov *et al.*,¹⁷⁵ light-gray data points relate to other experimental conditions that are not of primary interest here].

5.2 Digital Conductor Printing onto 2.5D Substrates

Inkjet printing of conductors onto non-flat substrates was investigated using the findings presented in Chapter 4. The following sections present the filling of blind via connections for powering buried LED dies as well as the generation of the electrode surfaces used in mass spectrometry applications.

5.2.1 Blind Via Connections

In the investigated application, bare LED dies were incorporated into a matrix of polymeric materials from a RMPD[®] process, which produces patterned films using photosensitive materials.¹⁷⁶ Blind via connections to the contact pads of the LEDs were provided in the top film covering the LED dies, having a diameter of 90 μm and a varying depth of 25 to 45 μm . The process produced steep, 90° walls and sharp, convex corners. The combination of these features poses a challenge to the inkjet printing of the conductors. The locally increased capillary pressure around the rim enhances the thinning of the film close to the convex corner and may result in dewetting. Therefore the resistance of the electrical conduction path will strongly increase, or the path might even be fully disconnected. Current crowding and strong local Joule heating were therefore expected to be the main challenges.

To investigate the performance of the printed blind via connection, specimen were prepared by producing the top layer including the vias on a sputtered gold film. To minimize the influence of the resistance of the conduction path on the top of the RMPD[®] 420 μm wide lines were printed, which ensured consistent

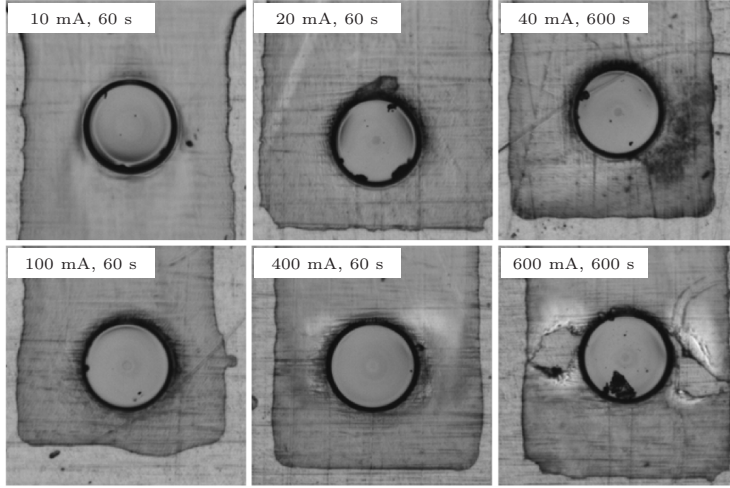


Fig. 5.6. Microscopic images of the inlet of the investigated via connection from the top of a patterned RMPD[®] substrate onto a gold bottom electrode.

conduction to the rim of the via. Thermal sintering for 30 minutes at 150 °C was performed as a benchmark for the achievable performance of the connection.

Printed single layers showed an average resistance of 4.6Ω with a standard deviation 2.7Ω . The strong variation can hereby be attributed to the 30% variability in the length of the via connection, differences in wetting on the top surface as well as the changing thickness of the metal around the rim and the sidewalls of the via. Increasing the deposited volume by a factor of three reduced the average resistance to 1.9Ω . The standard deviation of 1Ω still reflects strong variations, which may be counteracted by appropriate circuit layouts.

To assess the durability of the connection a constant current was applied to the samples for a given time and the resistivity was monitored. Negligible change was found in the resistance value for currents up to 80 mA applied for 60 s. For values higher than 100 mA the resistance did rise appreciably until detachment of the silver layer from the polymer was observed at 400 mA. Figure 5.6 presents micrographs of the tested via connections. The shape and location of the lift-off for 400 and 800 mA corroborated our assumption of current crowding and Joule heating being key failure modes. It is noteworthy that at currents of 400 and 500 mA a tendency to lower overall resistance of the connection was found, indicating a sufficient temperature development for continued sintering as observed in rapid electrical sintering.¹²⁸ Exposing the structures to 20 mA and 40 mA for 600 s showed no change in the electrical properties, which proved the basic applicability of the process to inkjet printing of blind vias.

To improve reliability of the overall process, printing was modified to have a triple layer of silver applied to the RMPD[®] surface, while additional volume was deposited in the area of the via connection to compensate for the volume variation induced by the varying thicknesses of 160 to 290 pL. The track formation on the top surface was further improved by printing at a substrate temperature of 70 °C,

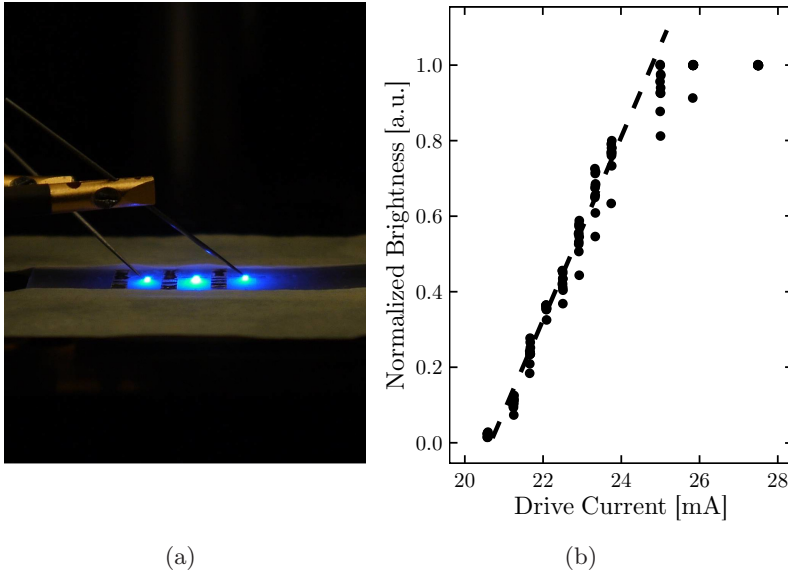


Fig. 5.7. (a) Series connection of three LED produced by inkjet printing with subsequent wet sintering driven at a voltage of 8.5 V at a current of <10 mA, (b) normalized intensity as a function of the applied current for an LED by the described process [70 °C substrate temperature, 100 μ m polyimide absorber, flash energy 350 J, pulse width 0.58 ms, repetition rate 4 Hz, sintering duration 6 s]

which assisted pinning of the contact line and reduced the influence of varying wetting properties on the RMPD[®] substrate.

Based on the findings presented in Section 4.5.3, passively optimized wet IPL curing was employed to sinter the structures. Freshly printed specimen were subjected to flashes with an energy of 350 J at a repetition frequency of 4 Hz. An optimal sintering result was found with a 100 μ m thick polyimide absorber after a minimum exposure of six seconds, totalling 24 flashes. Sintering attempts with a white background had failed to provide consistent results, as conduction paths were disrupted on the top layer or close to the rim of the via, where the strongest temperature gradient was expected during the course of sintering.

Figure 5.7 (a) shows a produced series connection of three LEDs. The LEDs were driven just above the threshold of 8.5 V with approximately 10 mA of current delivered from the internal resistance of the setup. The arrangement was furthermore operated at 9.5 V and 20 mA with a series resistor of 120 Ω to provide sufficient current. The response of a single LED driven by the internal series resistance of the conductors is shown in Figure 5.7 (b), where intensity was measured as the graylevel recorded by a CCD chip. A linear relationship could be observed up to 25 mA where the CCD started to saturate.

5.2.2 Printing Conductors on 3D Printed Parts

Creating arbitrarily shaped electrodes is of interest for many applications, but is often hindered by manufacturing complexity and cost. One example is the quadrupole antenna used in linear ion traps for mass spectrometry, which is typically produced by a combination of wire erosion and CNC machining. The choice of materials and manufacturing steps results in a relatively expensive and heavy device.

We attempted to produce a linear ion trap by the combination of low-cost 3D printing with the capability to print metallic nanoparticles using inkjet. For the 3D printing of the hyperbolic electrodes a DLP-SLA system (Perfactory 3 Mini, EnvisionTEC, Germany) was chosen. 3D shapes were generated by selectively cross-linking a photopolymer on a build-substrate by means of a projector. The produced layer was then separated from the build plate and retracted in the normal direction by a defined distance, so that liquid from the surrounding reservoir could fill the gap with fresh resin.¹⁷⁷ The pixelation of the different layers by the projector and the discrete movement typically resulted in clear voxel contours. Techniques such anti-aliasing and pixel shifting¹⁷⁸ were available to mitigate some of the effects and produce smoother prints.

Initial experiments with inkjet printing onto 3D printed specimen produced with a wet layer thickness of 25 μm revealed regular patterns in the glossy finish of sintered silver layers, which could impede application due to local changes in the electric field. In addition local dewetting was observed, which appeared to correlate with the surface roughness.

To optimize the resulting finish a smaller layer thickness was attempted in the 3D production of the electrodes. Figure 5.8 depicts the resulting finish, where the direction of print is from left-to-right. The micrographs revealed a pattern parallel to the build direction, which was independent of the layer thickness. It was assumed that this resulted from variations in the projection of the image into the photopolymer bath or the limited resolution of the digital light processor (DLP) and the accompanying voxel profiles. No clear or repetitive patterns could be recognized in the horizontal direction of the FFT representations (d)-(e). The influence of the layer thickness could be detected perpendicular to the printing direction. For the standard setting of 25 μm repetitive ripples were visible, which correlate the printer's layer thickness to the FFT. These variations inhibited a thin coating, as the rim of the underlying structure increases the capillary pressure and the thin film disrupted. With decreasing layer thickness the patterns in the vertical direction were indiscernible.

The shape of the 3D printed electrodes did not require the active control in height of the printhead. Printing was therefore performed along the long axis of the electrode, with a nominal droplet volume of 50 pL and a substrate velocity of 50 mm s^{-1} at a frequency of 1 kHz. The misplacement due to the flight time difference was thereby restricted to about 20 μm between the highest and lowest surface. In view of the surface variations discussed above, multi-layer printing was required to allow for a sufficient coverage and homogenization of the surface.

Sintering was limited due to the thermal sensitivity of the 3D-printed parts, which were found to delaminate and warp at temperatures above 200 °C. Oven sintering with extended sintering times of 30 minutes was chosen for these ex-

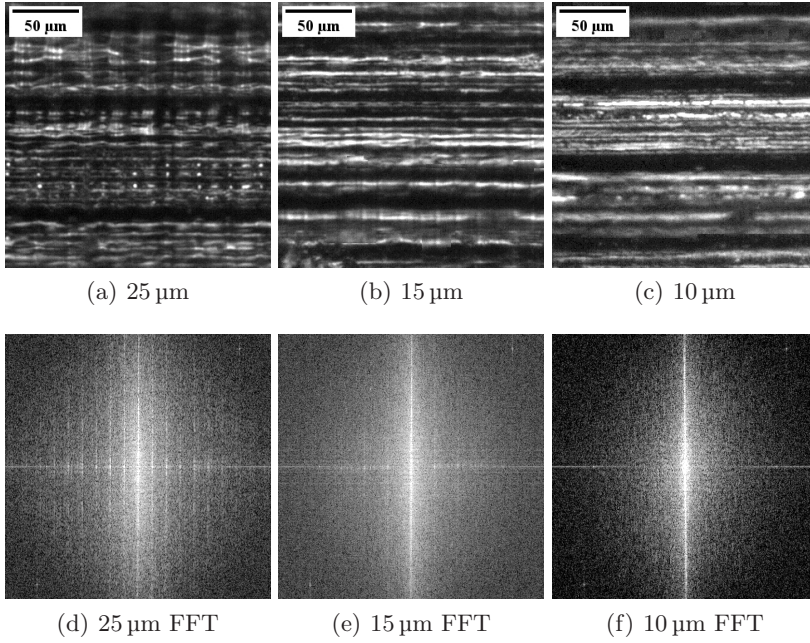


Fig. 5.8. Micrographs of the top surface of 3D printed electrode substrates with layer thicknesses of 10, 15 and 25 μm (a–c, build direction left-to-right) and the corresponding 2D Fourier transforms of the images (d–f).

periments to ensure that trapped gasses and humidity were removed from the samples to comply with the results presented in Section 4.6.

It was found that curing of the multi-layer prints at 100 $^{\circ}\text{C}$ was insufficient to drive off the solvent of the ink, which left the deposits in wet state. The other settings of 125, 150 and 175 $^{\circ}\text{C}$ produced dry and consistent sintering results with the expected decrease in resistance with increasing cross-sectional area of the deposit. With the application of 4–5 layers of ink, all sintering settings produced resistances lower than 500 $\text{m}\Omega\text{cm}^{-1}$. The deposition of 5 layers cured at 175 $^{\circ}\text{C}$ yielded the lowest resistance of 200 $\text{m}\Omega\text{cm}^{-1}$. However, a curing temperature of 150 $^{\circ}\text{C}$ was chosen as compromise between thermal impact on the polymeric material and the achievable electrical performance. This yielded a total resistance of 2 Ω per electrode. Compared to specimen that were electroplated with a 130 μm thick copper-nickel film this value was still a factor of two higher, but sufficient to drive the ion trap.

5.2.3 Summary

The usage of inkjet printed conductors in two different applications was successfully demonstrated.

Blind via connections were filled with silver ink and subsequently dried and sintered using the passively damped photonic sintering approach. Coatings were

shown to withstand currents of 40 mA for extended periods of time without damage induced by Joule heating. A series connection of LEDs was produced and showed the applicability of the process in a R2R application.

Further a hybrid approach was demonstrated, consisting of a DLP 3D printing process and the conductive coating of the specimen with inkjet printing. The observed surface structure was found to originate from the layer thickness used in the DLP process. Optimization of the DLP process showed major improvement of the roughness in the build direction, while a lateral variation remained. Inkjet printing of a conductive coating onto 3D printed electrode bodies of the ion trap was performed and produced acceptable results of $2\ \Omega$ per electrode when performing thermal sintering at 150 °C for 30 minutes.

Conclusion

The goal of this thesis was to explore two critical areas in the Lab2Fab transition for inkjet printed functionalities: (a) the experimental methods for the study of droplet formation and reliability from industrial inkjet printheads and (b) the post-processing techniques enabling the conversion of solution-based metallic nanoparticle inks into conductive structures.

A stroboscopic technique was developed to produce images with high temporal and high spatial resolution. The fast and slow axes of a laser diode were used to produce an illumination confined to the vicinity of the droplet trajectory with pulse widths shorter than 50 ns. The projected shadow of a droplet was then swept across a CCD sensor using a MEMS micro-mirror to produce sharp images of droplet formation at ten instances during the travel from the nozzleplate towards the substrate. This technique enabled the study of the droplet formation process, the creation of satellites as well as secondary tailing.

Reliability was studied using a linescan camera-based approach, where each droplet ejected from the printhead width was captured. Continuous background illumination was found crucial to accommodate variations in droplet velocity and starting position. Statistical data analysis was then used to extract the Gaussian distributions of the droplet and background pixels from the the resulting low contrast images. The statistics were used in a histogram matching transformation to enable fault-tolerant binarization of the recorded images and identification of missing droplets with respect to the printed image. Using temporal oversampling the technique was shown to provide qualitative data on droplet velocity variations.

Ways of improving post-processing using intense pulsed light (IPL) processing were also assessed. IPL was found to produce comparable sintering results to convective oven sintering in less than 0.5% of the typical time required. Wet IPL processing was assessed for the inline sintering of nanoparticle deposits without the need for intermediate drying. The spectral composition of the light resonating in the chamber was altered by employing various absorber materials in combination with a broadband Xenon light. It was shown that damping the blue part of the spectrum was beneficial as it prevented thermal runaway. Furthermore, a portion of the red part of the spectrum was retained for it provides indirect heating and to avoid redeposition of evaporated solvent in the vicinity of the

sintered tracks. This passive filtering concept was found to optimize both line conformation and electrical performance and produced resistance values lower than $5\ \Omega\text{ cm}^{-1}$ in less than ten seconds on polyimide. The approach was successfully applied to other low-cost substrates, yielding for example resistance values of $3\text{--}4\ \Omega\text{ cm}^{-1}$ on bare PET. Alternatively, shaping the energy delivered by the arc lamp was investigated using a copper oxide ink. It was shown that the amplitude could be tailored so that drying, reduction and sintering are accomplished in a single sintering step.

The developed methods were further applied to use cases in the field of digital fabrication. The ejection of 2.8 pL droplets at 11.6 kHz for the use in nanoimprint lithography was achieved by a suitable drive of a commercial printhead. The meniscus pressure was found to further reduce volumes to 2.4 pL at constant droplet velocities within a stable meniscus pressure window. By altering the geometry of the printhead, the volume was reduced to as low as 0.9 pL, which enabled a reduction in squeeze time by 500 ms, or 20%, at a constant defect density.

The optimization of the post-process for solution-processable metal inks was applied to blind via-interconnects to buried LED dies. Cracking at the rim of the vias was observed at currents above 400 mA. Currents of 20 to 40 mA, which were required to drive the LEDs, did not show degradation and a series connection of three LEDs was produced on structured polymer substrates.

Nanoparticle deposits sintered thermally at 200 °C did not exhibit measurable outgassing from incomplete sintering when exposed to low-pressure. Inkjet printing of a conductive coating onto the 3D-printed electrode bodies for quadrupole ion traps used in mass spectrometry was performed and produced acceptable results of $2\ \Omega$ per electrode when performing thermal sintering at 150 °C for 30 minutes.

Acknowledgements

This thesis would not have been possible without the support from all those people I was so lucky to call my colleagues and friends during the past years. I am indebted to them for their guidance, helping hands, discussions and good times that aided both, the development of the ideas in this thesis and myself. Therefore I would like to thank each and every one who has a stake in this work and apologize for anyone a fail to name.

I would like to extend my sincerest gratitude to Werner Zapka for planting the seed for this work. His unswerving enthusiasm and strong belief in our work helped to find solutions where these seemed absent.

The work presented in this thesis was conducted at Xaar plc in Stockholm in close cooperation with the Royal Institute of Technology KTH. The research was in part financially supported by the iPack VINN Excellence Center and the European Community's FP7 Program (Grant Agreement No. CP-TP 228686 & 285045). I would also like to thank the management at Xaar plc that enabled me to do this as an industrial student and use part our work for this thesis.

I should also thank my supervisors, Carl-Mikael Zetterling and Lirong Zheng, who welcomed me into their groups. The interaction between our seemingly distant fields was a great opportunity to learn new concepts and approach problems differently.

None of the work of the past years would have been possible without my colleagues at Xaar. There is my extended family from Advanced Applications, Maik, Renzo, Jürgen and Wolfgang, who I shared many days (and partially nights) with. You were always there, for discussions, firefighting, good (and a few bad) times or to just bring all our ideas to life. I don't know where I would be without you. I will of course not forget about the folks from the Cambridge office and would like to thank each and every one, and specifically Tomáš, Peter, Mario, Maëlle, Matt, Edward, Anja, Tony, Mani, Angus, Tim and Nathan.

I also remember all the students that were a passing part of the group and were responsible for many of the results. Thank you Moritz, Stefan, Janosch, Ali, Fritz, George, Matthias, Max, Chris, Markus, Andy, Uwe, Mirko, Karsten, and all the ones that I now forgot to mention.

The projects done in collaboration were often the most fruitful thanks to the wonderful and brilliant people I was allowed to work with. I specifically would like to thank Van Truskett, Matt Shafran, Whitney Longsine, Matt Traub, Roger Bollström, Ian Rawson, Andrew Edd, Kurt Schroeder, Fredrik Jonsson, Ingo Sander, Tri Tuladhar, Frits Dijkstra, Steven Hoath and Gustaf Mårtensson.

Being part of a scientific community was of great benefit over the years and I would therefore like to thank the Society of Imaging Science and Technology IS&T for welcoming me in their midst and allow me to work with them. I would especially like to acknowledge Suzanne Grinnan and the IS&T staff, as well as all the colleagues on the committees, specifically Reinhard Baumann, Mike Willis, Jim Stasiak, Ron Askeland, Wolfgang Schmidt, Jolke Perelaer, Katrina Donovan, Patrick Smith, Enrico Sowade, Brian Derby, Atsushi Tomotake and Teruaki Mitsuya.

Lastly I would like to thank my family and friends for their unconditional love and support.

References

- [1] P. B. Umbanhowar, V. Prasad, and D. A. Weitz. Monodisperse Emulsion Generation via Drop Break Off in a Coflowing Stream. *Langmuir*, 16(2): 347–351, 2000.
- [2] H. D. Smyth and A. J. Hickey. Multimodal Particle Size Distributions Emitted from HFA-134a Solution Pressurized Metered-Dose Inhalers. *AAPS PharmSciTech*, 4(3):1–11, 2003.
- [3] O. Semprez, J. Jonkers, R. Apetz, and M. Yoshioka. Making Extreme-UV Lightsources a Reality. *SPIE Newsroom*, 2012.
- [4] I. M. Hutchings, G. D. Martin, and S. D. Hoath. Introductory Remarks. In *Fundamentals of Inkjet Printing*, chapter 1, pages 1–12. John Wiley & Sons, Ltd, 2015.
- [5] H. Wijshoff. The Dynamics of the Piezo Inkjet Printhead Operation. *Physics Reports*, 491(4-5):77–177, 2010.
- [6] J. Przybyla, R. Vina, and J. Hintzman. Something for Nothing - Developing MEMS Silicon for a Vertically Integrated Market Leading Business - The example of HP Thermal Inkjet. pages 52–56, 2015.
- [7] T. Mitsuya, May 2019. Personal Communication.
- [8] A. Tomotake, May 2019. Personal Communication.
- [9] A. Eranpurwala, May 2019. Personal Communication.
- [10] *Duralink Printhead*. Memjet, 2017. Datasheet.
- [11] *Precision Core - Next-Generation Inkjet Technology*. Epson, September 2013. White Paper.
- [12] R. Imanishi. Design Studies on Ink Jet Printhead to Improve its Throughput. In *International Conference on Digital Printing Technologies and Digital Fabrication*, pages 20–23, 2012.
- [13] *Samba G3L Printhead Features*. Fujifilm Dimatix, February 2015. Datasheet.
- [14] *StarFire SG1024/MC*. Fujifilm Dimatix, October 2013. Datasheet.
- [15] *Xaar 5601*. Xaar, November 2018. Datasheet.
- [16] A. Tomatake. Topics of Inkjet Printing Technology in DRUPA 2016. *Journal of the Imaging Society of Japan*, 55(5):541–548, 2016.

- [17] J. Stoffel. Improving the Performance of Inkjet and Laser Printing Through Paper Modification. In *International Conference on Non Impact Printing*, pages 577–579, 2007.
- [18] J. Stasiak. Technological Advances in 3D Printing - Voxel Scale Design and Engineering. In *The IJC 2018 Conference*, San Diego, 2018.
- [19] A. V. Yakovlev, V. A. Milichko, V. V. Vinogradov, and A. V. Vinogradov. Inkjet Color Printing by Interference Nanostructures. *ACS Nano*, 2016.
- [20] U. Bürklin. Industrial Printed Seed-Layer for Front Side Metallization of Crystalline Silicon Solar Cells. In *International Conference on Digital Printing Technologies and Digital Fabrication*, pages 472–475, 2013.
- [21] J. Putaala, J. Niittynen, J. Hannu, S. Myllymäki, E. Kunnari, M. Mäntysalo, J. Hagberg, and H. Jantunen. Capability Assessment of Inkjet Printing for Reliable RFID Applications. *IEEE Transactions on Device and Materials Reliability*, 17(2):281–290, 2017.
- [22] H. Huttunen, P. Ruusuvaori, T. Manninen, K. Rutanen, and R. Ronkka. Dynamic Adaptation of Interconnections in Inkjet Printed Electronics. In *International Conference on Signals and Electronic Systems*, pages 449–452, 2008.
- [23] S. Han, J. Derksen, and J. H. Chun. Extrusion Spin Coating: An Efficient and Deterministic Photoresist Coating Method in Microlithography. *IEEE Transactions on Semiconductor Manufacturing*, 17(1):12–21, 2004.
- [24] F. J. Dijkman, P. C. Duineveld, M. Hack, A. Pierik, J. Rensen, J.-E. Rubingh, I. Schram, and M. Vernhout. Precision Ink Jet Printing of Polymer Light Emitting Displays. *Journal of Materials Chemistry*, 17(6):511, 2007.
- [25] B.-J. de Gans, P. C. Duineveld, and U. S. Schubert. Inkjet Printing of Polymers: State of the Art and Future Developments. *Advanced Materials*, 16(3):203–213, 2004.
- [26] M. Crankshaw, L. Foster, A. Owens, L. Webb, and E. Mayes. From DMP to 40" TV – The Challenges of Scaling-Up Inkjet. In *International Conference on Digital Printing Technologies and Digital Fabrication*, pages 627–630, 2009.
- [27] M. Crankshaw, S. Goddard, M. Dowling, L. Webb, B. Wild, J. Isaac, C. Creighton, and E. Burton. Inkjet Printing of Swathe-Free Displays. In *International Conference on Digital Printing Technologies and Digital Fabrication*, pages 736–739, 2008.
- [28] A. Pierik, F. J. Dijkman, A. Raaijmakers, T. Wismans, and H. Stapert. Quality Control of Inkjet Technology for DNA Microarray Fabrication. *Biotechnology Journal*, 3(12):1581–1590, 2008.
- [29] W. Voit, N. Jackson, K. Preckel, S. Iqbal, I. Reinhold, and W. Zapka. Evaluation of Crosstalk Effects in Inkjet Printing with Xaar 1001. In *International Conference on Digital Printing Technologies and Digital Fabrication*, pages 97–100, 2011.
- [30] A. van der Bos, M.-J. van der Meulen, T. Driessen, M. van den Berg, H. Reinten, H. Wijshoff, M. Versluis, and D. Lohse. Velocity Profile Inside Piezoacoustic Inkjet Droplets in Flight - Comparison between Experiment and Numerical Simulation. *Physical Review Applied*, 1:014004, 2014.

- [31] S. D. Hoath. On International Standards for In-Flight Measurements of Inkjet Drops. *Journal of Imaging Science and Technology*, 62(1):1–8, 2018.
- [32] Y. Kipman, P. Mehta, and E. Nguyen. Low Cost in-situ Drop Analysis System for Ink Jet and other Non-Contact Dispensing Technologies. In *International Conference on Digital Printing Technologies*, pages 522–527, 2011.
- [33] Y. Kipman, P. Mehta, and K. Johnson. Three Methods of Measuring Velocity of Drops in Flight Using Jetxpert. In *International Conference on Digital Printing Technologies and Digital Fabrication*, pages 71–74, 2009.
- [34] A. Fraters. *Inkjet Printing: Bubble Entrainment and Satellite Formation*. Ph.D. thesis, University of Twente, 2018.
- [35] A. Van Der Bos, A. Zijlstra, E. Gelderblom, and M. Versluis. ILIF: Illumination by Laser-Induced Fluorescence for Single Flash Imaging on a Nanoseconds Timescale. *Experiments in Fluids*, 51(5):1283–1289, 2011.
- [36] S. Koekebakker, M. Ezzeldin, A. Khalate, R. Babuška, X. Bombois, P. van den Bosch, G. Scorletti, S. Weiland, H. Wijshoff, R. Waarsing, and W. de Zeeuw. Piezo Printhead Control: Jetting Any Drop at Any Time. In *Model-Based Design of Adaptive Embedded Systems, Embedded Systems*, volume 22, pages 41–85. 2013.
- [37] M. B. G. Wassink, O. H. Bosgra, D. J. Rixen, and S. Koekebakker. Modeling of an Inkjet Printhead for Iterative Learning Control using Bilaterally Coupled Multiports. In *44th IEEE Conference on Decision and Control*, pages 4766–4772, 2005.
- [38] K.-S. Kwon. Methods for Detecting Air Bubble in Piezo Inkjet Dispensers. *Sensors and Actuators A: Physical*, 153(1):50–56, 2009.
- [39] H. Wijshoff. *Structure- and Fluid-Dynamics in Piezo Inkjet Printheads*. Ph.D. thesis, University of Twente, 2008.
- [40] J. Renner. Real-time Process Monitoring of DoD Inkjet Systems by Overlaid Imaging. In *The IJC 2015 Conference*, 2015.
- [41] Y. Kipman, P. Mehta, and K. Johnson. Automated Inkjet Print Head Sustainability Testing. In *International Conference on Digital Printing Technologies*, pages 632–634, Austin, TX, 2010.
- [42] E. Gili, M. Caironi, and H. Sirringhaus. Picoliter Printing. In G. P. Wiederrecht, editor, *Handbook of Nanofabrication*, pages 183–196. Elsevier, 2010.
- [43] H. Pan, S. H. Ko, and C. P. Grigoropoulos. Thermal Sintering of Solution-Deposited Nanoparticle Silver Ink Films Characterized by Spectroscopic Ellipsometry. *Applied Physics Letters*, 93(23), 2008.
- [44] K.-S. Moon, H. Dong, R. Maric, S. Pothukuchi, A. Hunt, Y. Li, and C. P. Wong. Thermal Behavior of Silver Nanoparticles for Low-Temperature Interconnect Applications. *Journal of Electronic Materials*, 34(2):168–175, 2005.
- [45] J. Felba, K. Nitsch, T. Piasecki, P. Paluch, A. Moscicki, and A. Kinart. The influence of Thermal Process on Electrical Conductivity of Microstructures Made by Ink-Jet Painting with the use of Ink Containing Nano Sized Silver Particles. *IEEE-NANO*, 8:408–411, 2009.
- [46] I. Reinhold, M. Thielen, W. Voit, W. Zapka, R. Götzen, and H. Bohlmann. Inkjet Printing of Electrical Vias. In *EPMC*, pages 2–5, 2011.

- [47] S. Wünscher, R. Abbel, J. Perelaer, and U. S. Schubert. Progress of Alternative Sintering Approaches of Inkjet-Printed Metal Inks and their Application for Manufacturing of Flexible Electronics. *RSC Advances*, 2:10232–10261, 2014.
- [48] D. Soltman and V. Subramanian. Inkjet-Printed Line Morphologies and Temperature Control of the Coffee Ring Effect. *Langmuir*, 24(5):2224–2231, 2008.
- [49] D. Tobjörk, H. Aarnio, P. Pulkkinen, R. Bollström, A. Määttänen, P. Ihalainen, T. Mäkelä, J. Peltonen, M. Toivakka, H. Tenhu, and R. Österbacka. IR-Sintering of Ink-Jet Printed Metal-Nanoparticles on Paper. *Thin Solid Films*, 520(7):2949–2955, 2012.
- [50] B. J. Kang and J. H. Oh. Geometrical Characterization of Inkjet-Printed Conductive Lines of Nanosilver Suspensions on a Polymer Substrate. *Thin Solid Films*, 518(10):2890–2896, 2010.
- [51] W. Voit, W. Zapka, and A. Menzel. Inkjet Printing of Phase-Change Materials. *International Conference on Digital Printing Technologies and Digital Fabrication*, 2008.
- [52] N. Hopkinson and P. J. Smith. Industrial 3D Inkjet Printing/Additive Manufacturing. In W. Zapka, editor, *Handbook of Industrial Inkjet Printing*, chapter 38, pages 649–660. John Wiley & Sons, Ltd, 2017.
- [53] O. Pabst, J. Perelaer, E. Beckert, U. S. Schubert, R. Eberhardt, and A. Tünnermann. All Inkjet-Printed Piezoelectric Polymer Actuators: Characterization and Applications for Micropumps in Lab-on-a-Chip Systems. *Organic Electronics*, 14(12):3423–3429, 2013.
- [54] R. Thalheim, M. Polomoshnov, and R. Zichner. Printing of Dielectric and Conductive Patterns on Non-Planar Surfaces Using Dispensing and Inkjet. In *Printing for Fabrication*, 2018.
- [55] J. Stringer and B. Derby. Limits to Feature Size and Resolution in Ink Jet Printing. *Journal of the European Ceramic Society*, 29(5):913–918, 2009.
- [56] T. Tano, H. Tomono, A. Onodera, K. Yutani, A. Murakami, K. Suzuki, D. Group, and C. Technology. Novel Fine Electrode Patterning Using Inkjet Method and Its Application to All-printed Organic TFT Backplane. *International Conference on Digital Printing Technologies and Digital Fabrication*, pages 631–634, 2009.
- [57] J. Z. Wang, Z. H. Zheng, H. W. Li, W. T. S. Huck, and H. Sirringhaus. Dewetting of Conducting Polymer Inkjet Droplets on Patterned Surfaces. *Nature Materials*, 3(3):171–176, 2004.
- [58] D. J. Resnick, S. V. Sreenivasan, and C. G. Willson. Step & Flash Imprint Lithography. *Materials Today*, pages 34–42, 2005.
- [59] I. Reinhold, M. M. Shafran, W. Longsine, M. M. Traub, Y. Srinivasan, V. N. Truskett, and W. Zapka. High-Speed, Low-Volume Inkjet and its Role in Jet and Flash™ Imprint Lithography. In *International Conference on Digital Printing Technologies and Digital Fabrication*, Philadelphia, PA, 2014.
- [60] A. Sher, D. Woodward, H. Epstein, R. J. Phelps, and P. Rice. Ink Printing. *IEEE Transactions on Electron Devices*, (4), 1972.

- [61] H. Kipphan, editor. *Handbook of Print Media: Technologies and Production Methods*. Springer-Verlag, Berlin, Heidelberg, 2006.
- [62] C. H. Hertz and S. I. Simonsson. Intensity Modulation of Ink-Jet Oscillographs. *Medical & Biological Engineering*, 7(3):337–340, 1969.
- [63] J. M. Chwalek. Kodak ’s Stream Inkjet Technology and the Future of Digital Printing. In *International Conference on Digital Printing Technologies and Digital Fabrication*, 2010.
- [64] M. Piatt, D. Bugner, J. M. Chwalek, and J. Katerberg. KODAK’s Stream Inkjet Technology. In *Handbook of Industrial Inkjet Printing*, pages 351–360. Wiley–VCH, 2017.
- [65] C. Ellinger and Y. Xie. Lateral Merging Continuous Inkjet. In *International Conference on Digital Printing Technologies and Digital Fabrication*, pages 343–346, 2011.
- [66] H. P. Le. Progress and Trends in Ink-Jet Printing Technology. *J. Imaging Sci. Technol.*, 42(1):49–62, 1998.
- [67] N. Morita, A. A. Khalate, A. M. Buul, and H. Wijshoff. Inkjet Printheads. In *Fundamentals of Inkjet Printing*, chapter 3, pages 57–92. John Wiley & Sons, Ltd, 2015.
- [68] A. Hudd. Inkjet Printing Technologies. In S. Magdassi, editor, *The Chemistry of Inkjet Inks*, pages 3–16. World Scientific, 2009.
- [69] T. L. Weber. HP’s Jet Fusion 3D Printing Technology : Enabling the Next Industrial Revolution. In *Printing for Fabrication*, 2016.
- [70] J. Przybyla, C. Bakker, E. Martin, and J. Gardner. High Definition Nozzle Architecture Inkjet Printhead for Commercial / Industrial Markets. In *International Conference on Digital Printing Technologies and Digital Fabrication*, pages 320–325, 2015.
- [71] R. Ulacia. HP Pagedwide System Printhead Architecture for a Compact Printer. In *International Conference on Digital Printing Technologies and Digital Fabrication*, pages 317–319, 2015.
- [72] J. Brünahl. *Physics of Piezoelectric Shear Mode Inkjet Actuators*. Ph.D. thesis, KTH - Royal Institute of Technology, 2003.
- [73] F. J. Dijkman. Hydrodynamics of Small Tubular Pumps. *Journal of Fluid Mechanics*, 139:173–191, 1984.
- [74] N. Reis, C. Ainsley, and B. Derby. Viscosity and Acoustic Behavior of Ceramic Suspensions Optimized for Phase-Change Ink-Jet Printing. *Journal of the American Ceramic Society*, 88(4):802–808, 2005.
- [75] R. Badie and D. F. De Lange. Mechanism of Drop Constriction in a Drop-on-Demand Inkjet System. *Proceedings of the Royal Society A: Mathematical, Physical and Engineering Sciences*, 453(1967):2573–2581, 1997.
- [76] A. U. Chen and O. A. Basaran. A New Method for Significantly Reducing Drop Radius without Reducing Nozzle Radius in Drop-on-Demand Drop Production. *Physics of Fluids*, 14(1), 2002.
- [77] M.-J. van der Meulen. *Meniscus Motion and Drop Formation in Inkjet Printing*. PhD thesis, University of Twente, 2015.
- [78] P. A. Cotterill, D. Nigro, I. D. Abrahams, E. Garcia-Neefjes, and W. J. Parnell. Thermo-Viscous Damping of Acoustic Waves in Narrow Channels:

- A Comparison of Effects in Air and Water. *The Journal of the Acoustical Society of America*, 144(6):3421–3436, 2018.
- [79] M. Crankshaw, M. Rulman, H. Zarezadeh, M. Douaire, and A. Condie. Ink Recirculation – Xaar TF Technology: A Study of the Benefits. In *Printing for Fabrication*, pages 207–211, 2016.
- [80] Y. Domae, Y. Yamamura, S. Horiguchi, and M. Tachibana. New Print Head Technology for High Productivity and Stability. In *International Conference on Digital Printing Technologies and Digital Fabrication*, pages 15–19, 2014.
- [81] T. Tuladhar. Measurement of Complex Rheology and Jettability of Inkjet Inks. In W. Zapka, editor, *Handbook of Industrial Inkjet Printing*, chapter 22, pages 409–430. John Wiley & Sons, Ltd, 2017.
- [82] S. D. Hoath, S. Jung, W.-K. Hsiao, and I. M. Hutchings. How PEDOT:PSS Solutions Produce Satellite-Free Inkjets. *Organic Electronics*, 13(12):3259–3262, 2012.
- [83] F. J. Dijkman. Hydro-Acoustics of Piezoelectrically Driven Ink-Jet Print Heads. *Flow, Turbulence and Combustion*, 61:211–237, 1999.
- [84] S. D. Hoath. Multi Pulse Train Modeling of Piezo-Drop-on-Demand Inkjet Print-Head Response. *Journal of Imaging Science and Technology*, 60(4):404041–404049, 2016.
- [85] J. de Jong, G. de Bruin, H. Reinten, M. van den Berg, H. Wijshoff, M. Versluis, and D. Lohse. Air Entrapment in Piezo-Driven Inkjet Printheads. *The Journal of the Acoustical Society of America*, 120(3):1257, 2006.
- [86] A. Fraters, T. Segers, M. V. D. Berg, H. Reinten, H. Wijshoff, and D. Lohse. Shortwave Infrared Imaging Setup to Study Entrained Air Bubble Dynamics in a MEMS - Based Piezo-Acoustic Inkjet Printhead. *Experiments in Fluids*, 60(123):1–12, 2019.
- [87] L. A. Crum. Rectified diffusion. *Ultrasonics*, pages 215–223, 1984.
- [88] J. de Jong, R. J. M. Jeurissen, H. Borel, M. van den Berg, H. Wijshoff, H. Reinten, M. Versluis, A. Prosperetti, and D. Lohse. Entrapped Air Bubbles in Piezo-Driven Inkjet Printing: Their Effect on the Droplet Velocity. *Physics of Fluids*, 18(12), 2006.
- [89] J. Brünahl, A. Condie, M. Crankshaw, T. Cruz-Uribe, and W. Zapka. Xaar’s Inkjet Printing Technology and Applications. In *Handbook of Industrial Inkjet Printing*, chapter 15, pages 285–312. John Wiley & Sons, Ltd, 2017.
- [90] C. Sun. Recirculating Printheads for Industrial Applications. In *The IJC 2018 Conference*, 2018.
- [91] J. Corral. Introducing New Konica Minolta Print Heads. In *The IJC 2015 Conference*, 2018.
- [92] J. Eggers. Tropfenbildung. *Physikalische Blätter*, 1997.
- [93] J. de Jong, H. Reinten, H. Wijshoff, M. van den Berg, K. Delescen, R. van Dongen, F. Mugele, M. Versluis, and D. Lohse. Marangoni Flow on an Inkjet Nozzle Plate. *Applied Physics Letters*, 91(20):204102, 2007.
- [94] P. Boltryk. Multiphysics Modeling of Piezo Inkjet Printheads. In *Comsol Conference*, Cambridge, UK, 2014.

- [95] F. J. Dijkman and P. C. Duineveld. Droplet-on-Demand Printing of Polymer Solutions. In *International Conference on Digital Printing Technologies and Digital Fabrication*, pages 214–218, Portland, OR, 2015.
- [96] J. E. Fromm. Numerical Calculation of the Fluid Dynamics of Drop-on-Demand Jets. *IBM Journal of Research and Development*, 28(3):322–333, 1984.
- [97] C. Clasen, P. M. Phillips, L. Palangetic, and J. Vermant. Dispensing of Rheologically Complex Fluids: The Map of Misery. *AIChE Journal*, 58(10):3242–3255, 2012.
- [98] J. R. Castrejon-Pita and I. M. Hutchings. High Speed Shadowgraphy for the Study of Liquid Drops. In J. Klapp, A. Medina, A. Cros, and C. A. Vargas, editors, *Fluid Dynamics in Physics, Engineering and Environmental Applications*, pages 121–137. Springer, 2013.
- [99] R. Johannes and S. Karl. Multi Wavelength Imaging for Drop Watching Systems. In *Proceedings of the 5th International Scientific Conference - Printing Future Days 2013*, pages 73–78, Chemnitz, Germany, 2013. Technical University Chemnitz.
- [100] Y. Sabharwal. Digital Camera Technologies for Scientific Bio-Imaging. Part 4: Signal-to-Noise Ratio and Image Comparison of Cameras. *Microscopy and Analysis*, 26(1):4–8, 2012.
- [101] G. D. Martin, W. C. Price, and I. M. Hutchings. Measurement of Inkjet Drop Volume—The Role of Image Processing. *Journal of Imaging Science and Technology*, 60(4):404011–404019, 2016.
- [102] W. Wehl. *Akustik und Fluidmechanik in Kanälen und Düsen von Tintenschreibwerken*. Ph.D. thesis, TU München, 1984.
- [103] S. Sack. *Detektion und Charakterisierung von Verunreinigungen in piezokeramischen Mikrokanälen*. Diploma thesis, Technische Universität Dresden, 2013.
- [104] R. J. M. Jeurissen, H. Wijshoff, M. van den Berg, H. Reinten, and D. Lohse. Regimes of Bubble Volume Oscillations in a Pipe. *The Journal of the Acoustical Society of America*, 130(5):3220–3232, 2011.
- [105] Epson. Precision Core - Next-Generation Inkjet Technology, 2013.
- [106] Canon Solutions America. Océ Crystalpoint Technology. Technical report, 2016.
- [107] N. J. M. Bosch. *Iterative Learning Control on an Inkjet Printhead*. Master thesis, University of Eindhoven, 2005.
- [108] M. Ezzeldin, P. van den Bosch, and S. Weiland. Experimental-Based Feed-forward Control for a DoD Inkjet Printhead. *Control Engineering Practice*, 21(7):940–952, 2013.
- [109] H. Mizes, J. Folkins, E. Viturro, Y. Eun, and D. Mantell. High Speed Xerox Inkjet Technology. In *International Conference on Digital Printing Technologies and Digital Fabrication*, pages 340–343, 2010.
- [110] H. Mizes, S. Spencer, C. Sjolander, and A. Yeh. Active Alignment of Print Heads. In *International Conference on Digital Printing Technologies and Digital Fabrication*, pages 711–714, 2009.
- [111] R. C. Gonzalez and R. E. Woods. *Digital Image Processing*. Pearson/Prentice Hall, 2008.

- [112] G. R. Ruschau, S. Yoshikawa, and R. E. Newnham. Resistivities of Conductive Composites. *Journal of Applied Physics*, 72(3):953–959, 1992.
- [113] W. Wu, S. H. Brongersma, M. Van Hove, and K. Maex. Influence of Surface and Grain-Boundary Scattering on the Resistivity of Copper in Reduced Dimensions. *Applied Physics Letters*, 84(15):2838–2840, 2004.
- [114] J. De Vries. Resistivity of Thin Au films as a Function of Grain Diameter and Temperature. *Journal of Physics F: Metal Physics*, 18(2):515, 1988.
- [115] G. E. Jabbour, M. Abulikamu, H. W. Choi, and H. M. Haverinen. Reactive Inkjet Printing as a Tool for in situ Synthesis of Self-Assembled Nanoparticles. In S. Magdassi and A. Kamyshny, editors, *Nanomaterials for 2D and 3D Printing*, chapter 4, pages 69–82. Wiley-VCH, 2017.
- [116] A. Kamyshny and S. Magdassi. Metallic Nanoinks for Inkjet Printing of Conductive 2D and 3D Structures. In S. Magdassi and A. Kamyshny, editors, *Nanomaterials for 2D and 3D printing*, pages 119–160. Wiley-VCH, 2017.
- [117] A. Lee, K. Sudau, K. H. Ahn, S. J. Lee, and N. Willenbacher. Optimization of Experimental Parameters to Suppress Nozzle Clogging in Inkjet printing. *Industrial and Engineering Chemistry Research*, 51(40):13195–13204, 2012.
- [118] M. Grouchko, A. Kamyshny, C. F. Mihailescu, D. F. Anghel, and S. Magdassi. Conductive Inks with a ”Built-In” Mechanism That Enables Sintering at Room Temperature. *ACS Nano*, 5(4):3354–3359, 2011.
- [119] J. Olkkonen, J. H. Leppäniemi, T. Mattila, and K. Eiroma. Sintering of Inkjet Printed Silver Tracks with Boiling Salt Water. *Journal of Materials Chemistry C*, 2(18):3577, 2014.
- [120] W. Zapka, W. Voit, C. Loderer, and P. Lang. Low Temperature Chemical Post-Treatment of Inkjet Printed Nano-Particle Silver Inks. *International Conference on Digital Printing Technologies and Digital Fabrication*, 2008.
- [121] Z. Z. Fang and H. Wang. *Sintering of Advanced Materials*. Woodhead Publishing, 2010.
- [122] K. K. Nanda. Size-Dependent Melting of Nanoparticles: Hundred Years of Thermodynamic Model. *Pramana - Journal of Physics*, 72(4):617–628, 2009.
- [123] S. Wünscher, S. Stumpf, A. Teichler, O. Pabst, J. Perelaer, E. Beckert, and U. S. Schubert. Localized Atmospheric Plasma Sintering of Inkjet Printed Silver Nanoparticles. *Journal of Materials Chemistry*, 22(47):24569, 2012.
- [124] S. Wünscher, S. Stumpf, J. Perelaer, and U. S. Schubert. Towards Single-Pass Plasma Sintering: Temperature Influence of Atmospheric Pressure Plasma Sintering of Silver Nanoparticle Ink. *Journal of Materials Chemistry C*, 2:1642, 2014.
- [125] I. Reinhold, C. E. Hendriks, R. Eckardt, J. M. Kranenburg, J. Perelaer, R. R. Baumann, and U. S. Schubert. Argon Plasma Sintering of Inkjet Printed Silver Tracks on Polymer Substrates. *Journal of Materials Chemistry*, 19(21):3384, 2009.
- [126] J. Niittynen, E. Halonen, and M. Mäntysalo. Conductivity and Adhesion Study of Plasma-sintered Nanoparticle Silver Ink. In *LOPEC*, pages 134–138, 2011.

- [127] S. Jang, D.-J. Lee, D. Lee, and J. H. Oh. Electrical Sintering Characteristics of Inkjet-Printed Conductive Ag Lines on a Paper Substrate. *Thin Solid Films*, 546:157–161, 2013.
- [128] M. L. Allen, M. Aronniemi, T. Mattila, A. Alastalo, K. Ojanperä, M. Suho-nen, and H. Seppä. Electrical Sintering of Nanoparticle Structures. *Nanotechnology*, 19(17):175201, 2008.
- [129] A. Alastalo, H. Seppä, J. H. Leppäniemi, M. Aronniemi, M. L. Allen, and T. Mattila. Modelling of Nanoparticle Sintering Under Electrical Boundary Conditions. *Journal of Physics D: Applied Physics*, 43(48):485501, 2010.
- [130] J. Perelaer, M. Klokkenburg, C. E. Hendriks, and U. S. Schubert. Mi-crowave Flash Sintering of Inkjet-Printed Silver Tracks on Polymer Sub-strates. *Advanced Materials*, 21:4830–4834, 2009.
- [131] J. Perelaer, R. Abbel, S. Wünscher, R. Jani, T. J. van Lammeren, and U. S. Schubert. Roll-to-Roll Compatible Sintering of Inkjet Printed Features by Photonic and Microwave Exposure: From Non-Conductive Ink to 40% Bulk Silver Conductivity in Less than 15 Seconds. *Advanced Materials*, 24(19): 2620–5, 2012.
- [132] S. F. Jahn, T. Blaudeck, R. R. Baumann, A. Jakob, P. Ecorchard, T. Rüffer, H. Lang, and P. Schmidt. Inkjet printing of conductive silver patterns by using the first aqueous particle-free MOD ink without additional stabilizing ligands. *Chemistry of Materials*, 22(10):3067–3071, 2010.
- [133] E. Sowade, H. Kang, K. Y. Mitra, O. J. Weiß, J. Weber, and R. R. Baumann. Roll-to-Roll Infrared (IR) Drying and Sintering of an Inkjet-Printed Silver Nanoparticle Ink Within 1 Second. *Journal of Materials Chemistry C*, 3 (45):11815–11826, 2015.
- [134] D.-G. Lee, D. K. Kim, Y.-J. Moon, and S.-J. Moon. Effect of Temperature on Electrical Conductance of Inkjet-Printed Silver Nanoparticle Ink During Continuous Wave Laser Sintering. *Thin Solid Films*, 546:443–447, 2013.
- [135] J. H. Choi, K. Ryu, K. Park, and S.-J. Moon. Thermal Conductivity Esti-mation of Inkjet-Printed Silver Nanoparticle Ink During Continuous Wave Laser Sintering. *International Journal of Heat and Mass Transfer*, 85:904–909, 2015.
- [136] J. Niittynen, E. Sowade, H. Kang, R. R. Baumann, and M. Mäntysalo. Comparison of Laser and Intense Pulsed Light Sintering (IPL) for Inkjet-Printed Copper Nanoparticle Layers. *Scientific Reports*, 5:8832, 2015.
- [137] T. Kumpulainen, J. Pekkanen, J. Valkama, J. Laakso, R. Tuokko, and M. Mäntysalo. Low Temperature Nanoparticle Sintering With Continu-ous Wave and Pulse Lasers. *Optics and Laser Technology*, 43(3):570–576, 2011.
- [138] J. West, J. Sears, S. Smith, and M. Carter. Photonic Sintering – An Ex-ample: Photonic Curing of Silver Nanoparticles. In *Sintering of advanced materials - Fundamentals and processes*, pages 275–288. 2010.
- [139] E. Drahi, S. Blayac, A. Borbély, P. Benaben, and A. Borbély. Impact of Ink Synthesis on Processing of Inkjet-Printed Silicon Nanoparticle Thin Films: A Comparison of Rapid Thermal Annealing and Photonic Sintering. *Thin Solid Films*, 574:169–176, 2015.

- [140] M. Cherrington, T. Claypole, D. Gethin, D. Worsley, and D. Deganello. Non-Contact Assessment of Electrical Performance for Rapidly Sintered Nanoparticle Silver Coatings Through Colorimetry. *Thin Solid Films*, 522: 412–414, 2012.
- [141] W.-H. Chung, H.-J. Hwang, S.-H. Lee, and H.-S. Kim. In Situ Monitoring of a Flash Light Sintering Process Using Silver Nano-Ink for Producing Flexible Electronics. *Nanotechnology*, 24(3):035202, 2013.
- [142] B. Polzinger, F. Schoen, V. Matic, J. Keck, H. Willeck, W. Eberhardt, and H. Kueck. UV-Sintering of Inkjet-Printed Conductive Silver Tracks. *11th IEEE International Conference on Nanotechnology*, pages 201–204, 2011.
- [143] M. Hösel and F. C. Krebs. Large-Scale Roll-to-Roll Photonic Sintering of Flexo Printed Silver Nanoparticle Electrodes. *Journal of Materials Chemistry*, 22(31):15683–15688, 2012.
- [144] A. Chiolerio, G. Maccioni, P. Martino, M. Cotto, P. Pandolfi, P. Rivolo, S. Ferrero, and L. Scaltrito. Inkjet Printing and Low Power Laser Annealing of Silver Nanoparticle Traces for the Realization of Low Resistivity Lines for Flexible Electronics. *Microelectronic Engineering*, 88(8):2481–2483, 2011.
- [145] K. Yung, X. Gu, C. Lee, and H. Choy. Ink-Jet Printing and Camera Flash Sintering of Silver Tracks on Different Substrates. *Journal of Materials Processing Technology*, 210(15):2268–2272, 2010.
- [146] G. Cummins and M. P. Y. Desmulliez. Inkjet Printing of Conductive Materials: A Review. *Circuit World*, 38(4):193–213, 2012.
- [147] R. Abbel, P. Teunissen, E. Rubingh, T. V. Lammeren, R. Cauchois, M. Everaars, J. Valetton, S. V. D. Geijn, and P. Groen. Industrial-Scale Inkjet Printed Electronics Manufacturing - Production Up-Scaling From Concept Tools to a Roll-to-Roll Pilot Line. *Translational Materials Research*, 1: 015002, 2014.
- [148] I. Reinhold. Inkjet Printing of Functional Materials and Post-Processing. In S. Magdassi and A. Kamysny, editors, *Nanomaterials for 2D and 3D Printing*, pages 27–50. Wiley-VCH, Weinheim, 2017.
- [149] X. Fang, Y. Deng, and J. Li. Plasmon Resonance and Heat Generation in Nanostructures. *Mathematical Methods in the Applied Sciences*, 38:4663–4672, 2015.
- [150] K. I. Rybakov, V. E. Semenov, S. V. Egorov, A. G. Ereemeev, I. V. Plotnikov, and Y. V. Bykov. Microwave Heating of Conductive Powder Materials. *Journal of Applied Physics*, 99(2), 2006.
- [151] M. Figueroa, S. Schraer, K. Pourrezaei, and S. Tyagi. Surface Enhanced Raman Scattering and Microwave Absorption in Silver Nanoparticle Inks. In *Plasmonics in Biology and Medicine IX*, volume 8234, 2012.
- [152] I. Reinhold, M. Müller, M. Müller, W. Voit, and W. Zapka. Spectrally Enhanced Photonic Sintering. In *International Conference on Digital Printing Technologies and Digital Fabrication*, Quebec, CA, 2012.
- [153] D. Soltman, B. Smith, H. Kang, S. J. S. Morris, and V. Subramanian. Methodology for Inkjet Printing of Partially Wetting Films. *Langmuir*, 26(19):15686–15693, 2010.
- [154] H. Kang, D. Soltman, and V. Subramanian. Hydrostatic Optimization of Inkjet-Printed Films. *Langmuir*, 26(13):11568–11573, 2010.

- [155] R. D. Deegan, O. Bakajin, T. F. Dupont, G. Huber, S. R. Nagel, and T. A. Witten. Capillary Flow As the Cause of Ring Stains From Dried Liquid Drops. *Nature*, 389(6653):827–829, 1997.
- [156] E. L. Talbot, A. Berson, P. S. Brown, and C. D. Bain. Drying and Deposition of Picolitre Droplets of Colloidal Suspensions in Binary Solvent Mixtures. In *International Conference on Digital Printing Technologies and Digital Fabrication*, 2012.
- [157] J. Perelaer, P. J. Smith, C. E. Hendriks, A. M. J. van den Berg, and U. S. Schubert. The Preferential Deposition of Silica Micro-Particles at the Boundary of Inkjet Printed Droplets. *Soft Matter*, 4(5):1072, 2008.
- [158] T. Kajiya and W. Kobayashi. Controlling the Drying and Film Formation Processes of Polymer Solution Droplets With Addition of Small Amount of Surfactants. *The Journal of Physical Chemistry B*, 113:15460–15466, 2009.
- [159] R. Abbel, P. Teunissen, J. Michels, and W. A. Groen. Narrow Conductive Structures With High Aspect Ratios Through Single-Pass Inkjet Printing and Evaporation-Induced Dewetting. *Advanced Engineering Materials*, (5): 615–619, 2014.
- [160] A. V. Galakhov. Pore Coordination Number and Sintering. *Refractories and Industrial Ceramics*, 51(2):83–87, 2010.
- [161] K. A. Schroder. Mechanisms of Photonic CuringTM: Processing High Temperature Films on Low Temperature Substrates. In *Nanotech Conference Technical Proceedings*, pages 220–223, Boston, MA, 2011.
- [162] D. A. van den Ende, R. Hendriks, R. Cauchois, and W. A. Groen. Large Area Photonic Flash Soldering of Thin Chips on Flex Foils for Flexible Electronic Systems: In Situ Temperature Measurements and Thermal Modelling. *Electronic Materials Letters*, 10(6):1175–1183, 2014.
- [163] M. J. Guillot, K. A. Schroder, and S. C. McCool. Simulating the Thermal Reponse of Thin Films during Photonic Curing. In *IMECE12*, 2012.
- [164] J. Niittynen and M. Mantysalo. Characterization of Laser Sintering of Copper Nanoparticle Ink by FEM and Experimental Testing. *IEEE Transactions on Components, Packaging and Manufacturing Technology*, 4(12): 2018–2025, 2014.
- [165] A. O. Govorov and H. H. Richardson. Generating Heat With Metal Nanoparticles. *Nano Today*, 2(1):30–38, 2007.
- [166] K. L. Kelly, E. Coronado, L. L. Zhao, and G. C. Schatz. The Optical Properties of Metal Nanoparticles: The Influence of Size, Shape, and Dielectric Environment. *Journal of Physical Chemistry B*, 107(3):668–677, 2003.
- [167] P. Gokhale, D. Mitra, E. Sowade, K. Y. Mitra, H. L. Gomes, E. Ramon, A. Al-Hamry, O. Kanoun, and R. R. Baumann. Controlling the Crack Formation in Inkjet-Printed Silver Nanoparticle Thin-Films for High Resolution Patterning Using Intense Pulsed Light Treatment. *Nanotechnology*, 28(49):495301, 2017.
- [168] D. Weise, K. Y. Mitra, P. Ueberfuhr, and R. R. Baumann. Effect of the Light Spectrum of Various Substrates for Inkjet Printed Conductive Structures Sintered With Intense Pulsed Light. *AIP Conference Proceedings*, 1646:101–105, 2014.

- [169] A. Schuppert, M. Thielen, I. Reinhold, and W. Schmidt. Ink Jet Printing of Conductive Silver Tracks from Nanoparticle Inks on Mesoporous Substrates. In *International Conference on Digital Printing Technologies and Digital Fabrication*, 2011.
- [170] *Printed Electronics Substrate - Inkjet Receptive*. Novacentrix, May 2011. 2212.2.
- [171] R. Abbel, T. van Lammeren, R. Hendriks, J. Ploegmakers, E. J. Rubingh, E. R. Meinders, and W. A. Groen. Photonic Flash Sintering of Silver Nanoparticle Inks: A Fast and Convenient Method for the Preparation of Highly Conductive Structures on Foil. *MRS Communications*, 2(04):145–150, 2012.
- [172] Y. Khan, F. J. Pavinatto, M. C. Lin, A. Liao, S. L. Swisher, K. Mann, V. Subramanian, M. M. Maharbiz, and A. C. Arias. Inkjet-Printed Flexible Gold Electrode Arrays for Bioelectronic Interfaces. *Advanced Functional Materials*, 26(7), 2015.
- [173] V. Truskett and M. Watts. Trends in Imprint Lithography for Biological Applications. *Trends in biotechnology*, 24(7):312–7, 2006.
- [174] S. F. Wuister, J. H. Lammers, Y. W. Kruijt-Stegeman, L. V. D. Tempel, F. J. Dijkman, and L. Van Der Tempel. Squeeze Time Investigations for Step and Flash Imprint Lithography. *Microelectronic Engineering*, 86(4-6): 681–683, 2009.
- [175] N. Khusnatdinov, Z. Ye, K. Luo, T. Stachowiak, X. Lu, J. W. Irving, M. Shafran, W. Longsine, M. Traub, V. Truskett, B. Fletcher, W. Liu, F. Xu, D. LaBrake, and S. V. Sreenivasan. High-Throughput Jet and Flash Imprint Lithography for Advanced Semiconductor Memory. *Alternative Lithographic Technologies VI*, 9049:904910, 2014.
- [176] H. Bohlmann, B. Puerto, and P. Puerto. Modulare Rolle-zu-Rolle Produktionsplattform mit Integriertem Mikro-3D-Druck-System. *wt Werkstattstechnik*, 108:808–814, 2018.
- [177] C. Schmidleithner and D. Kalaskar. Stereolithography. In D. Cvetković, editor, *3D Printing*, pages 3–22. IntechOpen, 2018.
- [178] *Advanced DLP for Superior 3D Printing*. Envisiontec, March 2017. Technical Report.